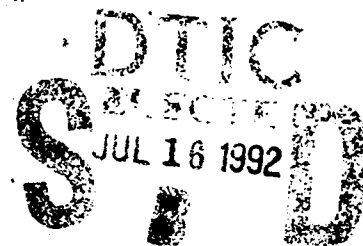


AD-A252 856



2

NAVAL POSTGRADUATE SCHOOL Monterey, California



THESIS

NONLINEAR DYNAMIC RESPONSE OF CYLINDRICAL
SHELLS SUBJECTED TO UNDERWATER SIDE-ON
EXPLOSIONS

by

Padraic K. Fox

MARCH 1992

Thesis Advisor:

Young W. Kwon

Approved for public release: Distribution is unlimited

92-18866



REPORT DOCUMENTATION PAGE				Form Approved OMB No 0704-0188	
1a REPORT SECURITY CLASSIFICATION Unclassified			1b RESTRICTIVE MARKINGS		
2a SECURITY CLASSIFICATION AUTHORITY		3 DISTRIBUTION/AVAILABILITY OF REPORT Approved for public release: Distribution is unlimited			
2b DECLASSIFICATION/DOWNGRADING SCHEDULE		4 PERFORMING ORGANIZATION REPORT NUMBER(S)			
4 PERFORMING ORGANIZATION REPORT NUMBER(S)		5 MONITORING ORGANIZATION REPORT NUMBER(S)			
6a NAME OF PERFORMING ORGANIZATION Naval Postgraduate School		6b OFFICE SYMBOL (If applicable) ME	7a NAME OF MONITORING ORGANIZATION Naval Postgraduate School		
6c ADDRESS (City, State, and ZIP Code) Monterey, CA 93943-5000			7b ADDRESS (City, State, and ZIP Code) Monterey, CA 93943-5000		
8a NAME OF FUNDING/SPONSORING ORGANIZATION		8b OFFICE SYMBOL (If applicable)	9 PROCUREMENT INSTRUMENT IDENTIFICATION NUMBER		
8c ADDRESS (City, State, and ZIP Code)			10 SOURCE OF FUNDING NUMBERS		
			PROGRAM ELEMENT NO	PROJECT NO	TASK NO
			WORK UNIT ACCESSION NO		
11 TITLE (Include Security Classification) NONLINEAR DYNAMIC RESPONSE OF CYLINDRICAL SHELLS SUBJECTED TO UNDERWATER SIDE-ON EXPLOSIONS (U)					
12 PERSONAL AUTHOR(S) PADRAIC K. FOX					
13a TYPE OF REPORT Master's Thesis		13b TIME COVERED FROM _____ TO _____	14 DATE OF REPORT (Year, Month, Day) MARCH 1992		15 PAGE COUNT 139
16 SUPPLEMENTARY NOTATION The views expressed are those of the author and do not reflect the official policy or position of the Department of Defense or the U. S. Government					
17 COSATI CODES			18 SUBJECT TERMS (Continue on reverse if necessary and identify by block number)		
FIELD	GROUP	SUB-GROUP			
			underwater shock		
19 ABSTRACT (Continue on reverse if necessary and identify by block number)					
<p>Two studies were performed to enhance the understanding of phenomena occurring in shell structures subjected to side-on underwater explosions. In the first, a numerical analysis was performed to investigate the non-linear response of cylindrical shells subjected to near-field side-on underwater explosions. In the second study, a numerical analysis of a cylindrical shell subjected to a far-field underwater explosion was compared with the results from an underwater explosion test. Sensitivity analyses were performed to determine the relative importance of various physical and numerical modelling factors.</p>					
20 DISTRIBUTION/AVAILABILITY OF ABSTRACT <input checked="" type="checkbox"/> UNCLASSIFIED/UNLIMITED <input type="checkbox"/> SAME AS RPT <input type="checkbox"/> DTIC USERS			21 ABSTRACT SECURITY CLASSIFICATION unclassified		
22a NAME OF RESPONSIBLE INDIVIDUAL Young W. Kwon		22b TELEPHONE (Include Area Code) (408) 646-3385		22c OFFICE SYMBOL ME/Kw	

Approved for public release: Distribution is unlimited

The Dynamic Response of Cylindrical Shells Subjected to Side-On
Underwater Explosions

by

Padraic K. Fox
Lieutenant Commander, United States Navy
B.S., United States Naval Academy, 1978

Submitted in partial fulfillment of the
requirements for the degrees of

MASTER OF SCIENCE
IN MECHANICAL ENGINEERING

and

MECHANICAL ENGINEER

from the

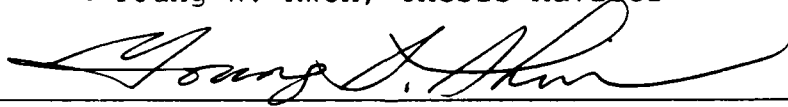
NAVAL POSTGRADUATE SCHOOL

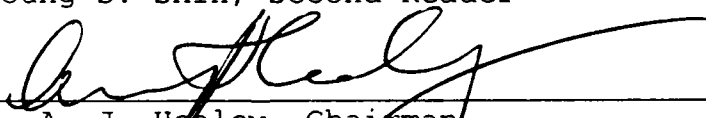
MARCH 1992

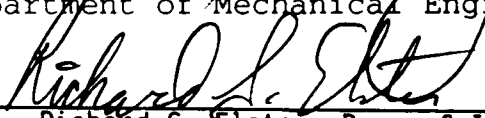
Author: _____

Approved by: _____


Young W. Kwon, Thesis Advisor


Young S. Shin, Second Reader


A. J. Healey, Chairman
Department of Mechanical Engineering


Richard S. Elster, Dean of Instruction

ABSTRACT

Two studies were performed to enhance the understanding of phenomena occurring in shell structures subjected to side-on underwater explosions. In the first, a numerical analysis was performed to investigate the non-linear response of cylindrical shells subjected to near-field side-on underwater explosions. In the second study, a numerical analysis of a cylindrical shell subjected to a far-field underwater explosion was compared with the results from an underwater explosion test. Sensitivity analyses were performed to determine the relative importance of various physical and numerical modelling factors.

DTIC QUALITY INSPECTED 2

Accession For	
NTIS GRA&I	<input checked="" type="checkbox"/>
DTIC TAB	<input type="checkbox"/>
Unannounced	<input type="checkbox"/>
Justification	
By _____	
Distribution/	
Availability Codes	
Dist	Avail and/or Special
A-1	

TABLE OF CONTENTS

I.	INTRODUCTION	1
II.	NUMERICAL COMPUTER CODE	7
A.	GENERAL DESCRIPTION OF THE METHOD	7
B.	VEC/DYNA3D FINITE ELEMENT METHOD CODE	8
C.	USA BOUNDARY ELEMENT METHOD CODE	11
D.	USA/DYNA3D CODE VERIFICATION	16
	1. DETAILED DESCRIPTION OF THE SPHERICAL MODEL	16
	2. DETAILED DESCRIPTION OF THE INFINITE CYLINDER MODEL	18
III.	NEAR FIELD SIDE-ON UNDERWATER EXPLOSION ANALYSIS	32
A.	GENERAL DESCRIPTION AND OBJECTIVES	32
B.	DESCRIPTION OF MODEL USED FOR THE STUDY	33
	1. CYLINDER MODEL	34
	2. EXPLOSIVE CHARGE	35
	3. SURROUNDING WATER	36
C.	RESULTS OF THE NEAR FIELD STUDY	39
	1. FREE FIELD TRANSMISSION AND SHELL WATER INTERACTION	39
	2. SHELL RESPONSE	45
	a. UNSTIFFENED MODEL	45
	b. STIFFENED MODEL	57
IV.	FAR FIELD SIDE-ON EXPLOSION ANALYSIS	59
A.	GENERAL DESCRIPTION AND OBJECTIVES	59
B.	DESCRIPTION OF MODELS USED FOR THE FAR FIELD STUDY AND EXPERIMENTAL METHOD	60
	1. PHYSICAL MODEL	60
	2. UNDERWATER EXPLOSION TEST	61
	3. NUMERICAL MODEL	65
C.	FAR FIELD STUDY RESULTS	76
	1. EXPERIMENTAL TO NUMERICAL COMPARISON	76
	2. SENSITIVITY ANALYSES	85
	a. END EFFECT SENSITIVITY ANALYSIS	85
	b. SHELL FORMULATION, QUADRATURE RULE AND INTEGRATION TIME INCREMENT SENSITIVITY ANALYSES	91
	c. ROTATION SENSITIVITY ANALYSIS	102
	3. PHYSICAL FINDINGS	110
	a. RESPONSE MODES	110
	b. ROTATIONAL EFFECTS	115

1. NUMERICAL MODELLING	118
2. PHYSICAL ASPECTS	119
a. NEAR FIELD PHYSICAL RESULTS	119
b. FAR FIELD PHYSICAL RESULTS	119
B. RECOMMENDATIONS.	120
1. TOPICS FOR ADDITIONAL STUDY.	120
a. WELDING FABRICATION EFFECTS.	120
b. EIGHT NODE BRICK SHELL SENSITIVITY ANALYSES.	120
c. FAILURE CRITERIA.	121
d. NEAR FIELD EXPERIMENTATION	121
2. RECOMMENDATIONS TO IMPROVE TEST CONTROL. . .	121
LIST OF REFERENCES	123
INITIAL DISTRIBUTION LIST	125

LIST OF FIGURES

Figure II.1.	Elastic sphere verification model.	16
Figure II.2.	Elastic sphere verification model geometry.	17
Figure II.3.	Spherical model verification results.	19
Figure II.4.	Infinite cylinder verification model.	20
Figure II.5.	Infinite cylinder verification geometry.	21
Figure II.6.	Near element oscillation reduction for infinite cylinder verification model.	23
Figure II.7.	Remote element oscillation reduction for infinite cylinder verification model.	24
Figure II.8.	Infinite cylinder results with $\eta = 0.00$	26
Figure II.9.	Infinite cylinder results with $\eta = 0.25$	27
Figure II.10.	Infinite cylinder results with $\eta = 0.50$	28
Figure II.11.	Infinite cylinder results with $\eta = 0.75$	30
Figure II.12.	Infinite cylinder results with $\eta = 1.00$	31
Figure III.1.	Quarter symmetry model for near field side-on attack analysis.	33
Figure III.2.	Shell quarter symmetry discretization for near field side-on attack analysis.	34
Figure III.3.	Explosive charge quarter symmetry discretization for near field analysis.	37
Figure III.4.	Location of specified elements for near field analysis.	39
Figure III.5.	Pressure-time history for specified water elements for near field analysis.	40
Figure III.6.	Pressure fringe plot as the pressure wave strikes the nearest shell surface.	43
Figure III.7.	Pressure fringe plot as cavitation occurs in water near the shell surface.	43
Figure III.8.	Propagation of Von Mises stress at 90 microseconds (30 microseconds after pressure wave impact).	46

Figure III.9.	Mushroom shaped propagation of Von Mises stress at 150 microseconds.	46
Figure III.10.	Nearest element stress history for near field analysis.	50
Figure III.11.	Nearest element effective plastic strain time history for near field analysis.	50
Figure III.12.	Mid element Von Mises stress time history for near field analysis.	52
Figure III.13.	Mid element effective plastic strain time history for near field analysis.	52
Figure III.14.	Remote element Von Mises stress time history plot for near field analysis.	54
Figure III.15.	Remote element effective plastic strain time history plot for near field analysis.	54
Figure III.16.	Stress intensification in remote element during near field attack.	55
Figure III.17.	Final deformed condition of cylinder for near field attack.	56
Figure III.18.	Stiffener failure by tripping in near field attack stiffened model.	58
Figure IV.1.	Undex test profile.	63
Figure IV.2.	Undex test general arrangement.	64
Figure IV.3.	Undex test instrumentation diagram	66
Figure IV.4.	Low density, full model	67
Figure IV.5.	Refined mesh model.	68
Figure IV.6.	Effective plastic strain pattern on cylinder side nearest the explosive charge.	69
Figure IV.7.	Effective plastic strain pattern on cylinder side most remote from the charge.	69
Figure IV.8.	Mesh sensitivity comparison for surface of shell located nearest the explosive charge (location B1).	71
Figure IV.9.	Mesh sensitivity comparison for position with largest plastic strain (locations A1 and C1).	72

Figure IV.10.	Mesh sensitivity comparison for point on cylinder most circumerentially remote from the charge (location B3).	73
Figure IV.11.	Undex pressure profile.	75
Figure IV.12.	Experimental/numerical comparison for position A1 axial strain.	79
Figure IV.13.	Experimental/numerical comparison for position A2 hoop strain.	80
Figure IV.14.	Experimental/numerical comparison for position A2 axial strain.	80
Figure IV.15.	Experimental/numerical comparison for position B1 hoop strain.	81
Figure IV.16.	Experimental/numerical comparison for position B1 axial strain.	81
Figure IV.17.	Experimental/numerical comparison for position B2 hoop strain	82
Figure IV.18.	Experimental/numerical comparison for position B2 axial strain	82
Figure IV.19.	Experimental/numerical comparison for position B3 hoop strain	83
Figure IV.20.	Experimental/numerical comparison for position B3 axial strain	83
Figure IV.21.	Experimental/numerical comparison for position C1 axial strain	84
Figure IV.22.	Experimental/numerical comparison for position C2 hoop strain	84
Figure IV.23.	End effect sensitivity results (A1 axial)	88
Figure IV.24.	End effect sensitivity results. (A2 Hoop)	88
Figure IV.25.	End effect sensitivity results. (A2 Axial)	89
Figure IV.26.	End effect sensitivity results. (C1 Axial)	89
Figure IV.27.	End effect sensitivity results. (C2 Hoop)	90
Figure IV.28.	Shell formulation sensitivity results. (A1 Axial)	94

Figure IV.29.	Shell formulation sensitivity results. (A2 Hoop)	94
Figure IV.30.	Shell formulation sensitivity results. (A2 Axial)	95
Figure IV.31.	Shell formulation sensitivity results. (B1 Hoop)	95
Figure IV.32.	Shell formulation sensitivity results. (B1 Axial)	96
Figure IV.33.	Shell formulation sensitivity results. (B2 Hoop)	96
Figure IV.34.	Shell formulation sensitivity results. (B2 Axial)	97
Figure IV.35.	Shell formulation sensitivity results. (B3 Hoop)	97
Figure IV.36.	Shell formulation sensitivity results. (B3 Axial)	98
Figure IV.37.	Shell formulation sensitivity results. (C1 Axial)	98
Figure IV.38.	Shell formulation sensitivity results. (C2 Hoop)	99
Figure IV.39.	Effect of changing quadrature rule and time integration increment at location of highest strain (A1 and C1 hoop).	100
Figure IV.40.	Rotation sensitivity results. (A1 Hoop)	103
Figure IV.41.	Rotation sensitivity results. (A1 Axial)	103
Figure IV.42.	Rotation sensitivity results. (A2 Hoop)	104
Figure IV.43.	Rotation sensitivity results. (A2 Axial)	104
Figure IV.44.	Rotation sensitivity results. (B1 Hoop)	105
Figure IV.45.	Rotation sensitivity results. (B1 Axial)	105
Figure IV.46.	Rotation sensitivity results. (B2 Hoop)	106
Figure IV.47.	Rotation sensitivity results. (B2 Axial)	106
Figure IV.48.	Rotation sensitivity results. (B3 Hoop)	107
Figure IV.49.	Rotation sensitivity results. (B3 Axial)	107
Figure IV.50.	Rotation sensitivity results. (C1 Hoop)	108
Figure IV.51.	Rotation sensitivity results. (C1 Axial)	108
Figure IV.52.	Rotation sensitivity results. (C2 Hoop)	109

Figure IV.53.	Rotation sensitivity results. (C2 Axial)	109
Figure IV.54.	Cylinder accordion motion.	111
Figure IV.55.	Cylinder whipping motion in plane parallel to shock wave direction.	112
Figure IV.56.	Cylinder curvature as a result of whipping motion (scale factor 20).	113
Figure IV.57.	Cylinder breathing motion perpendicular to the shock wave direction of travel.	114
Figure IV.58.	Illustration of cylinder breathing mode at two different times (scale factor 40).	115
Figure IV.59.	Effective plastic strain distribution for near and remote side of cylinder with 7.5 degrees of rotation.	117

ACKNOWLEDGEMENTS

I would like to express my gratitude to Professors Young W. Kwon and Young S. Shin for their guidance, encouragement and support in carrying out this research. In addition, I would like to thank Dr. Thomas T. Tsai and Dr. Kent Goering, of the Defense Nuclear Agency, for supporting this research. Finally, I would like to thank the other members of the Naval Postgraduate School shock group, and in particular, Lieutenant William Miller and Lieutenant James Chisum for their assistance in performing this research.

I. INTRODUCTION

Surface ship and submarine survivability and cost have become the U. S. Navy's primary ship design concerns over the last several years. Unfortunately, these two criteria are often incompatible. In general, improved survivability leads to higher overall design and manufacturing costs for ships and submarines. In addition, congressionally mandated survivability testing has added substantial costs to the design and acceptance process for ships and submarines and their associated equipment.

A key survivability issue is a vessels ability to withstand the shock and blast effects of an underwater explosion. This issue has been emphasized for both the surface and submarine communities by recent events. Operations in the Persian Gulf both during the Iran/Iraq war and during operations Desert Shield and Desert Storm required movement of ships in shallow, mine infested waters. There is little reason to believe that future conflicts will be any different.

Currently recommended survivability goals state that it is desirable that ships should be able to stay afloat and continue to fight after a hit by enemy ordinance similar to the mines encountered by the USS Roberts, USS Tripoly and USS

Princeton. The near loss of the USS Roberts emphasized a need to improve the structural strength of warships. While the Princeton incident clearly demonstrates the positive impact of the Navy shock hardening program, it also shows that the Navy has not yet completely achieved the stated survivability goal.

Similarly, especially with a reduced deep water threat resulting from the dissolution of the Soviet Union and the expected division of the Soviet Navy, U. S. Navy submarines deployed in future conflicts are more likely to be required to operate against small conventionally powered submarines in shallow coastal waters with the same mine threat already encountered by surface units.

Therefore significant interest continues in determining methods that can reduce costs in both the design and manufacturing phases of ship procurement while still improving the shock and structural hardness of both surface vessels and submarines. One primary means of achieving cost savings without loss of desired attributes is the process of optimization of ship designs. This process reduces cost by removing unneeded redundancy. However, to perform an optimization, a designer must have a clear understanding of the modes of failure and their causes. Unfortunately, the interaction between an underwater shock wave and a ship hull as well as the effect on equipment is a highly complex event and remains poorly understood. In the past, data for studying failure modes and the underlying physics of the events leading

to failure has been obtained through costly and time consuming process of underwater explosion testing. This process, although useful, is extremely limited. Models tested to failure can only be used once and each model can only contain a limited number of data collection instruments. In addition, environmental safety concerns are increasing costs and imposing limitations on the Navy's ability to carry out required testing.

The rapid improvement of digital computing technology over the last decade is a possible solution to the problem. While computer technology cannot completely replace live testing, properly constructed computer models provide an opportunity to obtain an unlimited amount of data without the limitations associated with live testing. In addition, if computer model predictions can be shown to be reliable, some cost reduction may be possible through the reduction of live testing required to meet congressionally mandated survivability testing. However, currently existing computer codes used to construct and process computer models in this field, although promising are not yet proven.

A research program is underway at the Naval Postgraduate School to study numerical modeling of ship structures subjected to both near and far field underwater explosions. This program is expected to improve the understanding of factors affecting the reliability of numerical models and provide insight into the dynamic response of surface ship and

submarine hulls and the physics that lead to failure when a hull is subjected to an underwater shock wave. The current study centers around simple cylinders constructed of a homogenous material. Previous work in the program is documented in reference 1. Future studies will include more complex materials and structures as experience increases and the reliability of the numerical models is proven.

This thesis deals specifically with the non-linear response of a cylindrical shell subjected to both near field and far field side-on attacks. The first object of the research was to prove that the numerical computer code developed for the research provided correct results. The verification included comparison of numerical results to analytical solutions for two simple models. The results show that the numerical solution closely matched the analytic solution in both cases.

The near field study compares numerical predictions with expected physical results in the shell and the surrounding water. It also discusses physical findings related to the near field attack. Specifically, the most significant damage was found to be local in nature. Damage included severe local buckling of the shell at the point nearest the charge. Further, stiffeners in stiffened models failed by local tripping.

The far field study compares numerical predictions with experimental results obtained from an underwater explosion test

of an aluminum cylinder subjected to a far field side on attack. In addition, analyses were performed to determine the sensitivity of the results to:

- mesh refinement
- boundary effects
- rotation from expected configuration
- number of quadrature points used for integration
- time integration increment
- type of shell element formulation

used for the analysis. Results show that numerical computer codes can generally match experimental results if end effects and rotation are correctly modelled. Inconsistencies between experimental and numerical results is most likely caused by uncontrolled factors associated with the underwater explosion test and overall element averaging rather than a failure of the numerical method to provide correct results.

Physical results included observation of the primary response and damage modes. Primary response modes included accordion motion, whipping motion and breathing motion in the direction perpendicular to the charge. Damage was found to be more global in nature than that found for the near field case. Primary damage areas were located near the end plates on the side of the cylinder nearest the charge and at the center of the cylinder on the side most remote from the charge.

Recommendations will be provided to improve control of future tests to improve final results. Finally, preparations

for future testing will be described and recommendations for additional study are provided.

II. NUMERICAL COMPUTER CODE

A. GENERAL DESCRIPTION OF THE METHOD

The near field portion of this study was performed using the finite element method. The finite element method uses a discretized representation of the cylindrical model and the surrounding water along with appropriate material models and equations of state to obtain a solution for the response of the shell to a near field explosion.

The far field study was performed using the finite element method to obtain the response of the shell. However, the surrounding water was modelled using the boundary element method. The boundary element method uses fundamental physical principles to reduce the surrounding media and the associated forces to discrete forces and masses which are applied to the nodes of a two dimensional mesh. The two dimensional mesh, in turn is superimposed over the surface of the shell. Use of the boundary element method significantly reduces the number of elements required for the numerical model, and subsequently reduces the computational effort required to solve the problem. For example, models used for the near field problem consisted of more than 13000 three dimensional elements. In contrast, the most refined model used for the far field problem consisted of only 984 elements, or approximately 7.5%

of the total required for the near field problem. In addition to the reduced computational effort, the reduced number of elements allowed the storage of significantly more data per element, providing additional flexibility and improvement in the study. The finite element method (FEM) computer code used for the analysis was VEC/DYNA3D and the boundary element method (BEM) computer code was USA (Underwater Shock Analyzer) code.

To solve the far field problem, a link was developed to allow the boundary element computer code and the finite element computer code to operate interactively. This linkage was developed in 1991 at the request of the Naval Postgraduate School under funding provided by the Defense Nuclear Agency (DNA). A more detailed description of the two computer codes is provided in the following sections.

B. VEC/DYNA3D FINITE ELEMENT METHOD CODE

VEC/DYNA3D [Ref. 2] is an explicit finite element code. It has been used successfully for various types of dynamic nonlinear engineering problems since its conception in 1976. VEC/DYNA3D was selected for this study for several reasons. First, as stated above, VEC/DYNA3D is an explicit code. This attribute has two distinct advantages and two disadvantages. The advantages are its relatively high speed and its ability to be implemented on a relatively small stand alone engineering workstation. Initial work for this study is being

performed on IBM RISC 6000 workstations. Once the USA/DYNA3D interface is proven to be reliable and accurate and experience has been gained in the use of the software, work will begin on more complex models using main frame type computers. Therefore it was important to obtain a code that was able to work significant problems on a small workstation and yet be compatible with the main frames expected to be used in the future. VEC/DYNA3D is compatible with a full range of engineering workstations and has been implemented on the Los Alamos CRAY computer. Problems including up to 20000 solid elements have been run on Naval Postgraduate School workstations with 16 megabytes of random access memory.

The first disadvantage associated with the explicit numerical code is that the code is not inherently stable. This means that any problems dealing with time integration, including the underwater shock problems included in this study must be treated with care. Integration time steps must be matched closely with the size of the elements in the problem. This is performed automatically by VEC/DYNA3D in the stand alone mode. However, when coupled with the USA code, this automation is no longer functional. Incorrect selection of integration time steps can lead to significant oscillations and/or inaccuracies in the final solution.

The second problem associated with the explicit codes is the mesh reflection effect. In explicit codes, non-uniform meshes result in inaccurate solutions due to mesh reflection.

Two factors appear to be important in ensuring that correct solution was obtained. The first is mesh size and the second is total mass of neighboring elements. Sensitivity analyses indicate that error in the final solution is relatively small if neighboring elements are kept within ten percent of each other in size. This rule of thumb was used whenever possible in the performance of this study. However, this factor leads to some inefficiency in obtaining solutions since refinement must be performed over a larger area of the mesh to obtain a mesh independent solution than might normally be required in an implicit code. The additional area means more total elements and a subsequent increase in computation time to obtain the problem solution. Careful selection of the time integration increment can minimize this problem and allows use of larger variations at the expense of longer problem run times. These disadvantages can be overcome through careful planning. In general, they did not significantly overshadow the benefits associated with using an explicit code.

The second reason for selecting VEC/DYNA3D was its high degree of flexibility. It has a wide range of available material models and equations of state including the ability to model strain rate sensitivity, explosive materials and acoustic media. This flexibility is enhanced by the large degree of interactivity available with VEC/DYNA3D when used with the INGRID pre-processor [Ref. 3] and TAURUS post-processor [Ref. 4]. Changes can be entered with relative ease

using the pre-processor and almost any desired quantity can be obtained through knowledgeable use of the post-processor once the calculations are complete.

The final reason for selecting VEC/DYNA3D is that it is available in the public domain. Therefore the only cost associated with its use in this project was the cost associated with developing the link between VEC/DYNA3D and USA.

C. USA BOUNDARY ELEMENT METHOD CODE

The Underwater Shock Analyzer (USA) code [Ref. 5] is a boundary element code based on the Doubly Asymptotic Approximation (DAA) theory developed by T. L. Geers in 1971 [Ref. 6]. Through the use of the DAA theory and the boundary element formulation, USA computes the acoustic pressure loading and added mass matrices which represent the fluid surrounding the submerged shell. The acoustic pressure loading and added mass are applied at selected wetted nodes. This formulation has the benefit of significantly decreasing the number of elements required to model the submerged system since external water elements need not be included in the calculations. As stated previously, the reduced number of elements requires substantially less time and storage space to obtain a solution.

A detailed description of the DAA theory used in the USA code is provided by reference 7. In general, the governing

differential equation for the structure and the acoustic wave equation along with geometric compatibility between the fluid and the structure and appropriate initial conditions and boundary conditions are used to solve for the general structural response.

The governing differential equation for the structure is given below.

$$[M_s] \{\ddot{x}\} + [C_s] \{\dot{x}\} + [K_s] \{x\} = \{f\} \quad (1)$$

where $[M_s]$, $[C_s]$ and $[K_s]$ are the structural mass, structural damping and structural stiffness matrices. Further,

$\{\ddot{x}\}$, $\{\dot{x}\}$ and $\{x\}$ are the vectors of nodal acceleration, velocity and displacement for the structure.

The $\{f\}$ vector is the vector of nodal excitation forces generated by the acoustic wave. The nodal excitation force is a function of the incident and scattered pressures of the impinging acoustic wave and any concentrated loads applied to the structure. The equation specifying this relationship is shown below.

$$\{f\} = -[G] [A_f] \{P_i + P_s\} + \{f_d\} \quad (2)$$

where $[G]$ is the fluid/structure transformation matrix, $[A_f]$ is the diagonal area matrix associated with the fluid mesh,

$\{f_d\}$ is the vector of concentrated forces and $\{P_i + P_s\}$ is the vector of incident and scatter pressures.

In the above equation, all quantities are known with the exception of $\{P_s\}$. The scattered pressure can be represented in the form of a first order ordinary differential equation in terms of the fluid mass, element areas, density of the water, speed of sound in water and the vector velocity of the scattered acoustic wave.

$$[M_f] \{\dot{P}_s\} + \rho c [A_f] \{P_s\} = \rho c [M_f] \{\dot{u}_s\} \quad (3)$$

In the above equation ρ , c , $[M_f]$ and $\{\dot{u}_s\}$ are the water density, speed of sound in water, the fluid mass matrix and the vector of acoustic velocities respectively. The remaining quantities were previously defined. The fluid mass matrix is a diagonal matrix of virtual masses calculated by the boundary element method. This virtual mass is added to the structural mass and becomes important at low structural frequencies where the inertia of the water surrounding the structure can significantly affect the response of the structure.

At this point, the doubly asymptotic approximation is applied. The first asymptotic approximation, or high frequency approximation applies at early times very near the surface of the structure. It assumes that $|\dot{P}_s| \gg |P_s|$. This is a logical assumption and can be easily visualized in the one

dimensional case since the scatter wave of a one dimensional wave will completely reverse its direction according to Snell's law when it strikes a nearly rigid structure. As the change in direction is virtually instantaneous, the time derivative of $\{P_s\}$, or in other words $\{\dot{P}_s\}$, will be nearly infinite. Therefore, after integration, the differential equation which describes the scattered wave pressure is reduced to:

$$\{P_s\} = \rho c \{u_s\} \quad (4)$$

allowing the direct solution of the scattered wave pressure.

The late time asymptotic approximation, or low frequency approximation assumes that $|\dot{P}_s| \ll |P_s|$. Again, this is a logical assumption since the velocity of the scattered wave becomes constant at the speed of sound in water as the scattered wave travels a significant distance from the structure surface. As a result, the differential equation describing $\{P_s\}$ can be modified as shown below.

$$[A_f] \{P_s\} = [M_f] \{\dot{u}_s\} \quad (5)$$

The above solution is known as the first order Doubly Asymptotic Approximation (DAA1) and is exact at early and late

times for a planar surface. However, it does not take into account the effects of curvature.

Since most surfaces have some curvature, a second DAA theory was developed called DAA2 or the second order Doubly Asymptotic Approximation. The DAA2 theory is described in reference 8.

It must be noted that this code has limitations which result directly from the fundamental assumptions associated with the DAA theory [Ref. 5]. First, DAA is not theoretically appropriate for concave or multiple structures or near surface problems involving convex bodies. However, studies show that only results in highly shadowed, closely spaced areas or regions of strong concavity are affected. Secondly, DAA requires that the source of the incident wave be sufficiently removed from the structure since it can only account for acoustic waves and not hydrodynamic flow. Finally, the DAA theory is based on an early time (high frequency) approximation coupled with a late time (low frequency) approximation. Therefore, although the DAA solution will be very good at early times when the high frequency approximation is dominant and at late times when the low frequency approximation is dominant, it can vary significantly from the analytic or exact solution during intermediate times when neither the high or low frequency solution is dominant.

D. USA/DYNA3D CODE VERIFICATION

Since the USA/DYNA3D interface was new and had not been tested, some effort was expended on performing a verification of the performance of the combined computer code. To perform the verification, two cases with known analytic results were modelled using the USA/DYNA3D code. The first case was a quarter sphere and the second was an infinite cylinder. Results were satisfactory for both cases and the code interface is believed to be performing correctly.

1. DETAILED DESCRIPTION OF THE SPHERICAL MODEL

Figure II.1 shows the quarter symmetry model used for comparison to analytical results. The model contains 150

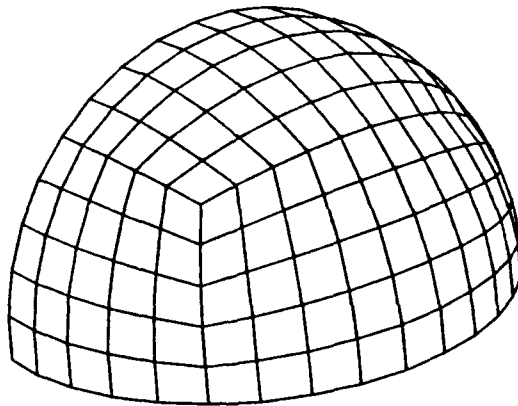


Figure II.1. Elastic sphere verification model.

elements. Figure II.2 shows the verification model test geometry. The thickness to diameter ratio of the shell is 1 to 50 and the shell is constructed of steel. The excitation is provided by a very small step pressure wave. As a result,

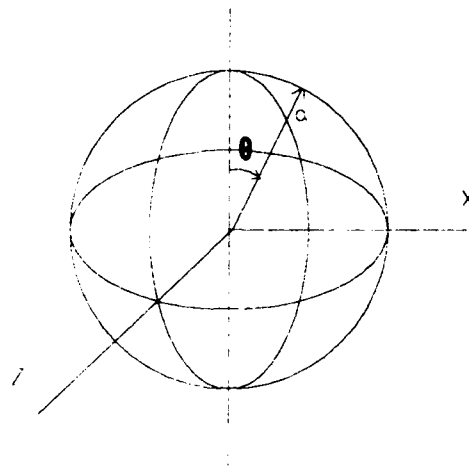


Figure II.2. Elastic sphere verification model geometry.

the shell response is considered to be completely elastic. The case was run using the elastic material model of DYNA3D and, since results are being compared to the analytic results found in reference 7, the same material and water properties as those found in reference 7 were used. As stated in reference 7, the exact solution is obtained from separation of variables as shown in reference 10. The material and water

properties used are listed below:

Steel Properties

Young's Modulus	E=206.84 GPa
Poisson's ratio	$\nu = 0.33$
Mass density	$\rho = 7784.5 \text{ kg/m}^3$

Water Properties

Sound speed	c=1461.2 m/s
Density	$\rho=999.6 \text{ kg/m}^3$

The numerical results using the USA/DYNA3D combination for the above test case compare favorably with the exact results. The normalized results are shown in Figure II.3. It can be seen that the numerical results lag the exact results, but the difference is negligible.

2. DETAILED DESCRIPTION OF THE INFINITE CYLINDER MODEL

The infinite cylinder model was run using the same material and water properties shown above. Figure II.4 shows the geometry used for the analyses and, as shown in Figure II.5, a single ring of elements was used to model the infinite cylinder by enforcing symmetry boundary conditions on each end of the model. In addition, since this is a two dimensional problem, the TWODIM option in USA was used to generate the

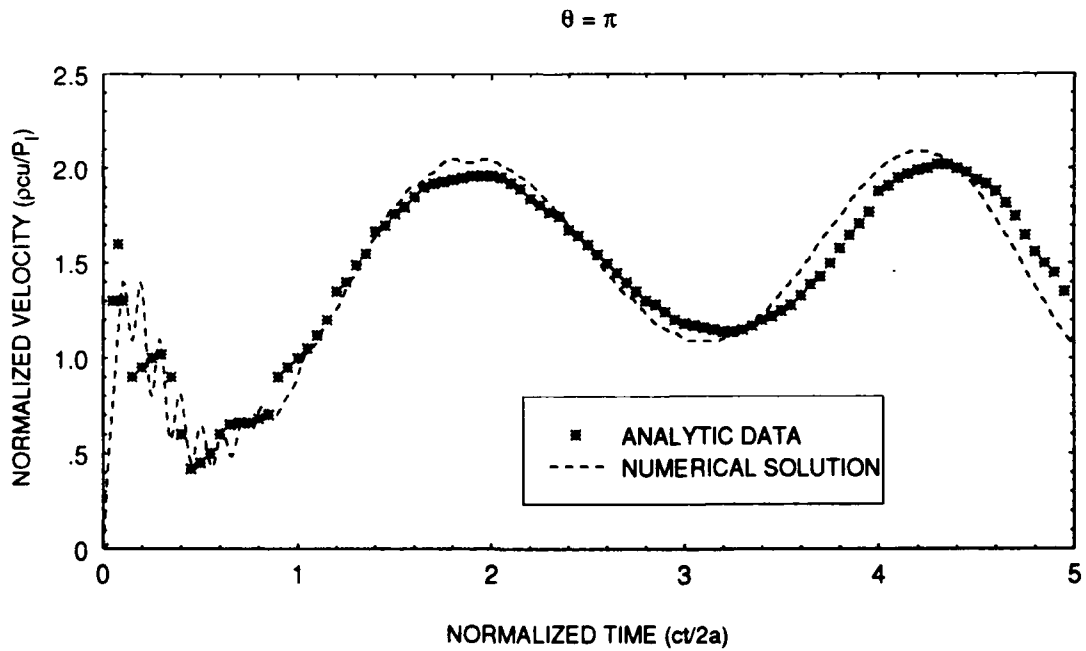
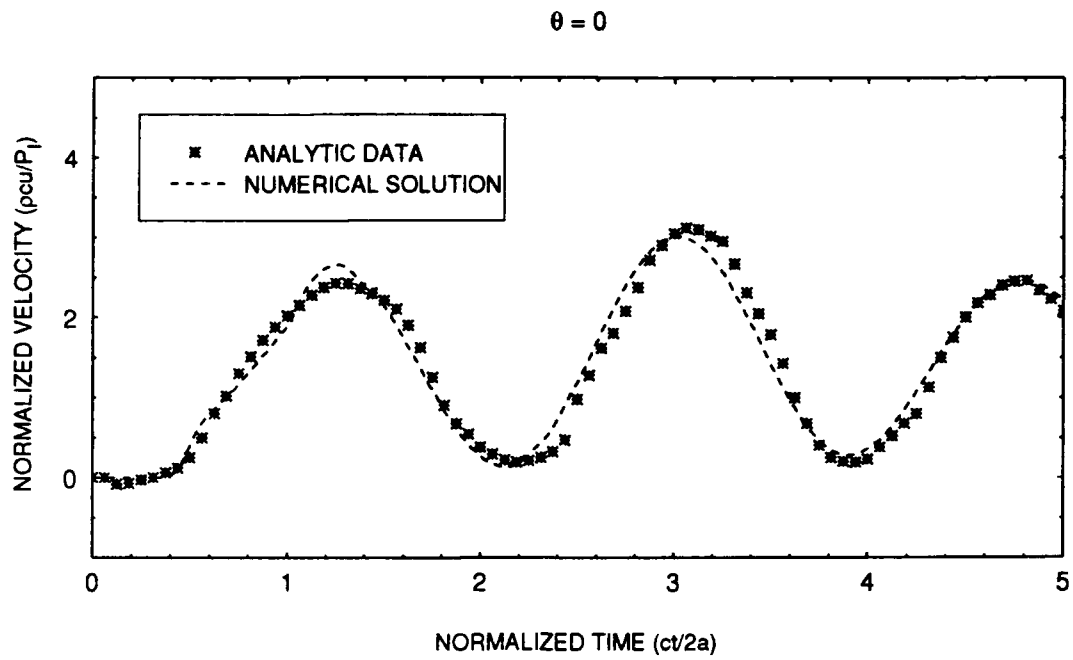


Figure II.3. Spherical model verification results.

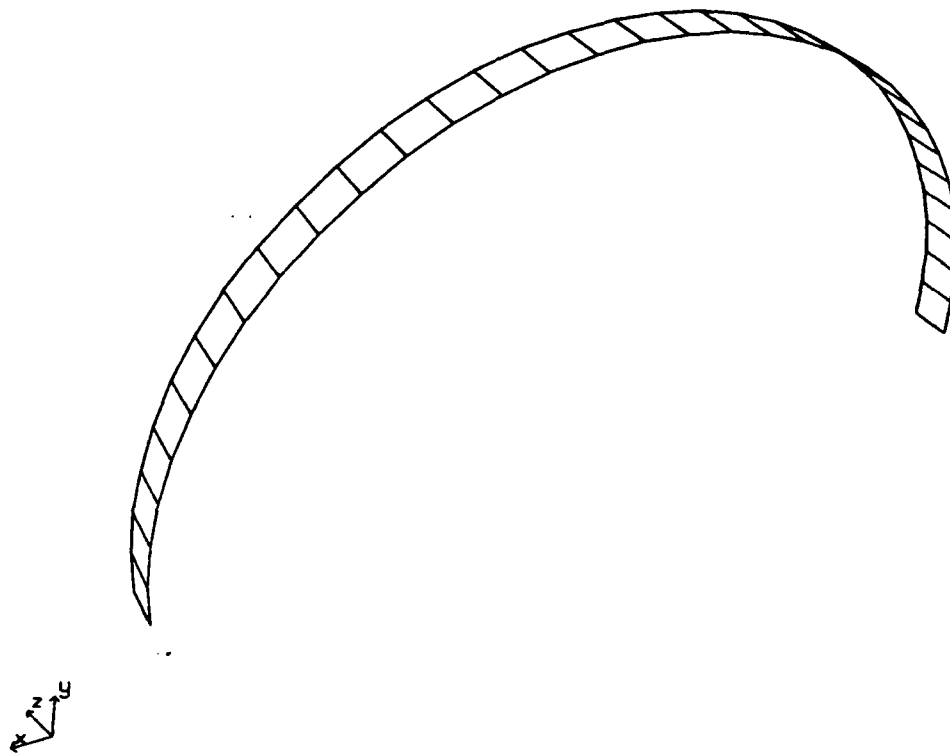
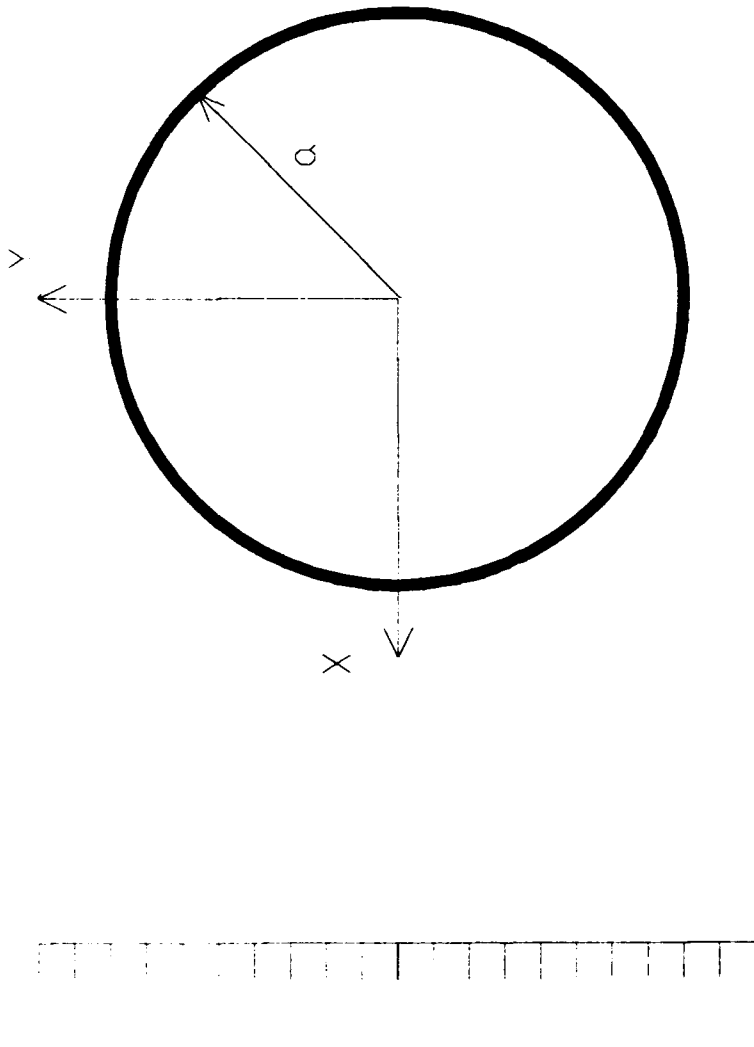


Figure II.4. Infinite cylinder verification model.



INCIDENT PLANE
WAVE

Figure II.5. Infinite cylinder verification geometry.

added mass and DAA matrices. Further, the value of the η variable was set to 0.0. η is a factor that accounts for curvature in the structure. If $\eta = 0.0$, there is no correction and the DAA solution provided is equivalent to the DAA1 solution which is exact for a planar surface. $\eta = 1.0$ is suitable for a spherical surface. Structures that are neither planar or spherical require a value between 0.0 and 1.0. In this case, the use of $\eta = 0.0$ allowed computation of a DAA1 solution for comparison to a known analytic DAA1 solution for a cylinder. The first model attempted had a longitudinal length of 0.1 inches. However, it was discovered that this resulted in a oscillatory solution as shown in the first graph in Figure II.6. A similar oscillation occurred on the reverse side of the cylinder as shown in the first graph of Figure II.7. After a check of the input data to ensure that the problem was not caused by numerical instability, it was hypothesized that the oscillation was caused by residual three dimensional effects caused by the finite width of the model. As a test of this hypothesis, two additional models were run with widths of 0.01 and 0.001 inches. As shown in Figure II.6 and II.7, reduction in width progressively reduced the oscillations on both the front and back of the cylinder. At 0.001 inches, oscillations are absent.

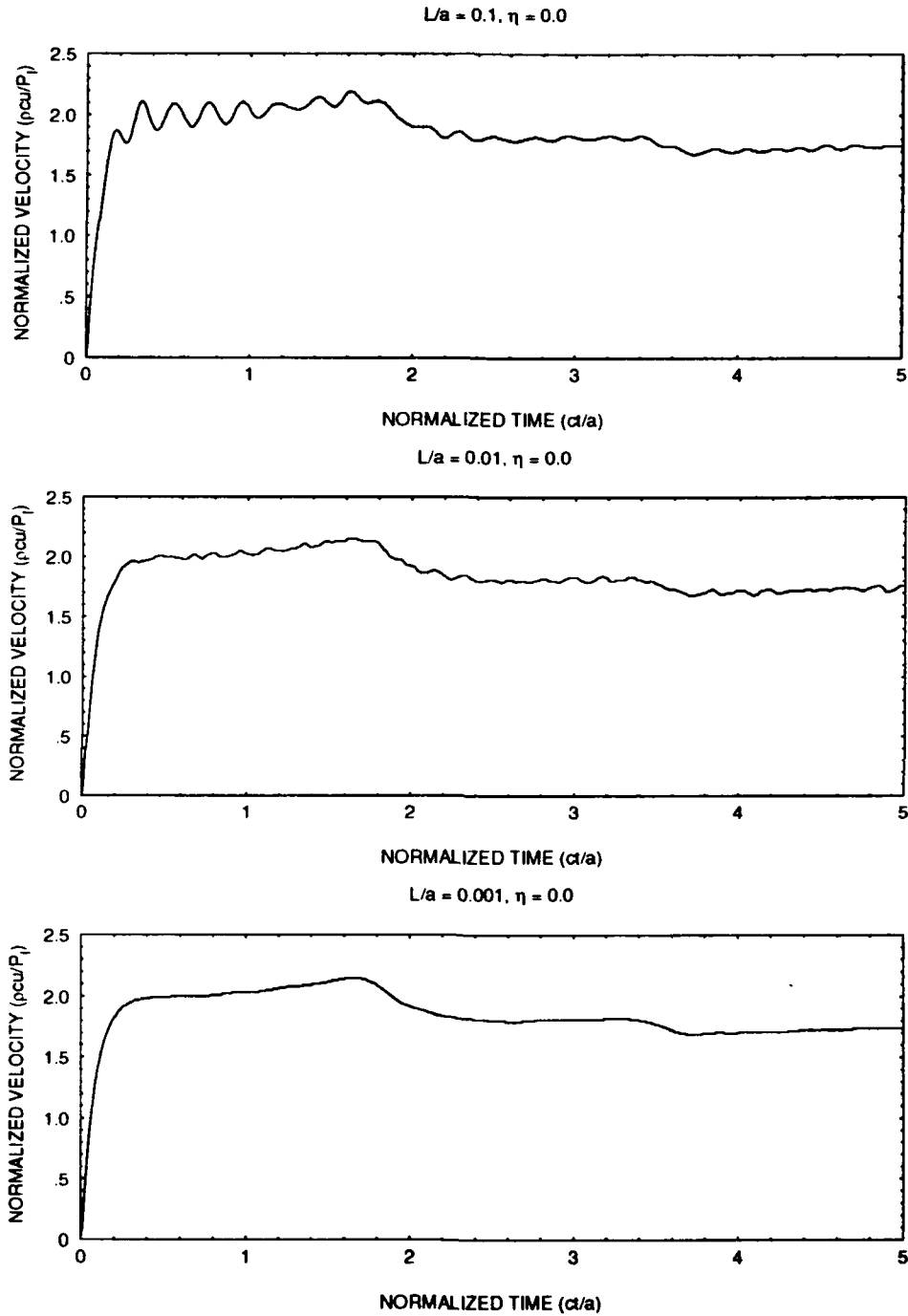


Figure II.6. Near element oscillation reduction for infinite cylinder verification model.

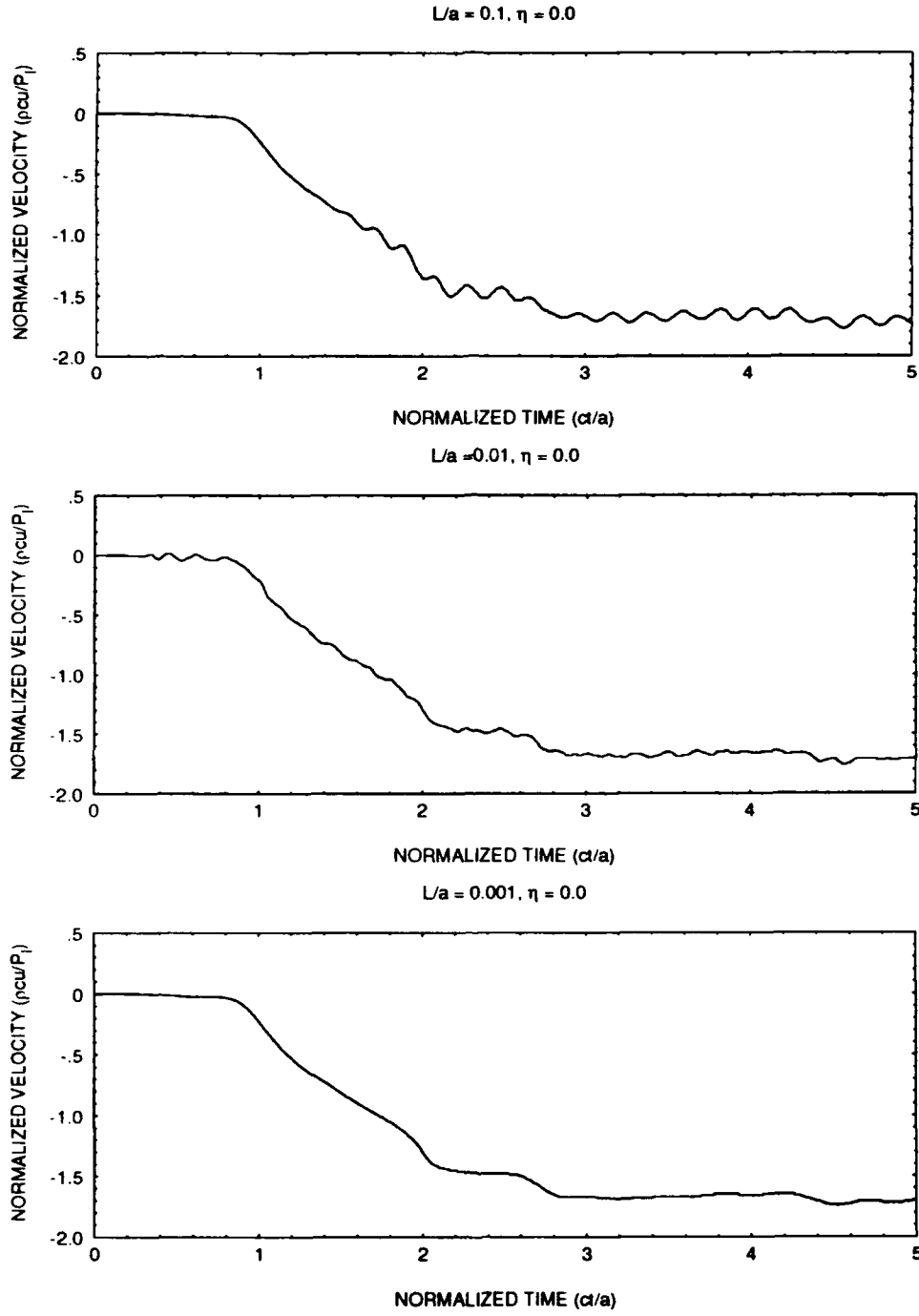


Figure II.7. Remote element oscillation reduction for infinite cylinder verification model.

The final results from the 0.001 inch model with an η variable value of 0.0 were compared to the analytical exact and analytical DAA1 solutions with favorable results as shown in Figure II.8. It can be seen that the results on both the front and back sides of the cylinder lie very close to the analytic DAA1 solution.

A further investigation was conducted to determine what value of the η variable would result in the numerical solution closest to the analytic modal solution. Values of 0.0, 0.25, 0.5, 0.75 and 1.0 were tested. Review of the results show that the value of the η variable that provides the results nearest the analytic modal solution varies depending on time and position on the cylinder.

For the front of the cylinder, an η variable value of 0.0, as shown in the first plot Figure II.8, provides results fairly close to both the analytic modal and analytic DAA1 solution for values of normalized time less than four and one half. However, as would be expected with an η value of 0.0, the numerical solution approaches the analytic DAA1 solution at late times. Figures II.9 and II.10 show the results for η values of 0.25 and 0.5. Although they do not match either the analytic modal or analytic DAA1 solutions at early times, they do come closer to matching the analytic modal solution at late times with $\eta = 0.5$ providing the best results.

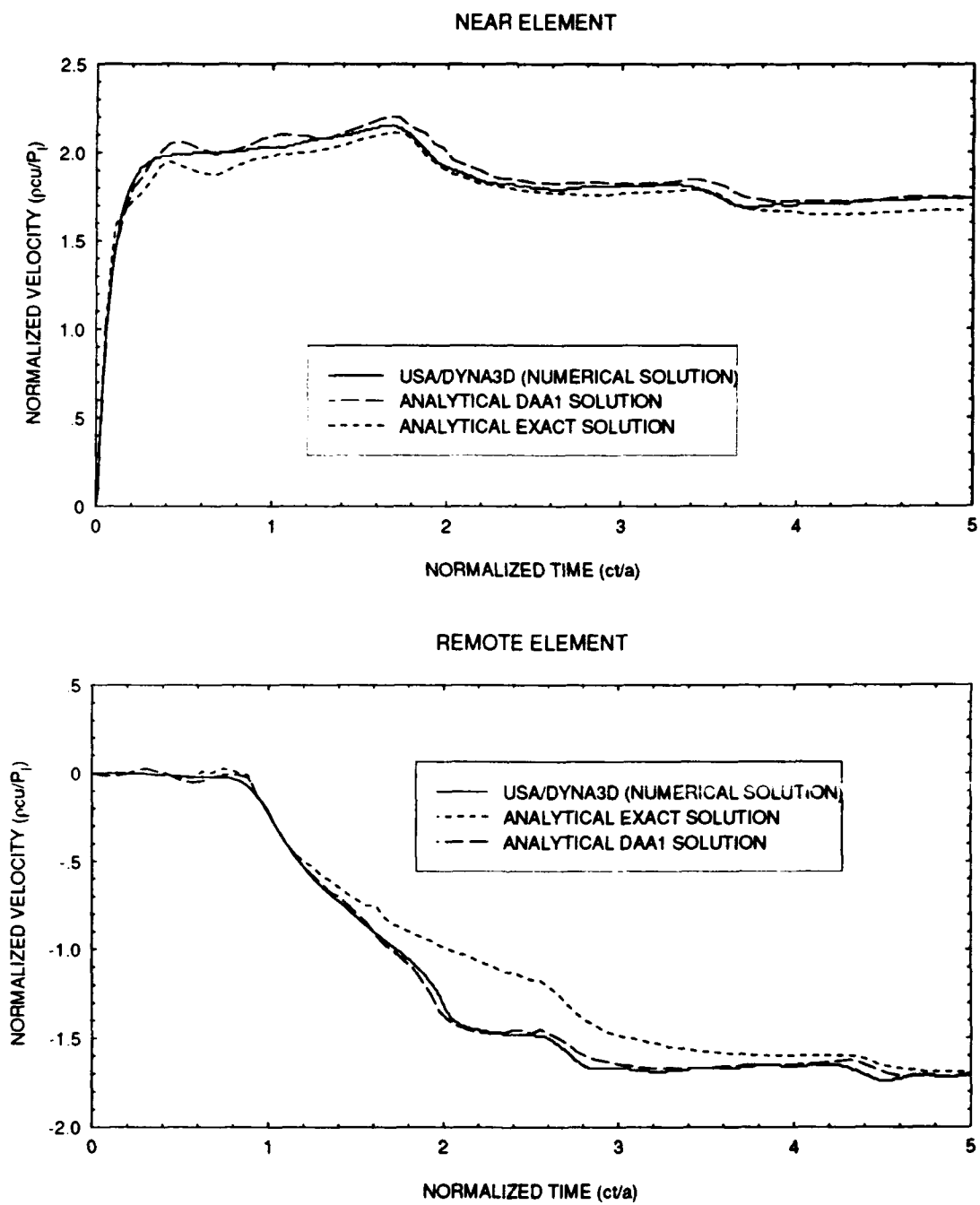


Figure II.8. Infinite cylinder results with $\eta = 0.00$.

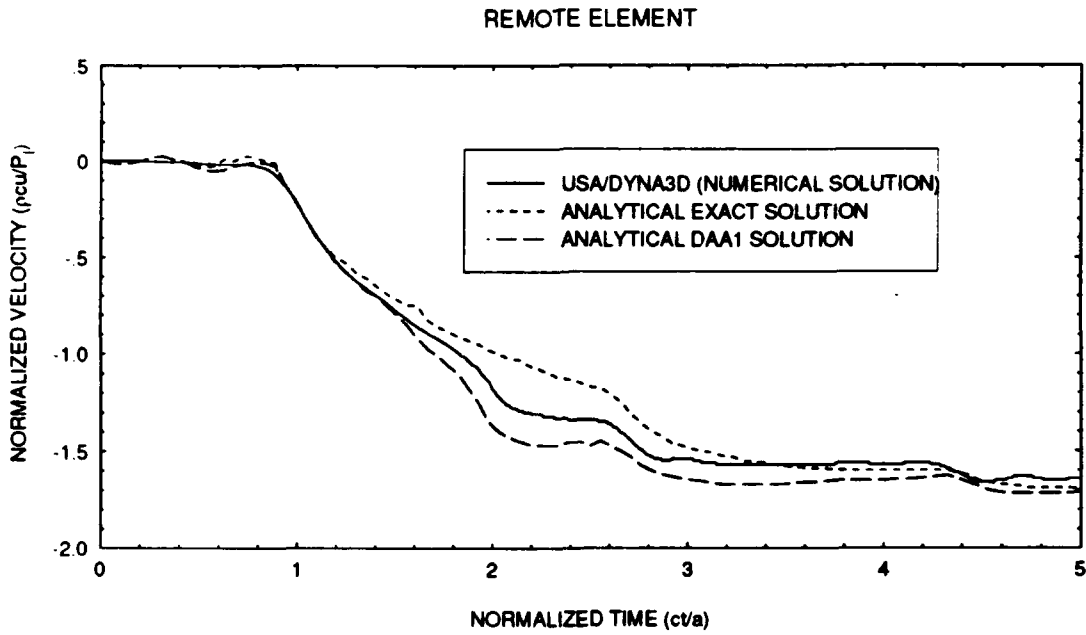
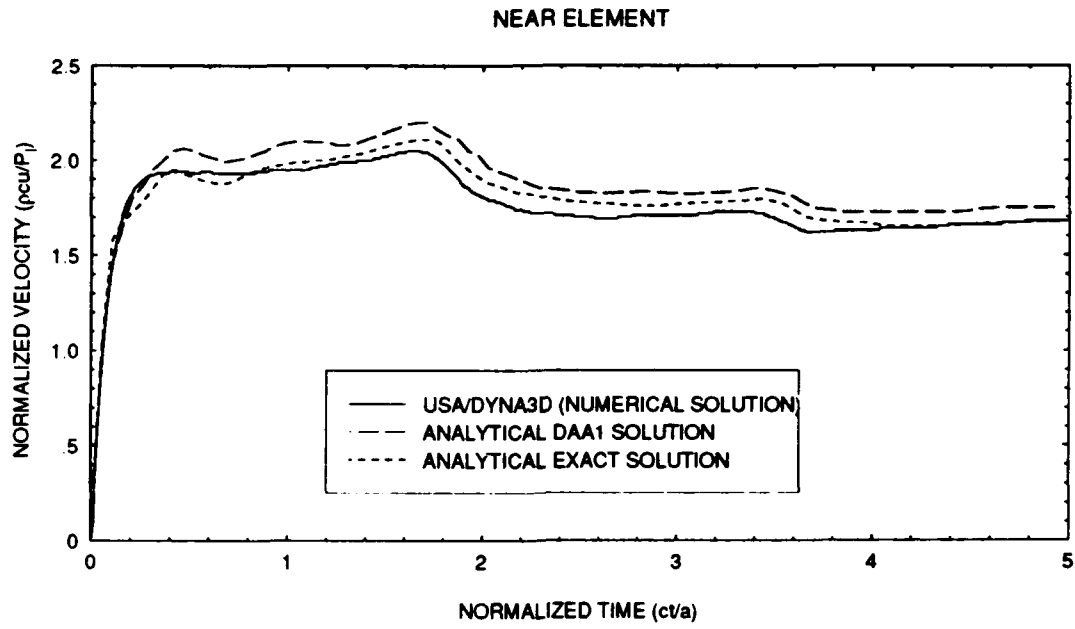


Figure II.9. Infinite cylinder results with $\eta = 0.25$.

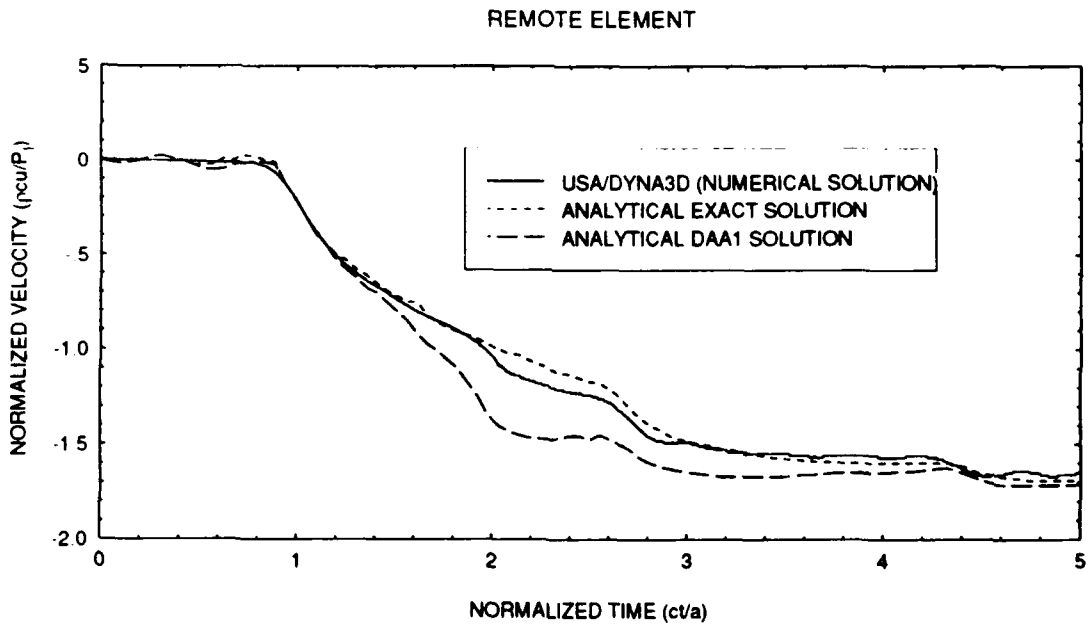
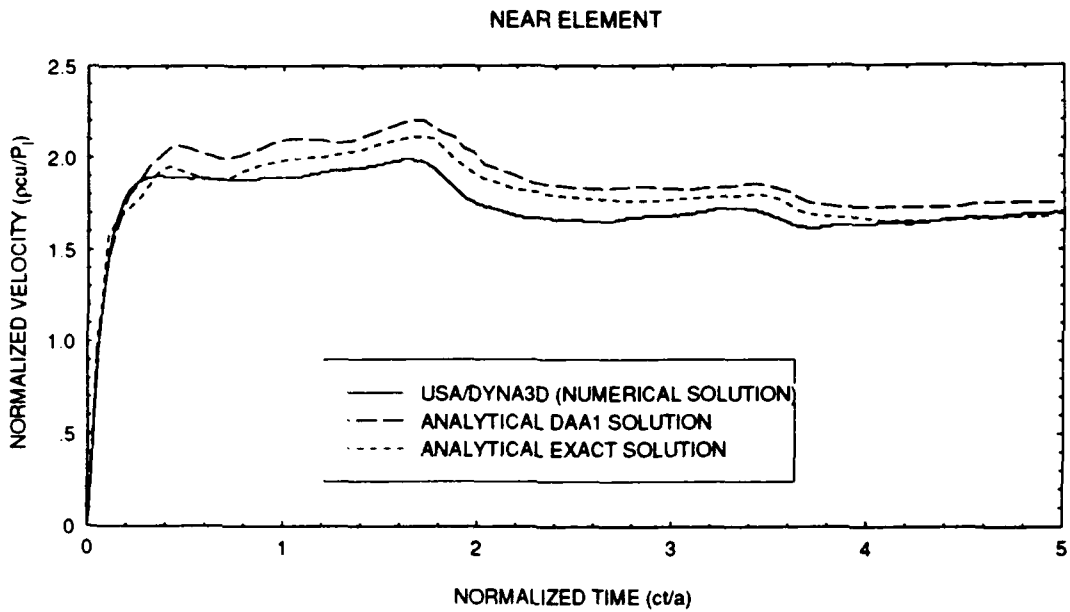


Figure II.10. Infinite cylinder results with $\eta = 0.50$.

On the reverse side of the cylinder, a value of 0.0 provides a result very near the analytical DAA1 solution. Again, this is the expected result with a η variable value of 0.0. However, as can be observed in the second plot of Figure II.8, the numerical solution varies substantially from the analytic modal solution between the normalized time values of 1.0 and 4.0. Values of 0.5, 0.75 and 1.0, as shown in Figures II.10, II.11 and II.12, provide results near the analytical modal solution with 0.75 coming the closest.

Assuming that interest lies in late time results over the entire cylinder, the results show that the best overall value of η for an infinite cylinder lies between 0.5 and 0.75. More compact bodies will have best results with higher η values. Based on the above results, an η value of 0.5 was selected for use for most models used for analyzing the far field problem described in Chapter IV.

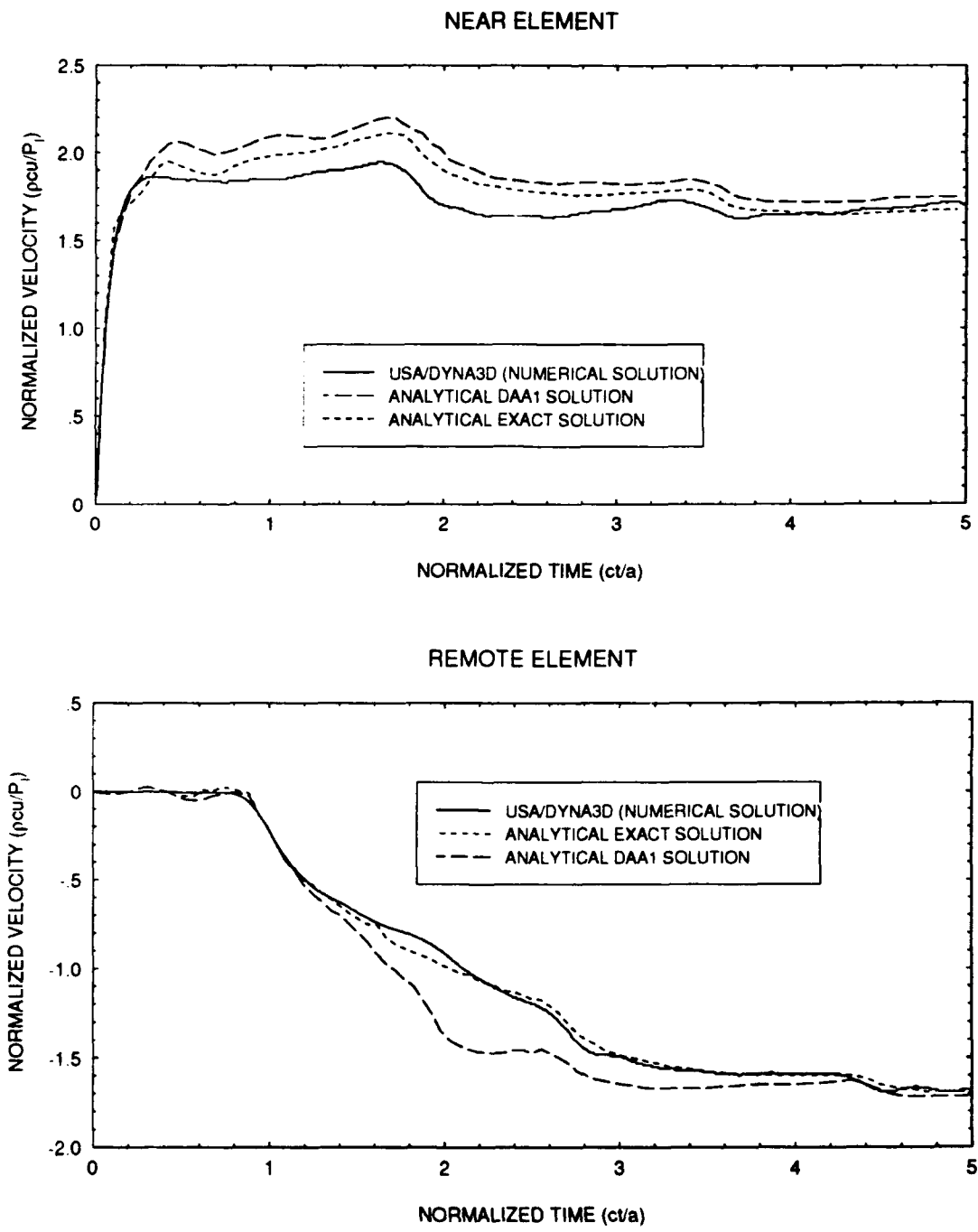


Figure II.11. Infinite cylinder results with $\eta = 0.75$.

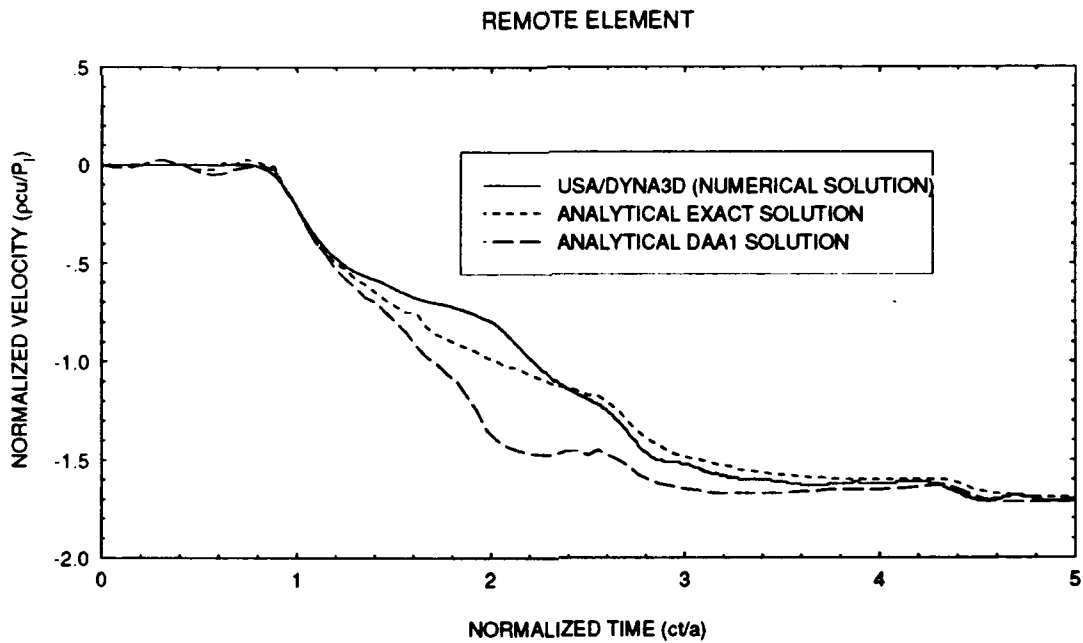
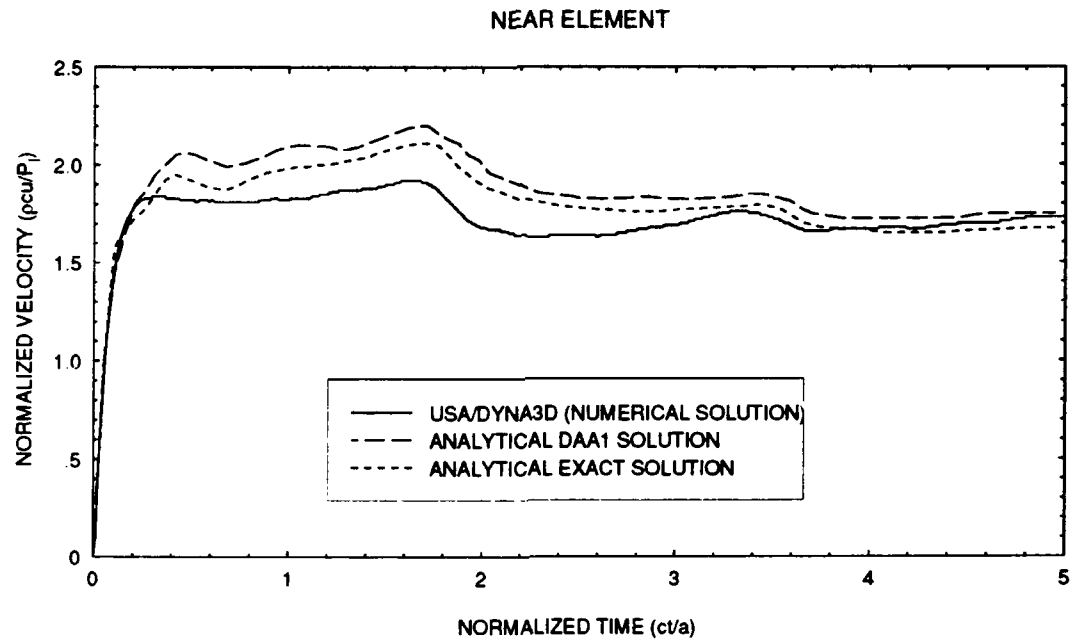


Figure II.12. Infinite cylinder results with $\eta = 1.00$.

III. NEAR FIELD SIDE-ON UNDERWATER EXPLOSION ANALYSIS

A. GENERAL DESCRIPTION AND OBJECTIVES.

The first case studied using the previously described numerical tools was a simple cylinder subjected to a near field side-on explosion. The study included both stiffened and unstiffened cylinders. The main objective of this study was to further the understanding of phenomena associated with a near field explosion. Of specific interest were shock wave propagation, water/shell interaction and nonlinear response of the shell and stiffeners. A clear understanding of these phenomena is required to determine the damage mechanisms that lead to shell collapse. Understanding these factors would ultimately allow the optimization of underwater structures to withstand this type of attack. Since there was no experimental data for comparison, the accuracy of the model is based on observing certain key expected performance parameters. Future studies should include experimental to numerical comparisons to validate the model and its results. The following sections provide a detailed explanation of the models used and provide results obtained from the study. Much of this information has already been published in reference 11.

B. DESCRIPTION OF MODEL USED FOR THE STUDY.

The model used for this study consisted of an explosive charge, a cylindrical shell and the surrounding water. Since the problem setup included a symmetric structure with symmetric loading, quarter symmetry analysis was used to minimize computational effort while providing the greatest opportunity for refinement of the discretization mesh. Different modeling techniques were used for each section of the model. Figure III.1 shows the combined quarter symmetry model used for the analysis.

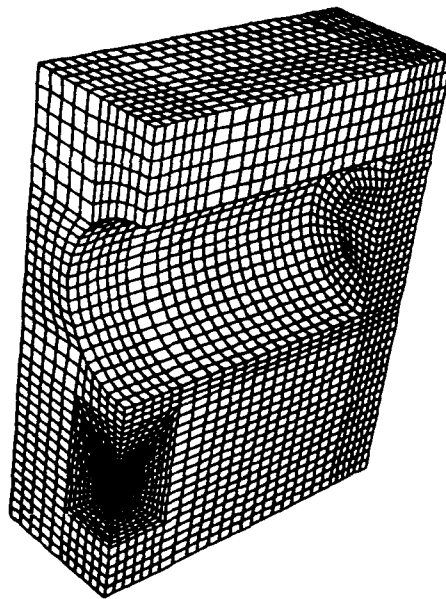


Figure III.1. Quarter symmetry model for near field side-on attack analysis.

1. CYLINDER MODEL

The quarter symmetry discretization of the cylindrical shell is shown in Figure III.2. The discrete model represents a physical cylinder with a 42 inch length and 12 inch diameter. The axial surface is one quarter inch thick and each end plate is has a one inch thickness. For the stiffened model, two one eighth thick by one inch high circumferential stiffeners were spaced equidistantly within the shell.

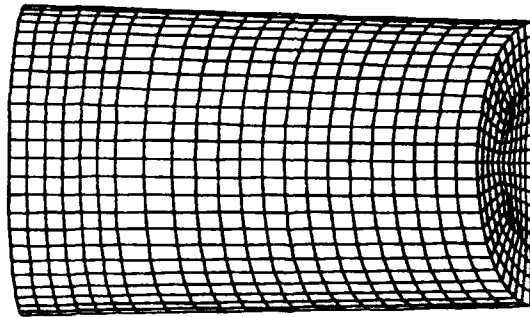


Figure III.2. Shell quarter symmetry discretization for near field side-on attack analysis.

The material selected for the analysis had a yield strength of 43 KSI and a Young's modulus of 10800 KSI. An elastic-plastic constitutive model with no strain or strain-rate hardening was selected. The constitutive model and material properties are consistent with 6061-T6 aluminum. The end plates are considered to be rigidly attached to the shell.

The Belytschko/Lin/Tsay element formulation was used for the model. This formulation was selected for its computational efficiency and high degree stability in the presence of large deformations. The theory associated with this formulation is discussed in reference 12.

2. EXPLOSIVE CHARGE

The shock wave for the study was provided by an explosive charge placed with its center located one foot below the geometric centroid of the cylinder. This resulted in a six inch standoff distance between the center of the charge and the surface of the model.

The Jones/Wilkins/Lee (JWL) equation of state was used to model a one inch radius pentolite charge for the unstiffened study. A slightly larger charge with a radius of 1.2 inches was used for the stiffened model. The JWL equation of state as stated below:

$$P = A\left(1 - \frac{\omega}{R_1 V}\right)e^{-R_1 V} + B\left(1 - \frac{\omega}{R_2 V}\right)e^{-R_2 V} + \frac{\omega E}{V}$$

determines the pressure generated by the charge. It has an empirical basis and is commonly used to model the detonation products of high explosives. The coefficients A , B , C , R_1 , R_2 and ω are experimentally derived and tabulated for each type of explosive. Additional information concerning the JWL equation of state can be found in reference 13.

Since the explosive charge has a physical volume, it is consumed at a rate governed by its burn rate and distribution about the detonation point. The combination of the equation of state with the finite burn time generates a shock wave in the surrounding media that is a function of explosive material weight, explosive material distribution, time, and distance from the charge. The quarter symmetry discretization of the explosive charge is shown in Figure III.3. The quarter charge is composed of 1296 solid elements. The extremely fine discretization was necessary to ensure spherical propagation of the shock wave while still maintaining a coherent mesh as the explosive material expanded in the surrounding water.

3. SURROUNDING WATER

As stated earlier, the boundary element method is not considered to be suitable for modelling for the near field case because of the fundamental theory that forms the basis of the doubly asymptotic approximation. As a result, the

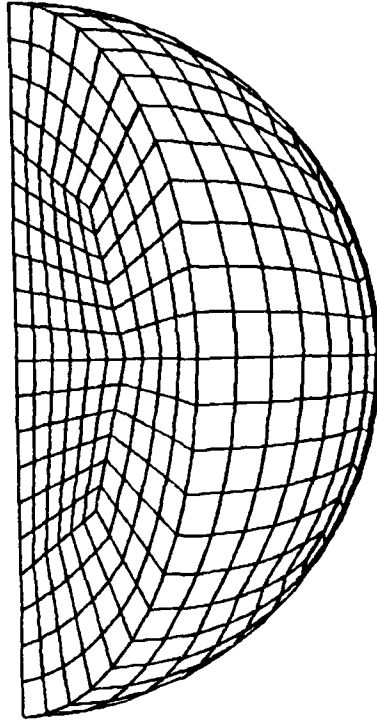


Figure III.3. Explosive charge quarter symmetry discretization for near field analysis.

surrounding water medium was discretized using the finite element method.

The water media discretization can be seen in Figure III.1. Even though quarter symmetry was used, the mesh still consists of 11640 solid elements. This proved to be a significant limitation in the use of the finite element method for the study of the underwater explosion phenomena. This limitation occurs because any increase in distance between the cylinder and the charge results in a significant penalty in the form of additional computational time and storage requirements as the size of the water medium was expanded to

accommodate the charge and cylinder. This problem can be overcome by the use of brute force - i.e. the use of larger and faster computers. However, this results in significant increases in cost in the performance of required studies. Fortunately, the boundary element method discussed in chapter II can be used at distances only slightly greater than the one foot distance used for this study.

The water was modelled as an infinite medium. Since an infinite medium cannot be discretized, the infinite case was modelled using a finite volume bounded by non-reflecting boundaries. The non-reflecting boundaries cause a travelling wave to damp out so that there is no reflection from the boundary surface. The non-reflecting boundary was used on four sides of the water volume. The other two sides were symmetric boundaries since quarter symmetry was used in the problem.

The Gruneisen equation of state was used to model the surrounding water. Since water cannot withstand a tensile force, a slightly positive pressure cut off was used in addition to the Gruneisen state equation to determine when cavitation occurred in the fluid. The pressure cutoff prevents the occurrence of physically impossible negative pressures in the water media.

C. RESULTS OF THE NEAR FIELD STUDY

1. FREE FIELD TRANSMISSION AND SHELL WATER INTERACTION

Figure III.4 shows the water mesh located between the charge and the nearest point of the cylinder to the shell.

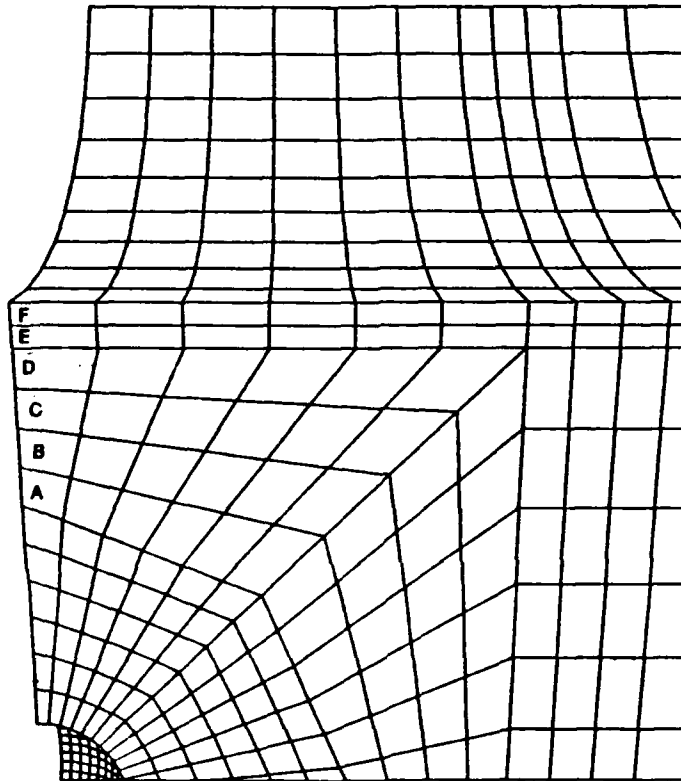


Figure III.4. Location of specified elements for near field analysis.

The pressure histories for elements designated A through F in Figure III.4 are plotted in Figure III.5. Unless otherwise stated, time scales are in microseconds and pressure and stress scales are in grams per $cm-\mu\text{sec}^2$. Of the water elements shown in Figure III.4, element A is nearest the charge

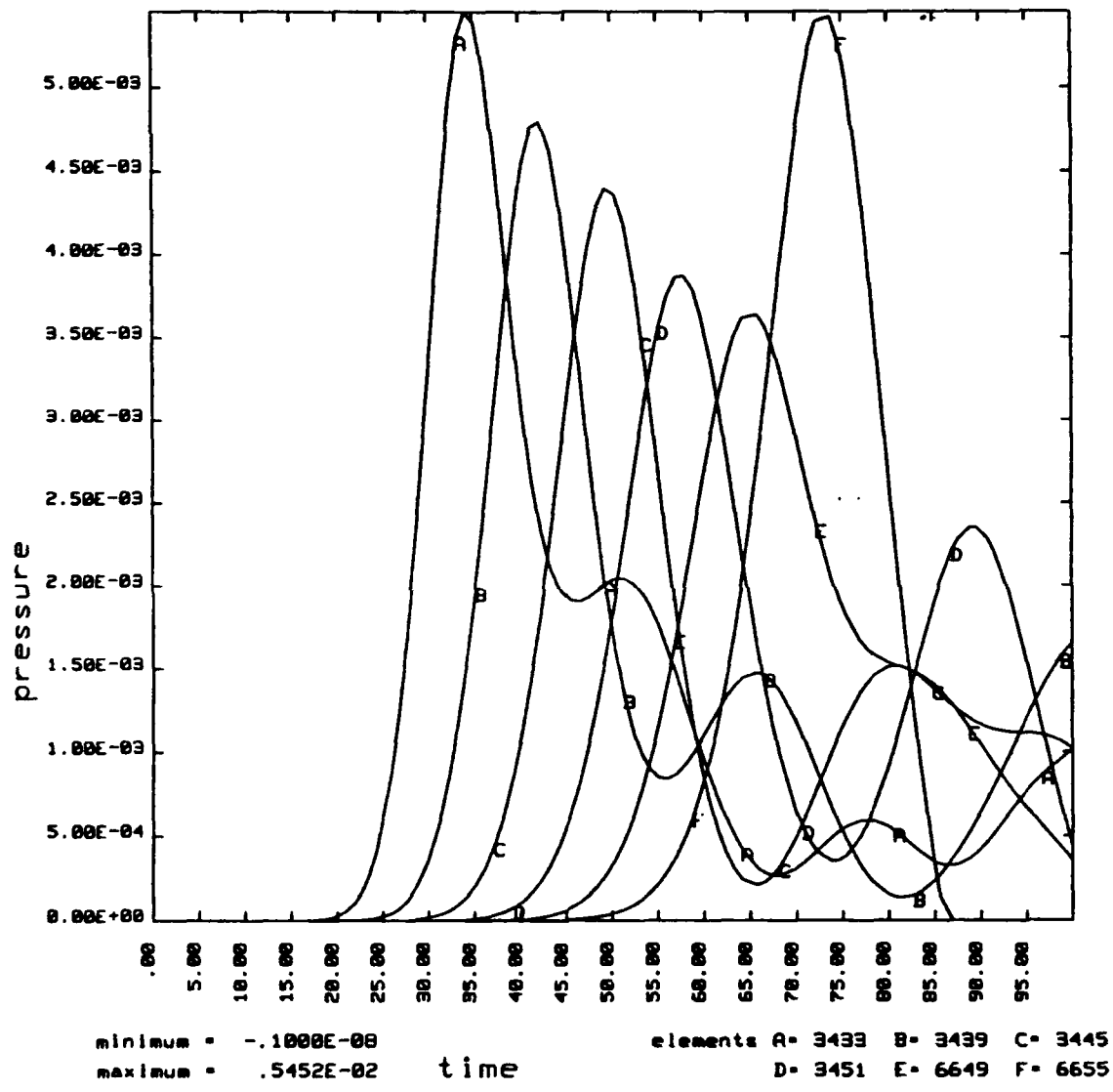


Figure III.5. Pressure-time history for specified water elements for near field analysis.

and element "F" lies next to the structure. Several observations can be made on the basis of the Figure III.5 plot. First, the free field peak pressure (elements "A" through "E") drops as distance from the charge increases. The rate of decrease is slightly less than the $1/R$ reduction expected for a spherical charge. This deviation can be attributed to the nearness of the charge. Element "A" is between two and three charge radii from the charge while element "E" lies between five and six charge radii from the charge. Normally, the $1/R$ performance is expected to hold outside ten charge radii from the charge. Nearer distances are expected to decrease at less than the $1/R$ rate. Therefore, the pressure decrease with respect to distance from the charge is considered to be physically correct for this situation.

The second observation is that the pressure suddenly increases in element "F". This is an expected phenomena. By using Snell's law, it can be shown that pressure will double at the water/structure interface when an acoustic wave impinges on a rigid structure. In this case, the pressure did not completely double. The reduction in the peak can be attributed to two factors. First, the pressure provided for the element is an average of the entire element. In theory, the doubling only occurs at the water/structure interface.

Since the pressure in the other areas of the element are lower than at the actual interface, the average for the element will be lower than the interface pressure. Second, the structure is not completely rigid as assumed by the theory that predicts the doubling. As a result, the reflected pressure will be somewhat less than double the pressure of the impinging acoustic shock wave.

It can be further observed that the pressure in element "F" drops rapidly to zero after peaking. This occurs because the impact of the shock wave on the shell surface causes the shell to deform inward at a speed higher than the adjacent water. Since water is highly incompressible, this velocity differential causes a rapid drop in pressure which in turn leads to a significant area of local cavitation. Figures III.6 and III.7 show the sudden pressure rise caused by the shock wave reflection and subsequent cavitation in the form of fringe plots. In the fringe plots, the darker areas represent areas of higher pressure and similarly, the lighter areas represent areas of low pressure.

Finally, it can also be observed in Figure III.5, that the reflected shock wave travels back toward the originating explosive charge. As stated previously, the reflected peak is visible in "F" as the rapid increase in pressure. In element "E", it is shown by the flattening and then continued drop of

time = .75000E+02
 fringes of pressure
 min = -1.000E-09 in element 12936
 max = 5.012E-03 in element 6559

fringe levels
 7.680E-04
 1.637E-03
 2.586E-03
 3.374E-03
 4.243E-03

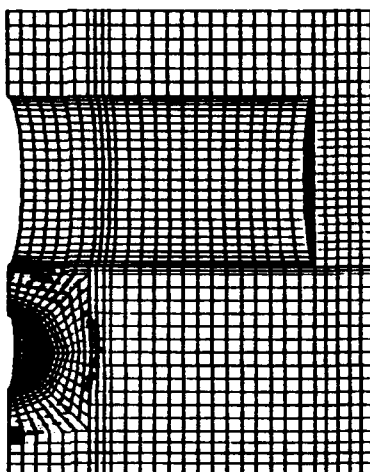


Figure III.6. Pressure fringe plot as the pressure wave strikes the nearest shell surface.

time = .10000E+03
 fringes of pressure
 min = -1.000E-09 in element 12934
 max = 1.987E-03 in element 6597

fringe levels
 2.920E-04
 6.230E-04
 9.530E-04
 1.294E-03
 1.614E-03

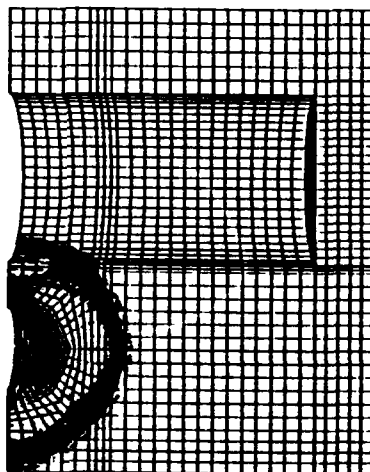


Figure III.7. Pressure fringe plot as cavitation occurs in water near the shell surface.

the pressure plot starting at 75 microseconds. The cavitation next to the shell prevents the pressure in element "E" from developing into a peak. The reflected peak is clearly visible in the element "D" plot at 90 microseconds and can be seen to be developing first in "B" and then in "A" at 100 microseconds. There are several key facts to note here. First, the height of the reflected peaks decreases as distance increases from the point of reflection. Second, the peaks show up in elements near the shell before they show up in elements further from the shell. In other words, as would be expected, elements are affected in the reverse order that they are affected by the incident shock wave. Element "C" appears to be an anomaly to this trend since no reflected pressure peak develops for "C" between the peaks for "D" and "B". However, careful observation shows that the leveling off of the "C" element pressure plot is caused by the arrival of the rising reflected wave at the same time as the second peak of the incident pressure wave is decreasing. The result is a cancellation effect, and the reflection peak does not develop.

Several other observations were made with regard to the free field pressure propagation and water/shell interaction. First, the free field pressure dissipates very quickly. By the time the shock wave has expanded to a point halfway up the side of the shell, the peak pressure has

already dropped to a value that is 20% of the free field pressure at element "E". By the time it reaches the most remote point on the shell midway between the two ends, the peak pressure has further dropped to seven percent of the peak value in element "E". These values are consistent with the 1/R thumb rule for peak pressure reduction for a spherical charge. The value at the remote side is a little low, but this can be attributed to shadowing by the cylinder.

2. SHELL RESPONSE

a. UNSTIFFENED MODEL

Figures III.8 and III.9 are fringe plots showing the propagation of stress in the shell shortly after initial impact of the shock wave with the shell. It can be observed that the stress propagation is initially a quarter circular shape. This is the result of quarter symmetry with elastic deformation. However, as plastic deformation begins in the shell, the stress pattern develops into the mushroom shape shown in Figure III.9. This mushroom shape is caused by a combination of two effects. First, the shock wave is causing the cylinder to bend globally at the center like a beam. This tends to put the whole thickness of the surface area nearest to the charge into compression. This effect decreases as the vertical distance between the location on the shell and the

time = .90000E+02
fringes of eff. stress (v-m)
min= 2.532E-09 in element 195
max= 4.100E-03 in element 4

fringe levels
6.290E-04
1.339E-03
2.050E-03
2.760E-03
3.471E-03

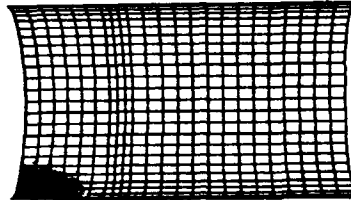


Figure III.8. Propagation of Von Mises stress at 90 microseconds (30 microseconds after pressure wave impact).

time = .15000E+03
fringes of eff. stress (v-m)
min= 4.884E-09 in element 551
max= 4.100E-03 in element 1

fringe levels
6.290E-04
1.339E-03
2.050E-03
2.761E-03
3.471E-03

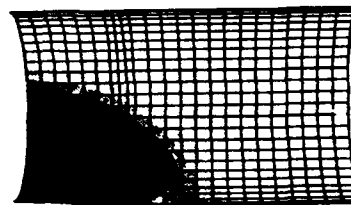


Figure III.9. Mushroom shaped propagation of Von Mises stress at 150 microseconds.

neutral plane of the cylinder decreases. It also decreases as the location gets closer to the ends since the maximum moment will occur at the centerline between the two end plates. At same time, the shock wave is deforming the surface in a circular pattern. This tends to relieve the compressive stress along the bottom of the cylinder in the vicinity of the shock wave impact. The same deformation tends to reinforce the compressive strain along a circumferential line running through the near point perpendicular to the axis. This in turn causes the mushroom shaped pattern observed in Figure III.9. As the pressure wave continues along the surface of the cylinder nearest to the charge and circumferentially around the cylinder surface, the mushroom grows. As the shock wave passes the end of the cylinder, the pattern resumes its former quarter circular shape.

Although the stress pattern changes shape, the effective plastic strain changes only marginally from a quarter circular shape to a quarter elliptical shape with the major axis in the same direction as the axis of the cylinder. This is consistent with the above description since the strain pattern covers a relatively small area of the lower part of the cylinder and tends to spread after the mushroom stem has already passed the deforming location.

Since the speed of sound in aluminum is higher than in water, the stress wave propagated through the cylinder faster than through the water. As a result, it took only 120 microseconds for the stress wave in the aluminum to arrive at the point on the mid shell circumference most remote from the charge while it took 200 microseconds for the wave to propagate to the same point through the water medium. Based on a linear travel distance of one foot and an acoustic velocity of 5000 ft/sec in water, the 200 microseconds appears correct. A similar check of expected travel time through aluminum based on an acoustic velocity of 15000 ft/sec with a circumferential travel distance of 1.5707 feet indicates that the 120 microseconds is slightly longer than the expected 105 microseconds. However, plot states were taken only every 20 microseconds. Therefore, if arrival occurred just after the previous plot state was recorded, it is possible for timing to be off by as much as 20 microseconds. The 15 microsecond difference noted above falls well under the 20 microsecond plot state difference.

Mid plane effective (Von Mises) stress and effective plastic strain were plotted for selected locations. Effective plastic strain is defined by the relation:

$$\bar{\epsilon}_p = \frac{\sqrt{2}}{3} [(e_{p1} - e_{p2})^2 + (e_{p2} - e_{p3})^2 + (e_{p3} - e_{p1})^2]^{\frac{1}{2}}$$

with ϵ_{p1} , ϵ_{p2} and ϵ_{p3} representing the true plastic strain components [Ref. 9]. Figures III.10 and III.11 show the results for the shell elements nearest the charge. Based on comparison of the two plots, it is apparent that it took approximately 30 to 40 microseconds for the stress to build to the yield stress level. Once yield stress was attained, stress did not change since the perfectly plastic material model with no strain or strain rate hardening was used for the analysis. It is also clear from comparison of the two plots that plastic deformation continued as long as the material remained at the yield stress level. Plastic deformation discontinued and remained constant when the stress dropped below the yield level. Since the strain plotted was effective plastic strain, no strain reduction or unloading occurred as the material stress was reduced. It is also apparent from the effective strain plot that the initial loading period is the most important. Even though the stress remained at the yield stress for most of the first 1300 microseconds following initial impact of the shock wave, over 80 percent of the strain occurred in the first 100 microseconds following initial impact.

The significant dip in stress which occurs near 1000 microseconds occurs when there is a change in axial

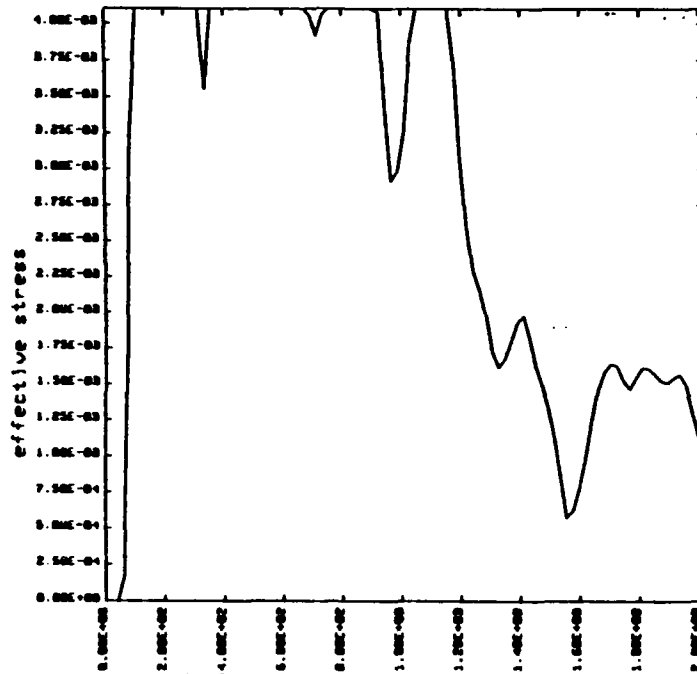


Figure III.10. Nearest element stress history for near field analysis.

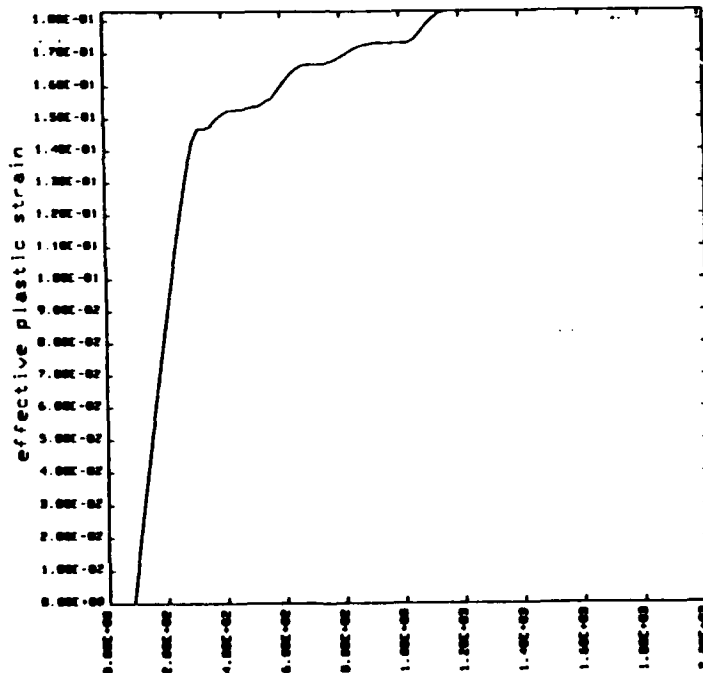


Figure III.11. Nearest element effective plastic strain time history for near field analysis.

direction of the two end plates. As the relative displacement between the two end plates becomes zero, the stress is relieved. As the relative displacement continues, the stress once again builds.

Similar plots are provided for the shell elements located 90 and 180 degrees along the circumference from the nearest shell element. The element at 90 degrees will be called the mid element and the one at 180 degrees will be called the remote element.

The plots for the mid element are Figures III.12 and III.13. Again, once the stress build up starts, it takes approximately 30 microseconds for the stress to reach yield stress. The mid element spends very little time at yield stress. As a result, the effective strain remains constant throughout the time of analysis. It should be noted that the damage mechanism is different for this element than the near element. The primary damage mechanism for the near element was the force of the shock wave impinging on the structure. However, as stated earlier, the water shock wave effect is significantly reduced by the time it reaches the mid element. Most of the stress at the mid element is caused by the global deformation of the cylinder. The cylinder tends to bend at the center much as a beam is loaded in one direction at the

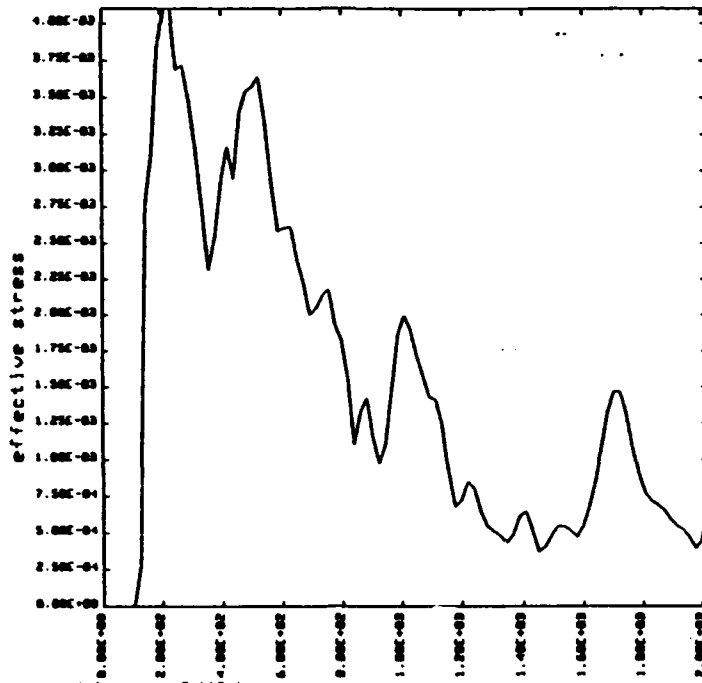


Figure III.12. Mid element Von Mises stress time history for near field analysis.

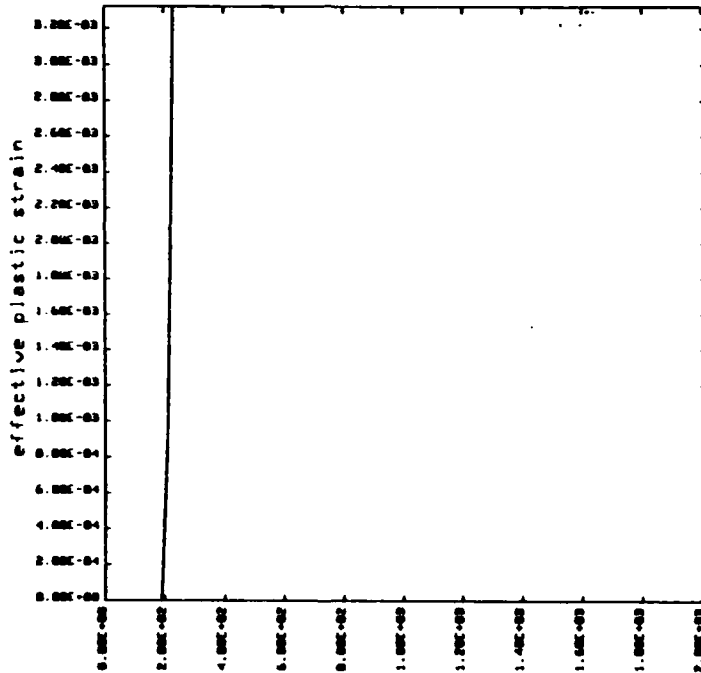


Figure III.13. Mid element effective plastic strain time history for near field analysis.

center and in the other direction at the ends. In addition, the surface at the mid element is forced to bulge outward by the movement of the near element upward toward the remote element. As a result, the mid element ends up in tension in both the axial and hoop directions. However, since the mid element is half way between the near and remote elements in a plane perpendicular to the direction of shock wave travel, the overall effect is minimal resulting in relatively small effective plastic strain.

The final set of stress and strain plots for the near field analysis are for the remote element. They are shown in Figures III.14 and III.15. As in the mid element, the shock wave in the water at this location is mostly dissipated. As a result, this is not a major damage mechanism at the remote element. However, two other factors appear to be important. First, the shock wave travels circumferentially through the shell direction in the two semi-circular paths from the nearest element to the remote element because of the symmetry. This causes an intensification of stress at the most remote element. This intensified stress corresponds to the sharp peak in Figure III.14. This intensification can also be seen in the fringe plot of Figure III.16.

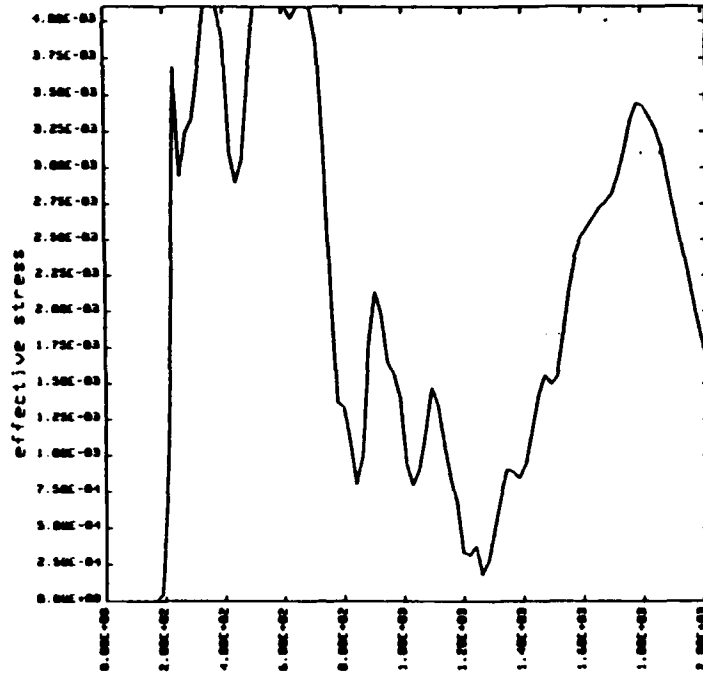


Figure III.14. Remote element Von Mises stress time history plot for near field analysis.

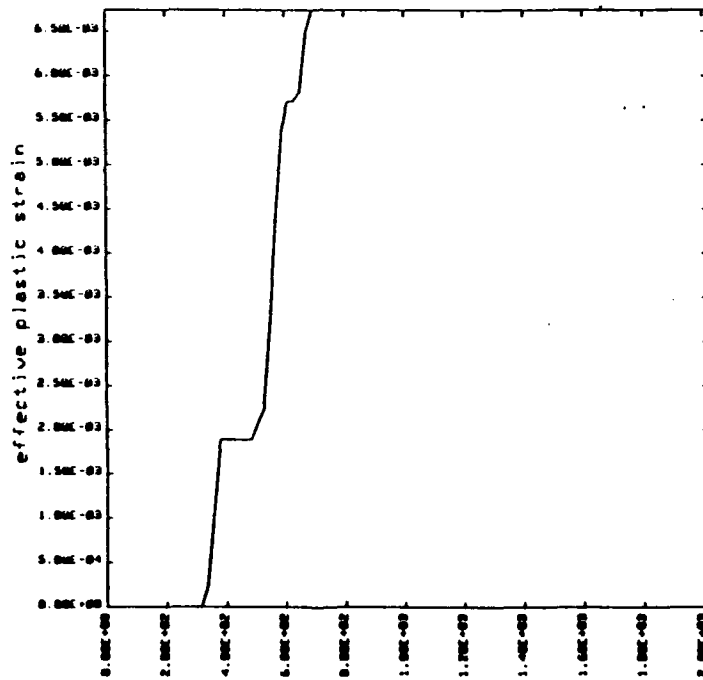


Figure III.15. Remote element effective plastic strain time history plot for near field analysis.

The second, and probably most important damage mechanism for the remote element is the beam bending type stress placed on the cylinder. This causes a high tensile stress in the axial direction in the remote element while the flattening of the cylinder caused by the deformation at the center on the near side places a relatively high compressive stress in the hoop direction.

time = .23200E+03	fringe levels
fringes of eff. stress (v-m)	6.310E-04
min= 2.859E-06 in element 271	1.341E-03
max= 4.100E-03 in element 33	2.051E-03
	2.762E-03
	3.472E-03

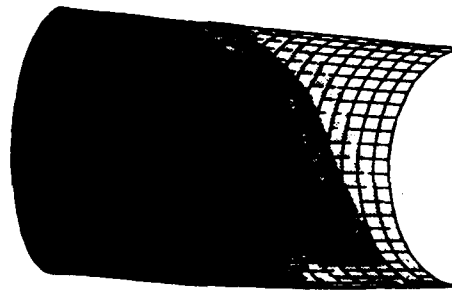


Figure III.16. Stress intensification in remote element during near field attack.

The entire deformation occurs very rapidly and is so extreme that very little oscillatory response is seen in the structure. The only oscillatory response noted was at a very low frequency (approximately 500 Hz) in the axial direction. No whipping or breathing modes were noted. This

will be contrasted to the far field model later in this document. The final deformed shape of the cylinder is shown in Figure III.17.

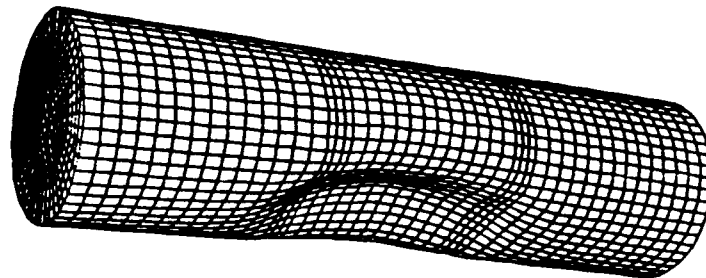


Figure III.17. Final deformed condition of cylinder for near field attack.

It should be noted that no material failure model was used for this analysis. The maximum effective strain was in the neighborhood of 18 percent. Such large strains could result in material failure if a failure model was considered.

b. STIFFENED MODEL

Figure III.18 shows the final deformed shape for a stiffened cylinder. Damage modes for the shell are very similar to the modes noted for the unstiffened cylinder. However, the stiffened cylinder withstood a larger charge at the same standoff distance.

The only additional information found in this portion of the analysis was the failure mode of the stiffener. It can be clearly seen in Figure III.18 that the stiffener fails by local buckling (tripping). This is the expected mode of failure. This observation clearly demonstrates that it is important to provide lateral stiffeners to stabilize the circumferential stiffeners if maximum effect is to be obtained from the circumferential stiffeners.

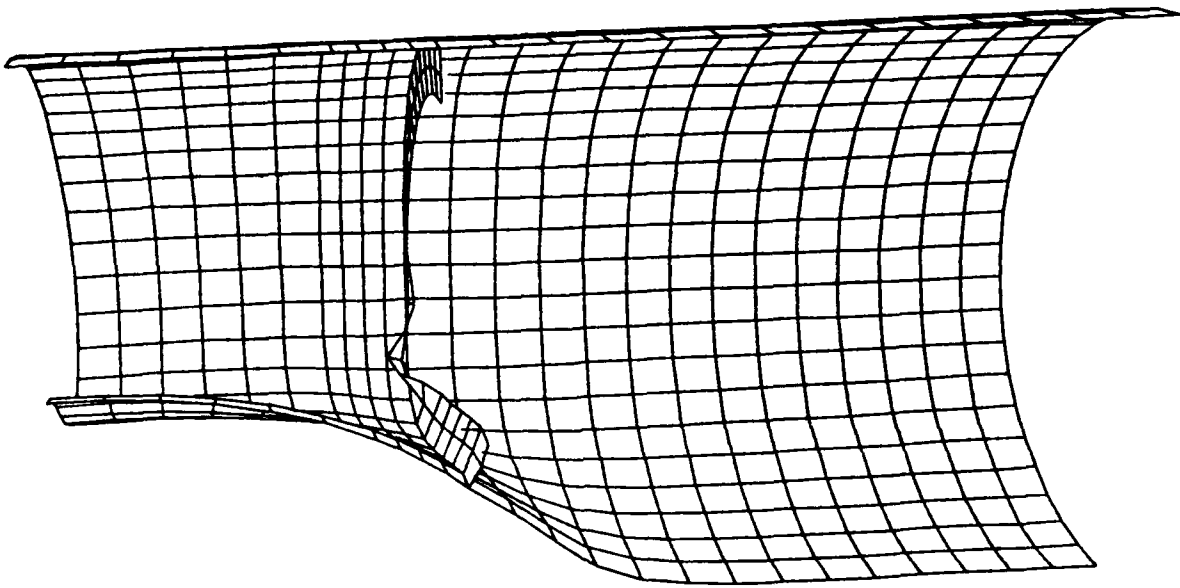


Figure III.18. Stiffener failure by tripping in near field attack stiffened model.

IV. FAR FIELD SIDE-ON EXPLOSION ANALYSIS

A. GENERAL DESCRIPTION AND OBJECTIVES

This study compared predictions obtained from a numerical analysis to the results obtained from an underwater explosion test. There were two main objectives. The first was to determine if numerical methods can adequately model the non-linear response of a simple cylinder subject to a side-on underwater explosion. If a close correlation is shown, this study could be used as a stepping stone to the study of more complex structures and materials with the final objective of using this type of modelling as a research tool for understanding the response of ships and submarines to underwater explosions and as a design tool for optimizing ship and submarine hull structures. Included in this portion of the study were various sensitivity analyses to determine the relative importance of various physical and numerical modeling factors on the final results. By doing this, it was hoped that some insight could be gained in improving future modelling efforts.

The second objective was to study the non-linear response of the shell in an effort to obtain a better understanding of the possible modes of failure and response modes of the

cylinder. As in the near field attack, this understanding is necessary to be able to predict the sudden collapse of a cylinder subjected to underwater far field explosions. Such an understanding would ultimately allow the optimization of underwater structures to withstand this type of attack.

B. DESCRIPTION OF MODELS USED FOR THE FAR FIELD STUDY AND EXPERIMENTAL METHOD

1. PHYSICAL MODEL

The physical model was an unstiffened right circular cylinder with the following characteristics.

Dimensions:

Length	42 inches (1.067 m)
Diameter	12 inches (0.305 m)
Weight	60.5 pounds (27.5 Kg)

Materials:

Shell	1/4 inch thick 6061-T6 Aluminum (0.64 cm)
End Plates	1 inch thick 6061-T6 Aluminum (2.54 cm)

The cylinders used for this test were constructed from commercially available material. Fabrication was performed at the Naval Postgraduate School. The end plates were welded to the shell using a Tungsten Inert Gas (TIG) process.

The 6061-T6 aluminum was selected on the basis of its high strength and strain rate insensitivity. The material properties of the aluminum used for the shell were verified using the MTS machine at the Naval Postgraduate School. Results of tensile testing determined that the material properties were near nominal with a Young's modulus of 10800 ksi (75.6 GPa) and yield strength of 43 ksi (300 MPa).

2. UNDERWATER EXPLOSION TEST

The underwater explosion test was performed at the Dynamic Testing Incorporated (DTI) facilities in Rustburg, Virginia. The facility is in a quarry and the depth of the water is approximately 130 feet (39.6 m) at the location of the test. As a result, bottom reflection was not a factor in the test.

The charge used for the test was 60 pounds (27.3 Kg) of HBX-1. The peak pressure generated by the charge was 2360 psig (16.3 MPa) which was substantially lower than the calculated peak pressure of 2680 psig (18.5 MPa) for the 60 pound (27.3 Kg) charge at a 25 foot (7.62 m) standoff distance. The test charge was activated by a radio control device.

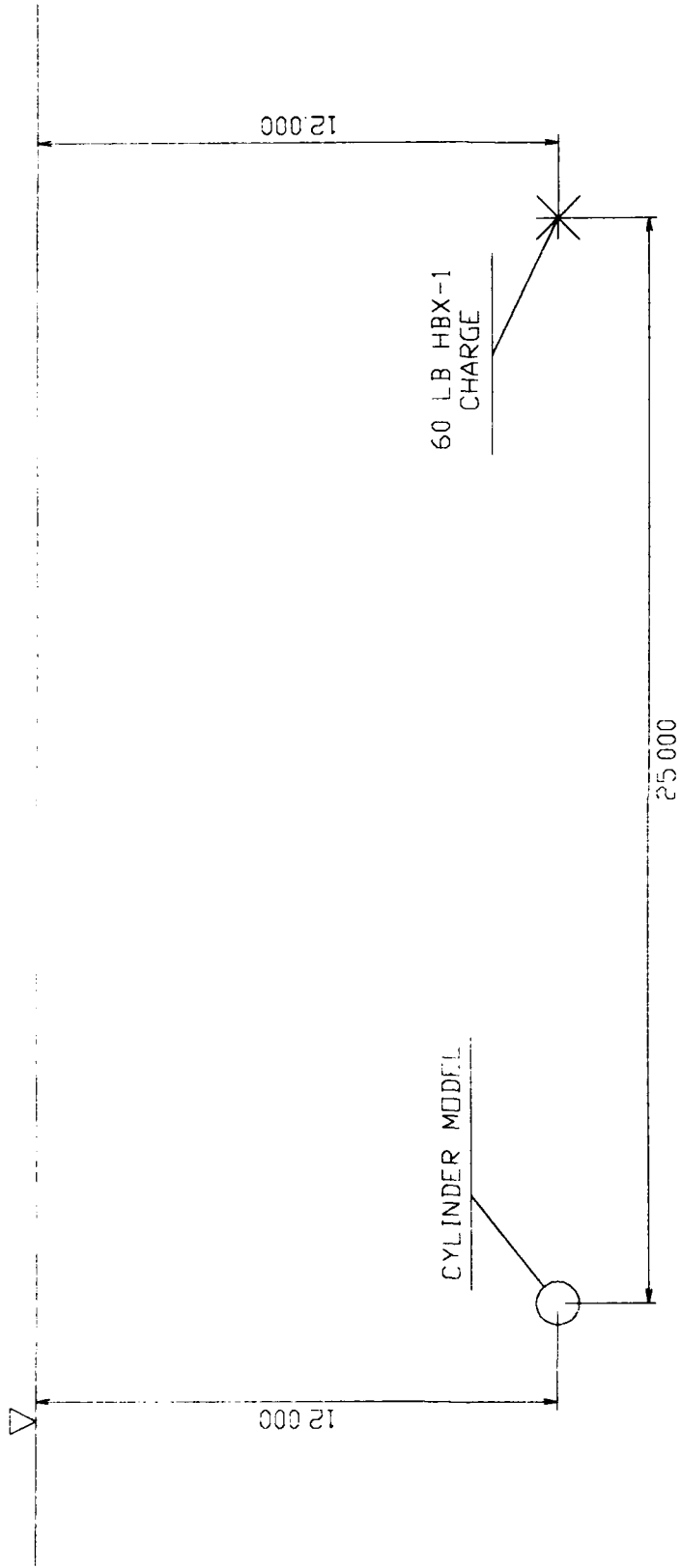
The test depth for both the charge and the cylinder was 12 feet (3.66 m). This depth allowed the bubble generated by the explosion to vent at the surface prior to encountering

the cylinder and eliminated the possibility of a bubble pulse. In addition, the 12 foot (3.66 m) depth provided a clear pressure cutoff.

The cylinder was held in place with a crane rig and the charge was suspended from a float. Distance and alignment of the charge to the cylinder was established and maintained using a tensioned span wire from the charge float to the cylinder support rig. Post-shot calculations found the arrival time of the shock wave to be consistent with a distance of 25 feet (3.66 m) and sound of speed in water of 4800 ft/sec (1463 m/s). Test profile and arrangement are provided as Figures IV.1 and IV.2.

Strain measurement was performed using CEA-06-250UW-350 strain gages. These are general purpose strain gages with an optimum range of ± 1500 microstrain and are good for both static and dynamic test measurements. The strain gages were bonded to the cylinder using a M bond 200 by a instrumentation technician employed by DTI. All pre-shot calibration and connection were performed by DTI technicians.

The test called for 14 total strain gages (seven to measure hoop strains and seven to measure axial strains). Of the fourteen strain gages, three failed. The dynamic range of the test exceeded the optimum range of the strain gages by a significant factor. This is the most probable cause of the



NOTE: DISTANCES IN FEET

Figure IV.1.1. Under test profile.

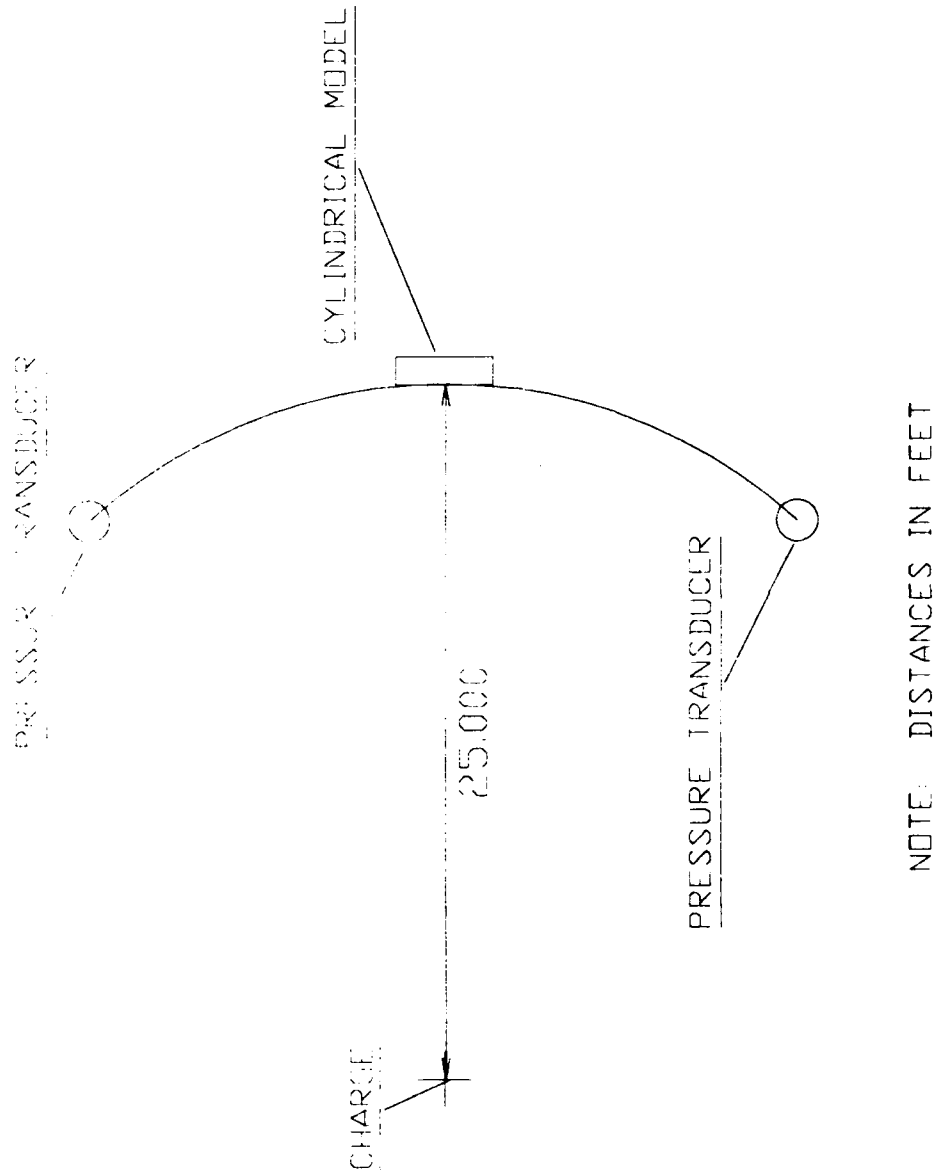


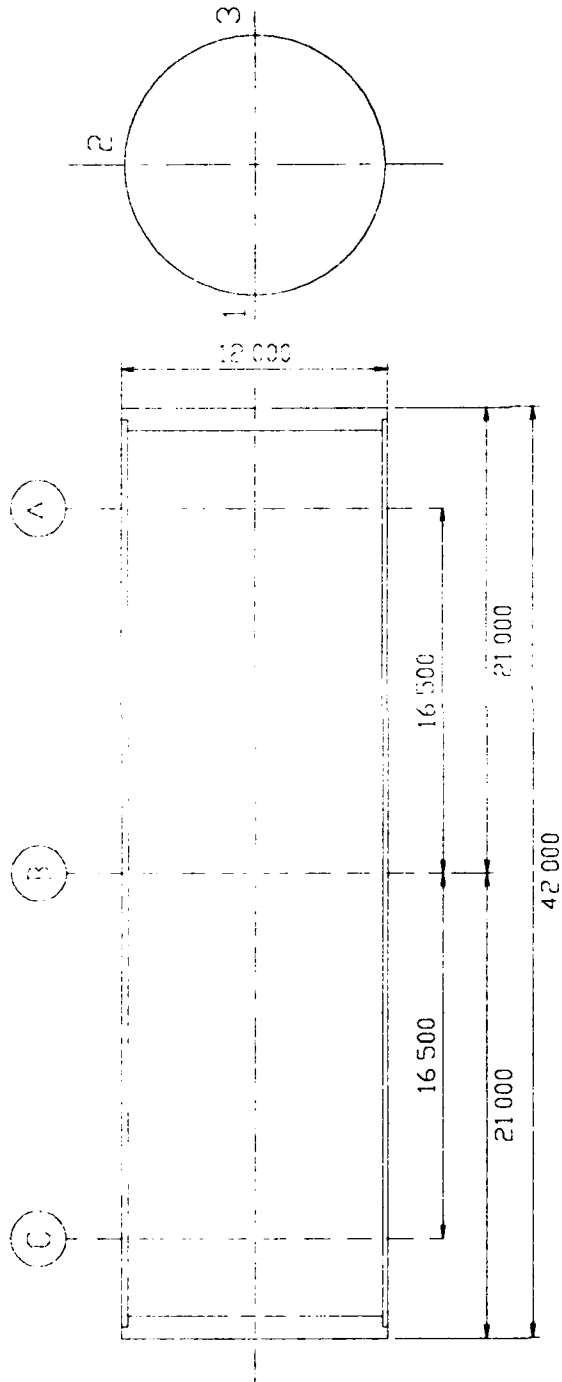
Figure IV.2. Undex test general arrangement.

high strain gage failure rate. The instrumentation diagram for the test is provided as Figure IV.3. The strain gage located at B1 was placed nearest the charge during the test. Strain gage output was filtered at 2000 Hz. Locations noted on Figure IV.3 will be used for reference throughout the remainder of the report.

Slight damage to the cylinder was noted upon completion of the test. Post-shot investigations found all strain gages firmly attached to the cylinder at the locations specified in the instrumentation diagram. However, some water intrusion was noted under the protective coating of several of the strain gages. This intrusion may also have played a part in the strain gage failures. The results of the test were forwarded to the Naval Postgraduate School in reference 14.

3. NUMERICAL MODEL

This study was performed using two primary mesh densities. The low density, full model mesh (Figure IV.4) was used for rotation, shell type and quadrature sensitivity analyses. The high density quarter model was used to perform direct comparison to experimental results and examine end effects. The computational efficiency of the quarter model allowed a more refined mesh without a subsequent increase in computational time or random access memory storage capability. A sample quarter model was run and results checked against a



1. ALL MEASUREMENTS ARE IN INCHES
2. STRAIN GAGE POSITIONS
A1, A2
B1, B2, B3
C1, C2
3. HOOP AND AXIAL STRAIN MEASURED AT EACH POSITION.
4. POSITION B1 IS NEAREST THE CHARGE.

Figure IV.3. Undex test instrumentation diagram.

full model with the same mesh configuration to certify that the symmetry boundary conditions used to form the quarter model were valid. The refined mesh quarter model is shown in Figure IV.5.

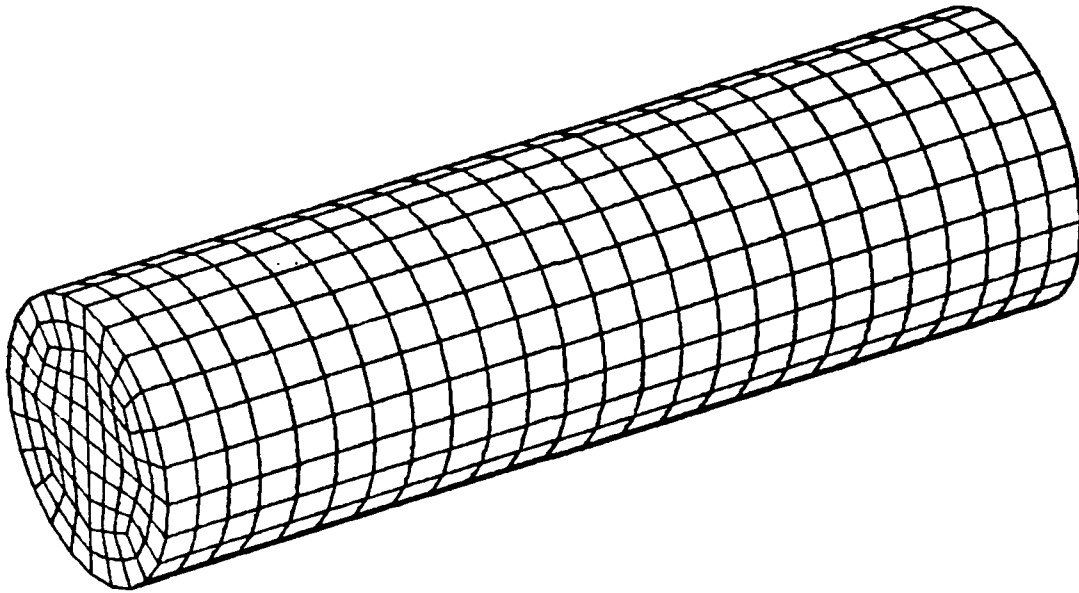


Figure IV.4. Low density, full model

In addition to the two models noted above, several additional quarter models with varying mesh density were run to verify mesh size independence of the quarter model results. It was found that the most critical locations for the mesh sensitivity check were the locations with the highest strain. The areas with the highest strain were located near each end on the side of the cylinder located nearest the explosive charge. Figure IV.6 shows the strain pattern on the surface

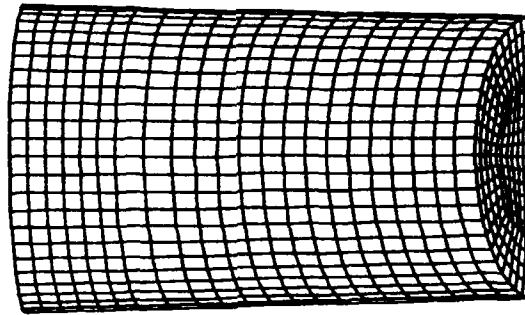


Figure IV.5. Refined mesh model.

on the surface of cylinder side nearest the charge. The high strain locations are symmetrically located 16.5 inches (0.42 m) from the axial midpoint of the cylinder. The other region of significant plastic strain was located on the surface of the reverse side of the cylinder at the axial midpoint. Figure IV.7 shows the effective plastic strain pattern for this location. The near side high strain regions cover a much smaller area than the reverse side region. That is, much higher strain gradients occurred on the near side compared to other locations on the cylinder. This condition plays a significant roll in mesh design and integration time increment selection.

time = .59796E-02
 fringes of eff. plastic strain
 min= 0.000E+00 in element 768
 max= 6.431E-03 in element 442

fringe levels

9.000E-04
1.800E-03
2.700E-03
3.600E-03
4.500E-03

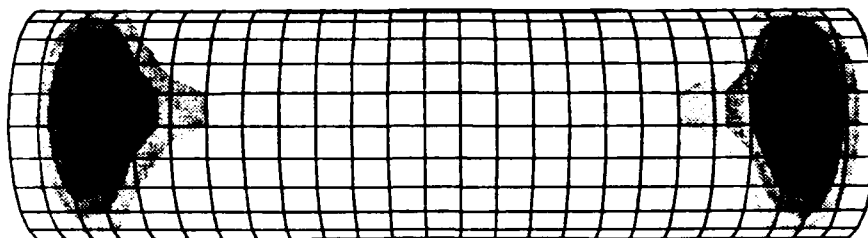


Figure IV.6. Effective plastic strain pattern on cylinder side nearest the explosive charge.

time = .59796E-02
 fringes of eff. plastic strain
 min= 0.000E+00 in element 768
 max= 6.431E-03 in element 442

fringe levels

9.000E-04
1.800E-03
2.700E-03
3.600E-03
4.500E-03



Figure IV.7. Effective plastic strain pattern on cylinder side most remote from the charge.

Figures IV.8 through IV.10 show the results of the mesh sensitivity test. It was found that strains in the axial direction were more sensitive to mesh density than hoop strain results. Figure IV.8 shows the strain at the surface of the cylinder at the point nearest the charge (location B1). This location has no permanent plastic strain. It can be seen that there is almost no significant difference between the results for the three mesh densities checked. Figure IV.9 shows strain results for the surface of the shell at the point most remote from the charge in the circumferential direction at the axial midplane (location B3). This location had the second highest strain of the positions checked. Although there is a slight difference between the three different mesh results, it is apparent that these differences are insignificant when compared to the overall plastic strain. Figure IV.10 shows the strain results for the locations that experienced the highest plastic strains (locations A1 and C1). The difference in the hoop direction is noticeable but small enough to be neglected. However, the results in the axial direction are significant with a 30 percent variance between the average plastic strains for the high density mesh and medium density mesh. Additional refinement was not possible due to random access memory limitations on the system used to perform the analysis. On the basis of the above results it was determined

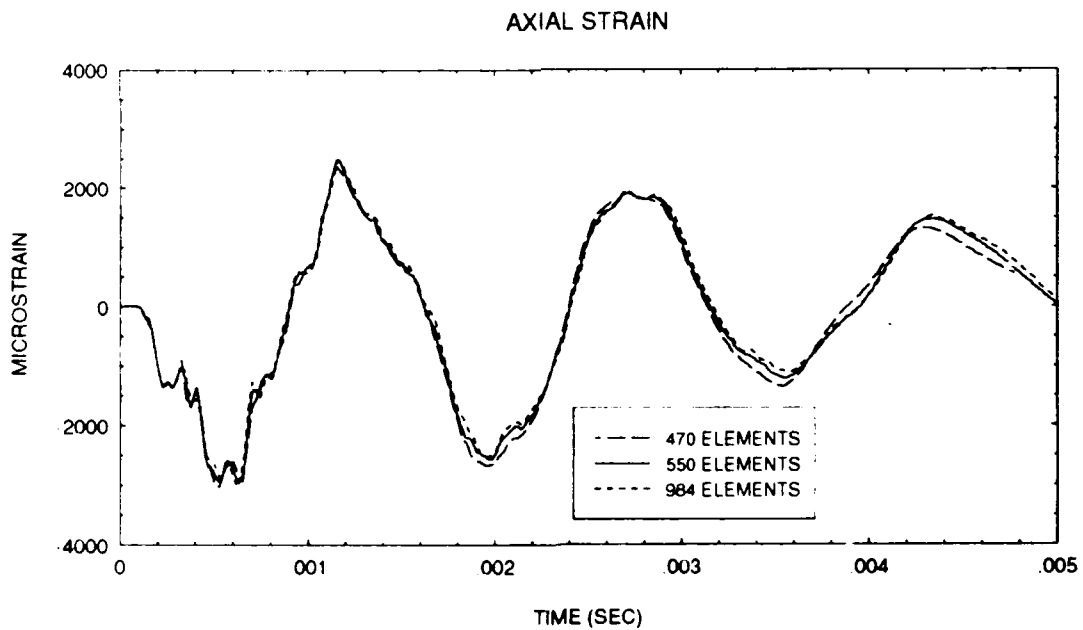
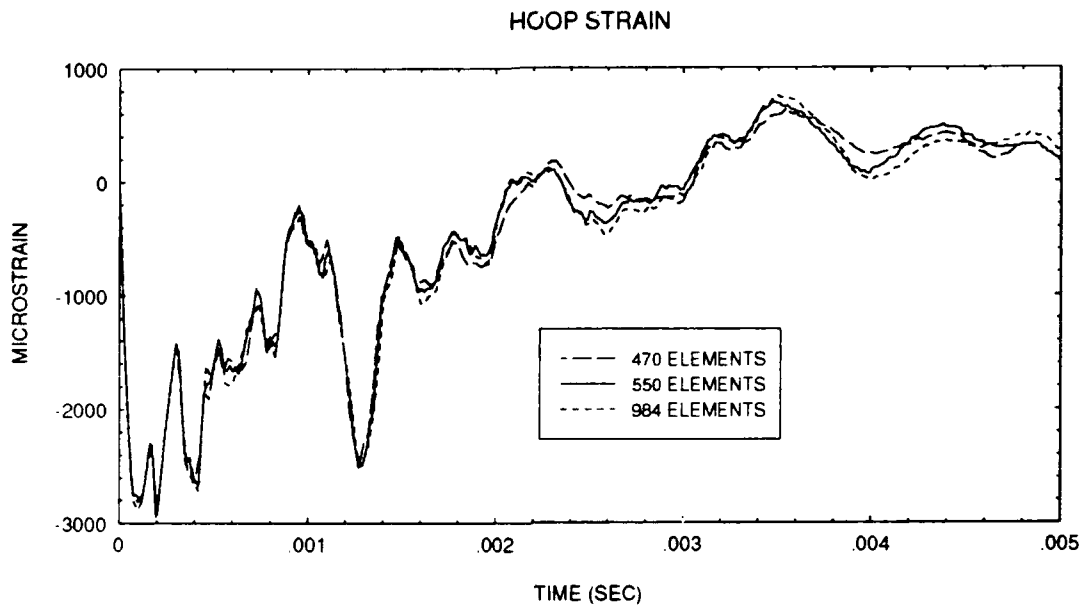


Figure IV.8. Mesh sensitivity comparison for surface of shell located nearest the explosive charge (location B1).

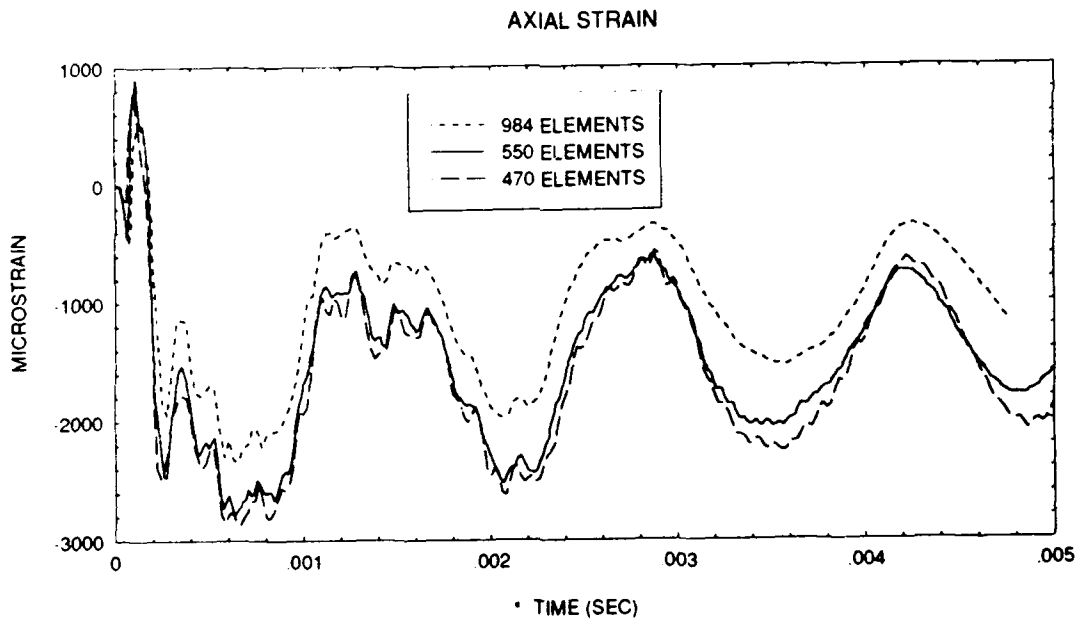
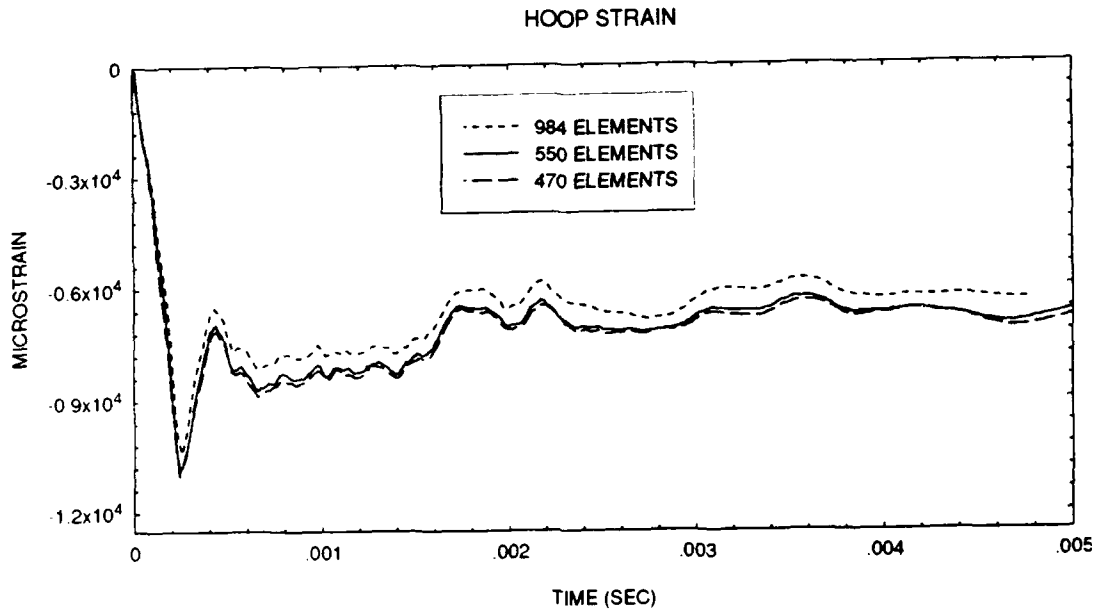


Figure IV.9. Mesh sensitivity comparison for position with largest plastic strain (locations A1 and C1).

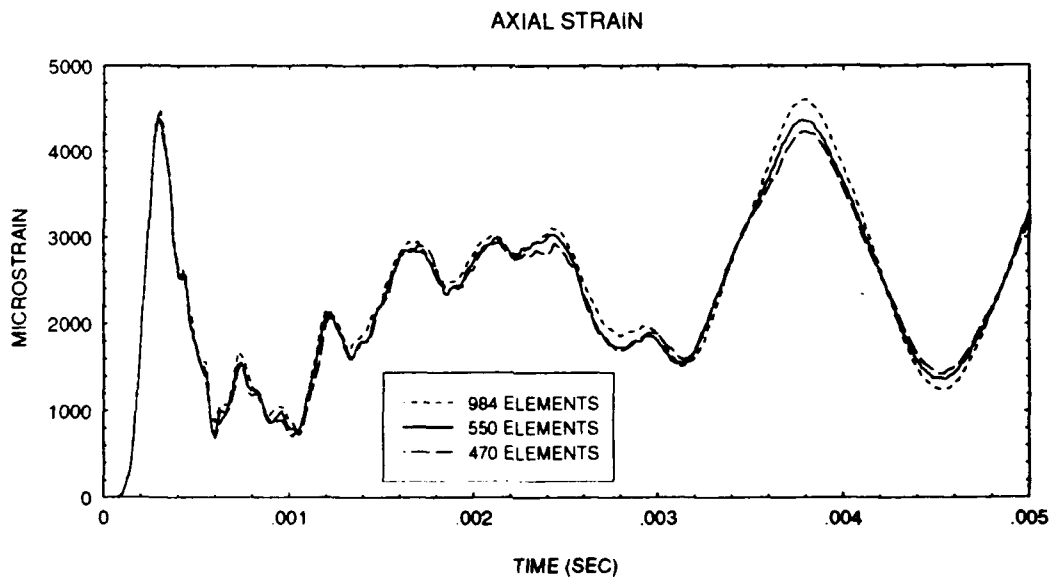
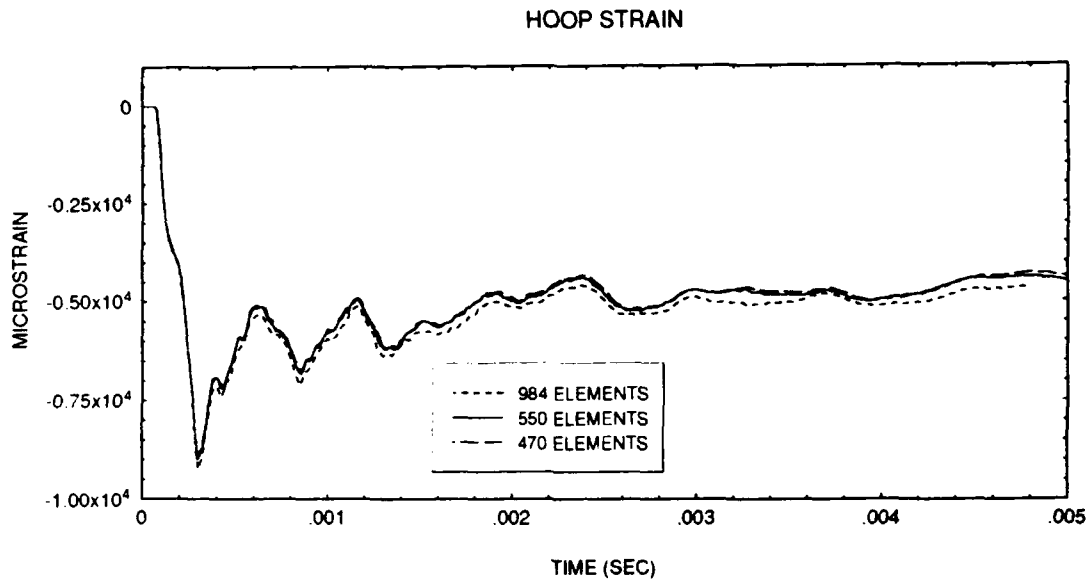


Figure IV.10. Mesh sensitivity comparison for point on cylinder most circumferentially remote from the charge (location B3).

that the medium mesh model was adequate for comparison of numerical to experimental results for all hoop strains and all axial strains except at the locations near the end on the side nearest the charge. The high density mesh was used for the axial strain comparison at the remaining locations. Care was taken to ensure that the mesh was as uniform as possible for both the full and the quarter mesh models to avoid problems with mesh reflection as noted earlier in this report.

Thin shell elements were used for both the shell and end plates. Since relatively small out of plane displacements were encountered in the test model, it was determined that the four node Belytschko/Lin/Tsay shell formulation, which is the default formulation for VEC/DYNA3D, was adequate for the analysis. A Hughes/Liu (Ref. 15) shell model and a eight node brick shell model were also run for comparison.

The Belytschko/Lin/Tsay shell was selected over the Hughes/Liu shell and 8 node brick shell formulation because of its higher relative computational efficiency.

The aluminum was treated as a kinematic/isotropic elastic/plastic material with no strain rate sensitivity. Research has shown that shock velocities much higher than the velocities encountered in the test are required to induce strain rate sensitivity in 6061-T6 aluminum.

The pressure input for the model was obtained from the free field pressure transducer time record of the underwater explosion test. The 17000 point trace was numerically condensed to 100 points and entered into the TIMINT pre-processor of USA using the VARLIN (variable linear) option. Figure IV.11 shows the pressure profile used for the analysis. Free surface effects were neglected and the speed of sound in water used for the test was 4800 ft/sec (1463 m/s) since the test was performed in fresh water at approximately 40 degrees Fahrenheit (4.5 degrees centigrade).

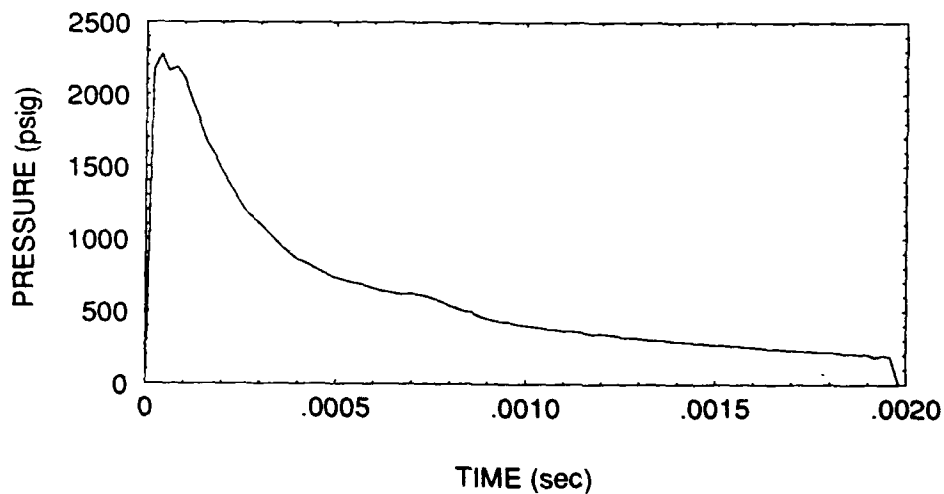


Figure IV.11. Undex pressure profile.

C. FAR FIELD STUDY RESULTS

1. EXPERIMENTAL TO NUMERICAL COMPARISON

As described earlier in the report, an underwater explosion test was conducted at the Dynamic Testing, Incorporated facility in Rustburg, Virginia. The test included a side-on attack of a cylinder with a stand off distance of 25 feet (7.62 m) using a 60 pound (27.3 Kg) HBX-1 charge. Fourteen strain gages were attached to the cylinder, of which eleven provided useable data. Four statements can be made about the results. First, the numerical results compared well with the experimental results qualitatively. That is, the numerical response had the same general shape as the experimental results and it predicted compression and tension correctly. There was one exception to the above statement at position B3 (Figure IV.20). The numerical model indicated a tensile axial strain at position B3 while the experimental data indicated a compressive strain. Physically, it can be observed that the shock wave is spherical and initially strikes the cylinder center. This places the cylinder in bending. Therefore, tensile strain is expected in the axial direction on the reverse side of the cylinder. It is believed that the poles on the axial strain gage at position B3 were reversed resulting in an error in sign of the data returned by the strain gage. As a result, the negative of the

experimental strain is plotted versus the numerical results in Figure IV.20 with satisfactory results.

Second, there were variations in magnitude between the numerical results and the experimental data. Further, magnitudes matched the experimental results more closely at the position nearest the charge and error increased as distance from the point nearest the charge increased in both the axial and circumferential directions. In addition, numerical and experimental results match more closely in areas with lower values of total strain. Finally, axial strains were affected more than hoop strains. Charge size factors were eliminated as a possible cause of the magnitude differential since the measured pressure profile was used to perform the post underwater explosion test numerical calculations. In addition, the possibility of the charge being located closer to the shell than the specified standoff distance was eliminated by comparing the actual shock wave travel time measured from the strain gage traces to the expected shock wave travel time calculated for the speed of sound in water for fresh water at 40 degrees Fahrenheit (4.4 degree centigrade). The results indicated less than two inches difference between the calculated and measured values for stand off distance.

Third, the frequency of oscillation of the numerical data was lower than the experimental data. The higher frequency oscillation in the physical model compared to the numerical model indicates that the experimental model is "stiffer" than the numerical model. This is an unexpected result, since numerical finite element solutions are normally expected to be stiffer than the physical model. In addition, the numerical results for axial strain tended to "ring" at all locations. The "ringing" is not a significant factor for hoop strains. It should also be noted that the "ringing" is heaviest at the front and back of the cylinder at the center. The causes of the "ringing" and the high relative stiffness of the physical model have not been determined and are a topic of additional study.

Finally, there is an unexpected asymmetry in the experimental results. The axial strain gage at position C1 (Figure IV.21) measured 50% lower than the axial strain gage at A1 (Figure IV.12) and the hoop strain gage at position C2 (Figure IV.22) measured nearly 50 percent higher than the hoop strain gage at position A2 (Figure IV.13). Failure of strain gages at positions A1, C1, and C2 prevented additional comparisons. The asymmetric results can result from two factors. The shell may have been rotated from the expected orientation by underwater currents or by forces placed on the

cylinder and rigging by the instrumentation cables or there could have been a failure in the bonding between the strain gage and the cylinder surface on one or more strain gages.

Figures IV.12 through IV.22 provide the results of the numerical to experimental data comparison.

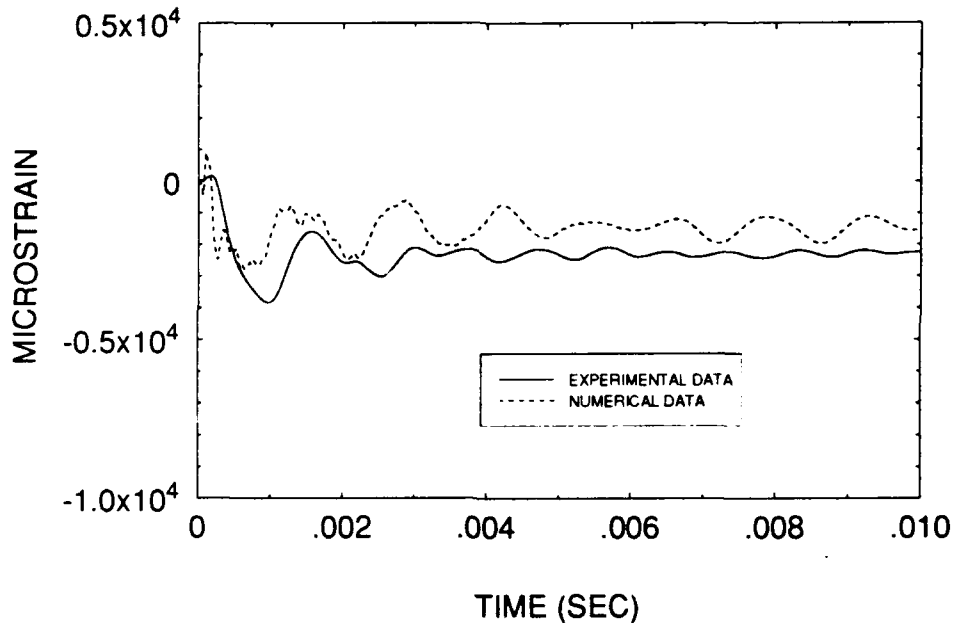


Figure IV.12. Experimental/numerical comparison for position A1 axial strain.

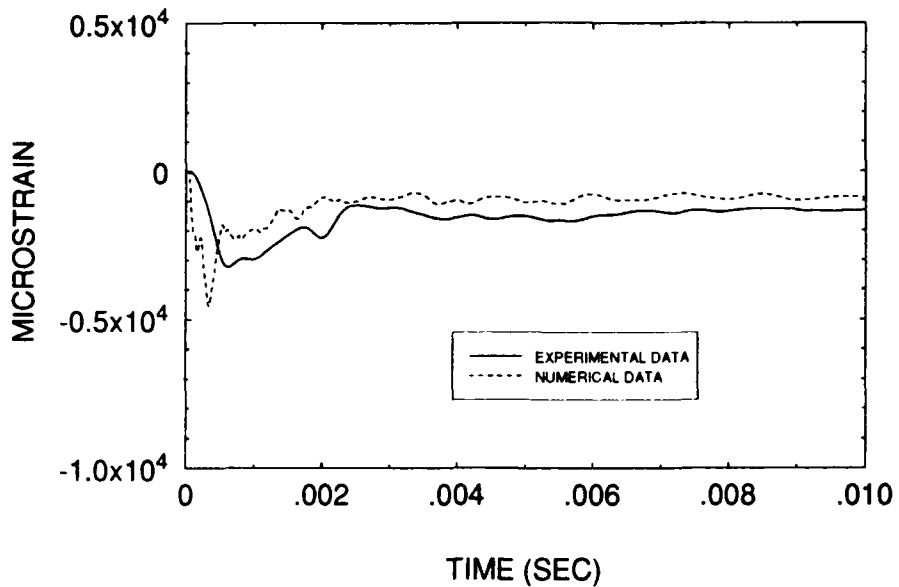


Figure IV.13. Experimental/numerical comparison for position A2 hoop strain.

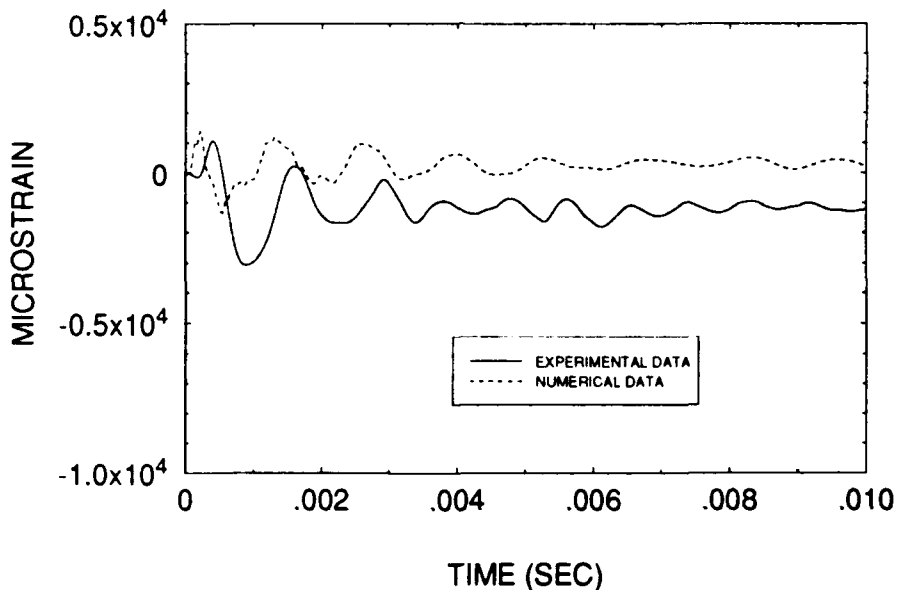


Figure IV.14. Experimental/numerical comparison for position A2 axial strain.

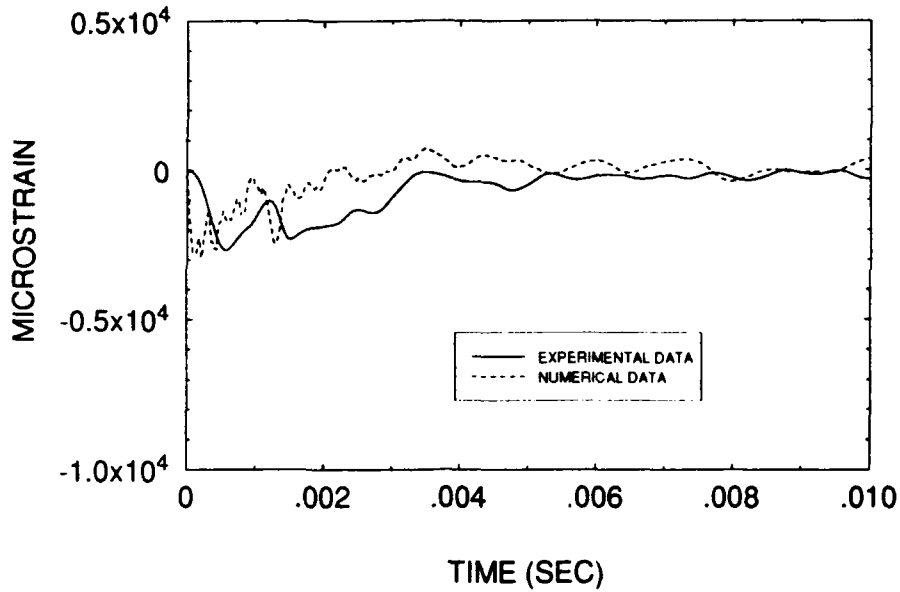


Figure IV.15. Experimental/numerical comparison for position B1 hoop strain.

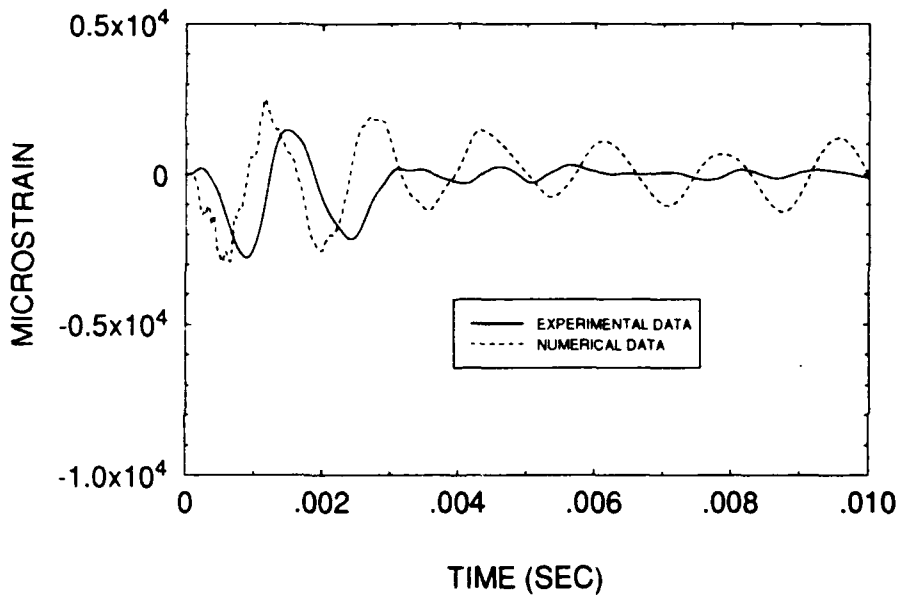


Figure IV.16. Experimental/numerical comparison for position B1 axial strain.

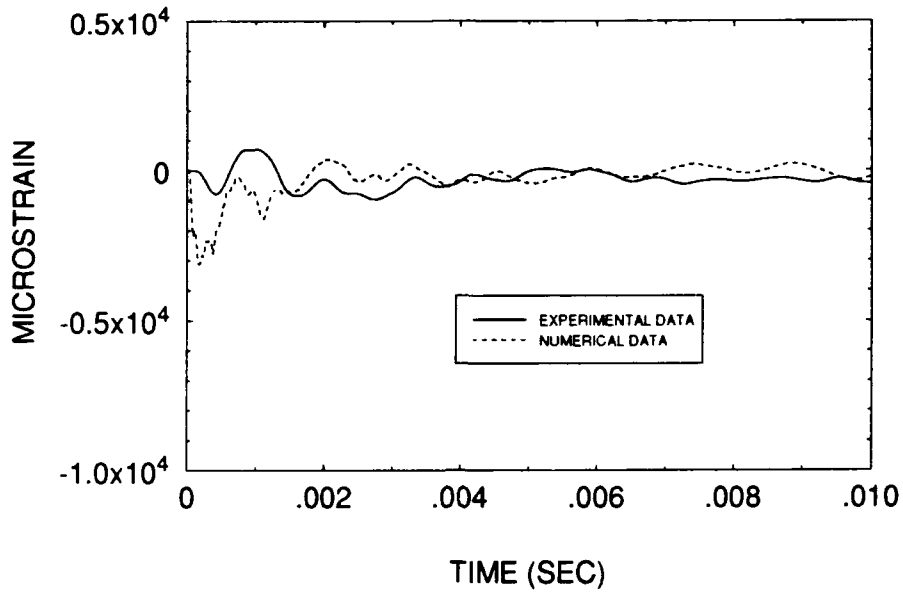


Figure IV.17. Experimental/numerical comparison for position B2 hoop strain.

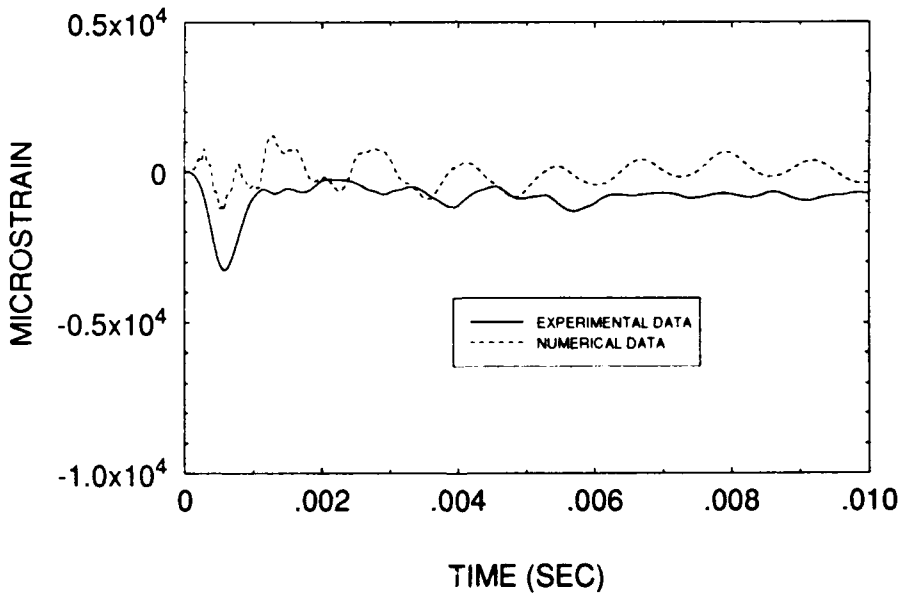


Figure IV.18. Experimental/numerical comparison for position B2 axial strain.

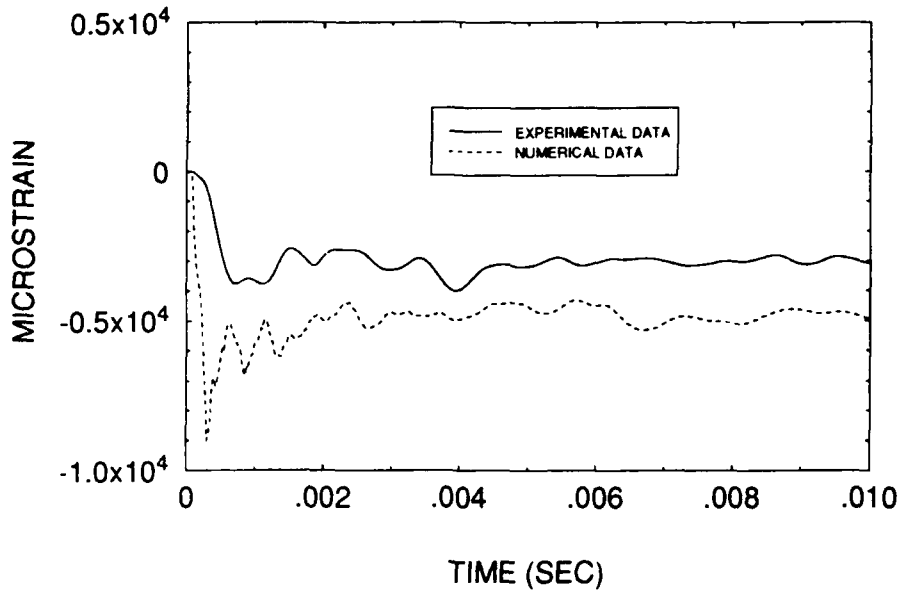


Figure IV.19. Experimental/numerical comparison for position B3 hoop strain.

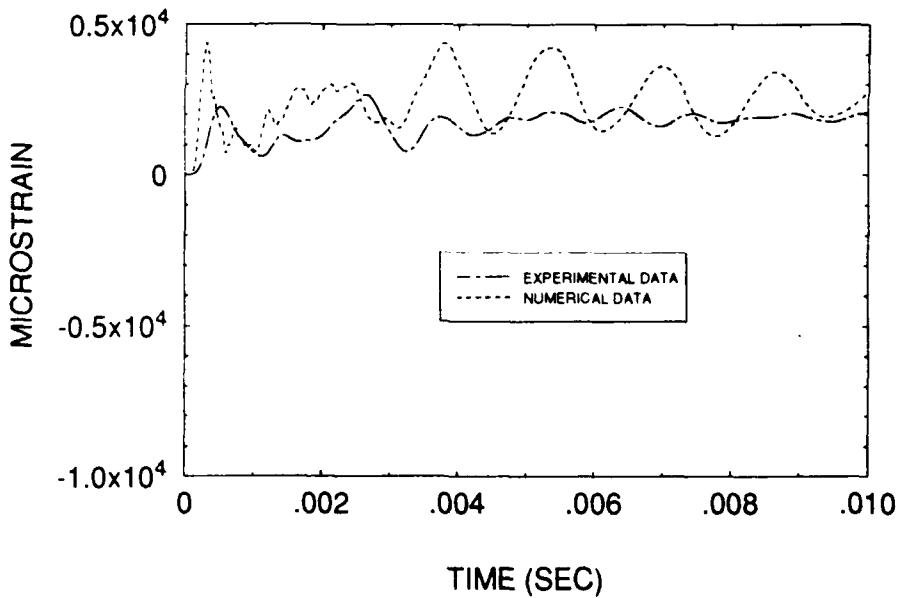


Figure IV.20. Experimental/numerical comparison for position B3 axial strain.

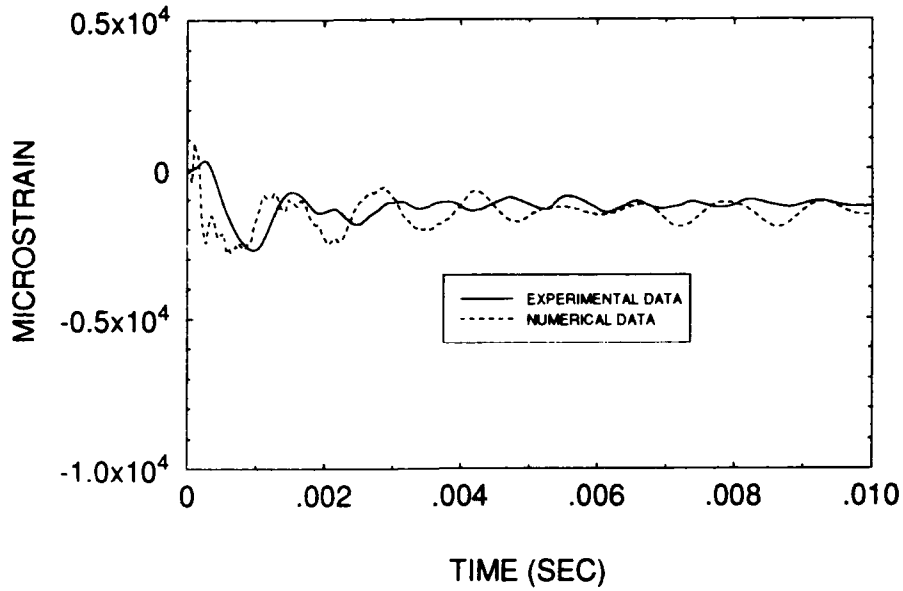


Figure IV.21. Experimental/numerical comparison for position C1 axial strain.

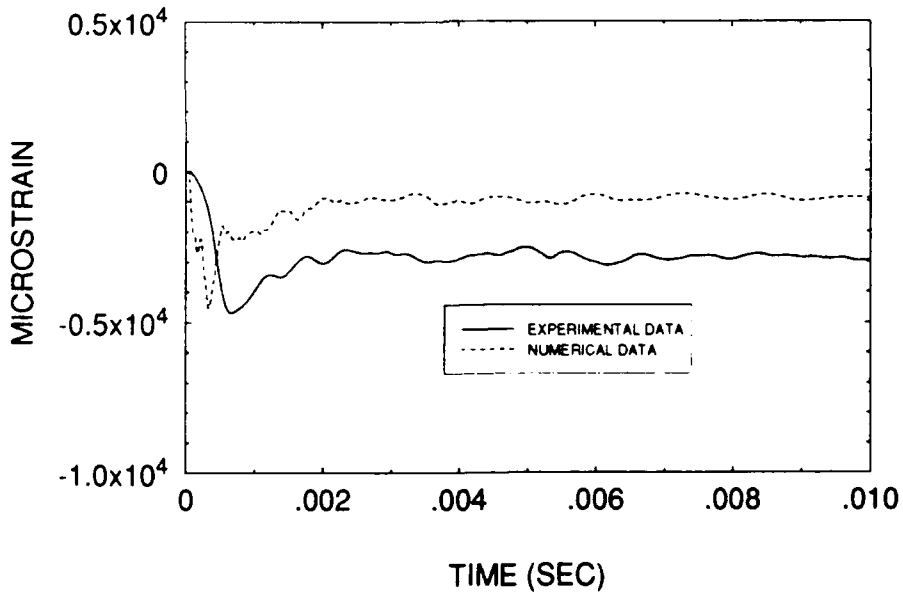


Figure IV.22. Experimental/numerical comparison for position C2 hoop strain.

2. SENSITIVITY ANALYSES

A series of sensitivity analyses were performed in an effort to explain the differences between the numerical and experimental results noted in the previous section. In addition, these analyses provided additional insight into the relative importance of various factors in the performance of underwater explosion tests and the associated calculations. Seven sensitivity analyses were performed. The first was the mesh sensitivity test. The results of this analysis have already been discussed. The other six analyses were, end effect, shell element formulation, integration time increment length, quadrature, rotational position and η value sensitivity checks. The results of these analyses are provided in the following subsections.

a. END EFFECT SENSITIVITY ANALYSIS

As previously noted, the most severe deformation occurred at locations near the end of the cylinder (positions A1 and C1). Two processes cause this phenomena. First, the relatively large mass of the end plates apply large inertial forces to the cylinder shell near the end plates. Second, the one inch thick end plates are very stiff and their lack of flexibility causes the weaker material of the shell near the end plates to deform in response to applied forces. A examination of the numerical and experimental data reveals

that these effects are concentrated near the end plates and result in large strain gradients. This means that elements on either side of a selected element near the end of the cylinder can have significantly different strain values. Accurate placement of strain gages within this region and careful mesh design along with adequately short time integration increments are critical in obtaining satisfactory results in a numerical to experimental data comparison. In addition, as stated earlier, the end plates are attached to the shell using a Tungsten Inert Gas process. This welding process results in high temperatures near the end of the cylinder. Since the aluminum for this model is at a peak hardened condition, this process could result in a change of the material properties near the end of the cylinder that can only be restored by performing the age hardening process again after the welding is complete. These factors can result in an uncertainty in the expected strain compared to what might occur under ideal circumstances.

The mesh sensitivity results clearly display the importance of mesh design within this region. However, even with proper design, the large gradients can result in significant differences between the predicted and actual strains since the strain computed for the element is an average of the strain over the entire element vice a strain at

a specific point. The best possible results would be obtained in these regions with large gradients if the mesh could be refined such that the size of the elements is the same size as the gage length of the strain gage. However, this would result in a prohibitively large number of elements and a subsequent increase in problem solution times. These problems can be overcome by placing strain gages in areas that are expected to have consistently increasing or decreasing strains and then ensuring that the mesh is designed so that the strain gage location is at the center of the element. If possible, large gradient regions should be avoided. If strain gages must be placed in a high gradient region, then the strain gages should be placed to one side or the other of the minimum or maximum strain location. Placement at the minimum or maximum point will result in an error since the average for the element will lie above a minimum or below a maximum if the element is not the same size as the gage length of the strain gage.

In this study, the strain gages located at A1 and C1 were located at the point of highest compressive strain. Therefore, a study was performed to determine the relative importance of the noted location factors. Figures IV.23 through IV.27 show the results of this study. Strains of two additional elements nearer the end were compared to the

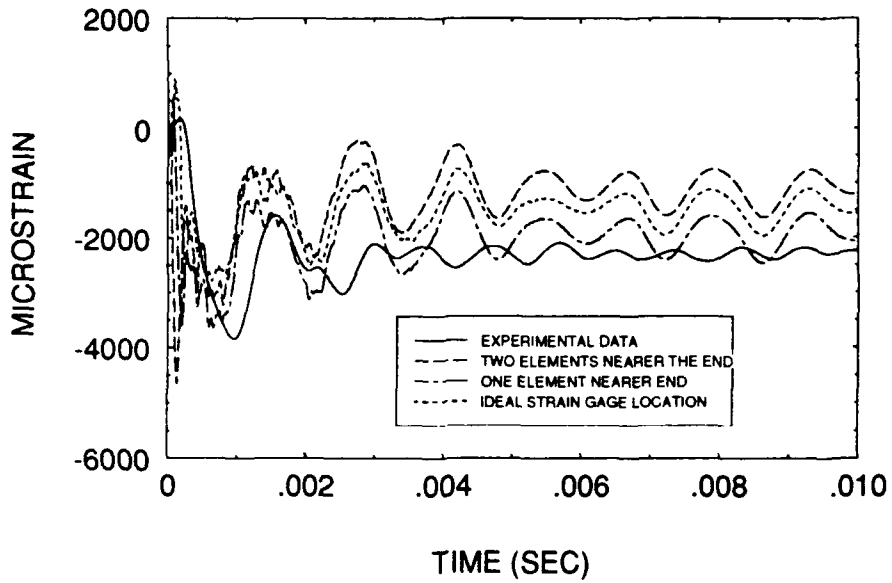


Figure IV.23. End effect sensitivity results.
(A1 axial)

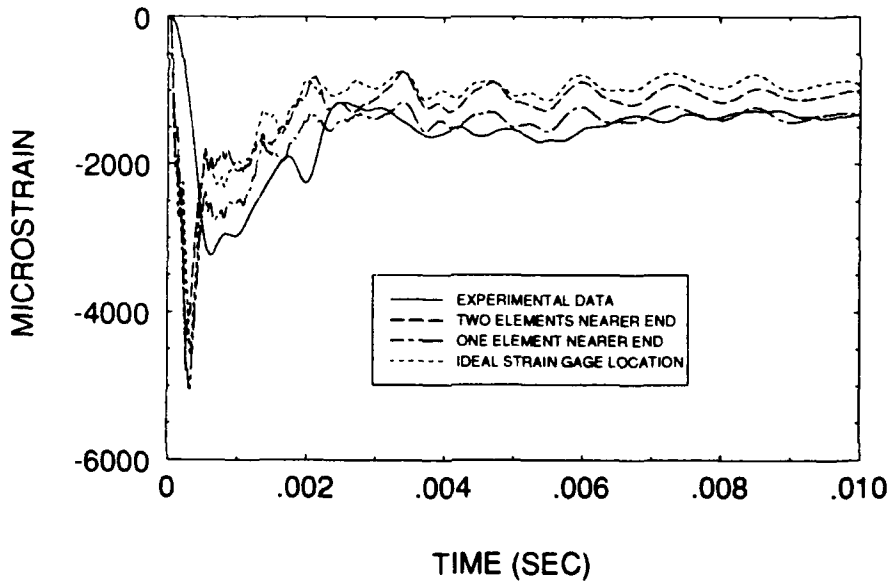
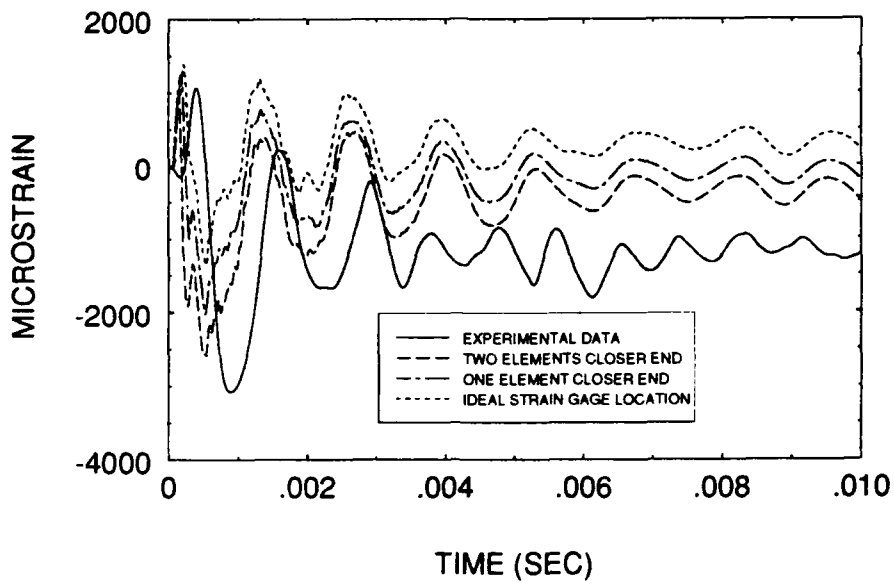
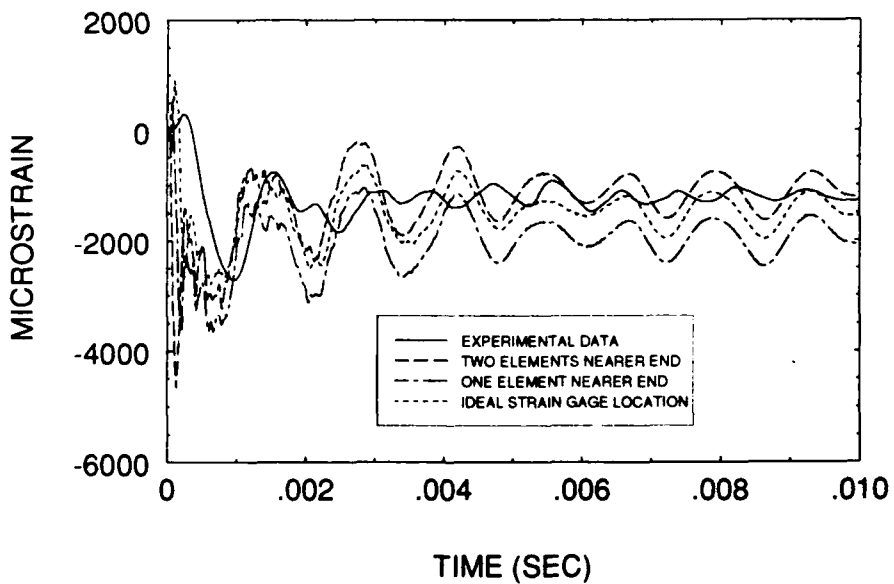


Figure IV.24. End effect sensitivity results.
(A2 Hoop)



**Figure IV.25. End effect sensitivity results.
(A2 Axial)**



**Figure IV.26. End effect sensitivity results.
(C1 Axial)**

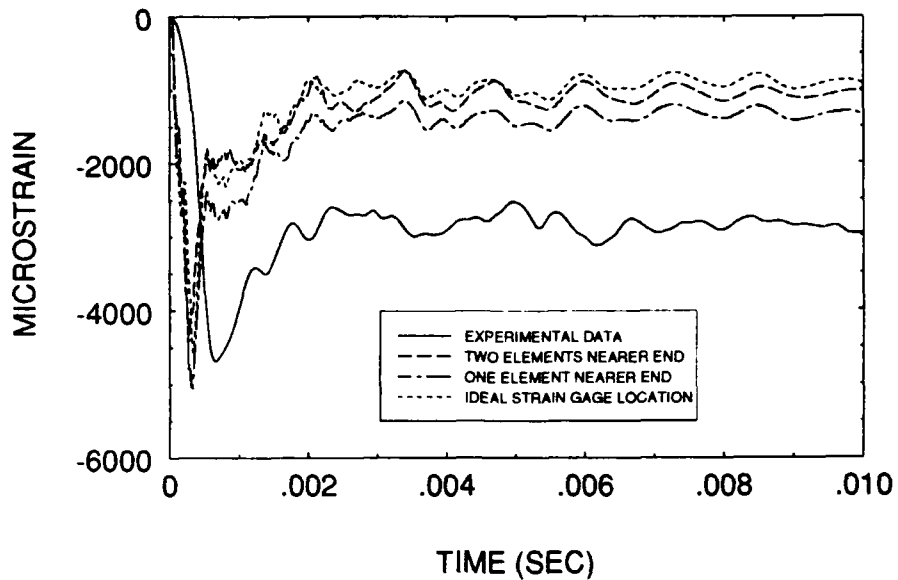


**Figure IV.27. End effect sensitivity results.
(C2 Hoop)**

measured strain and the actual strain gage location. Elements nearer the end plate were selected since the welding effects described in the previous paragraph would tend to move the high strain location nearer to the end plate by weakening the material near the end plate. Only the positions with useable experimental results are shown. In four of the five cases (positions A1 axial, A2 hoop, C1 axial and C2 hoop), if asymmetry effects are taken into account, the element one nearer to the end from the actual strain location provides a better estimate of the actual strain measured during the underwater explosion test. At the fifth location (A2 axial), the second element closer to the end provides the best

results. These results require additional study to separate and quantify the effect of the phenomena.

**b. SHELL FORMULATION, QUADRATURE RULE AND INTEGRATION
TIME INCREMENT SENSITIVITY ANALYSES**

In addition to the above end effects, there was some concern that the mid plane reference for the thin shell element would result in a greater flexible length than the actual physical model. This concern was based on the fact that the mass and stiffness of the end plates is concentrated into a planar surface co-located with the mid plane of the end plate in the thin shell analysis. This resulted in the shell portion of the structure being one inch longer in the numerical model than the physical model. This problem could have been avoided by using the Hughes/Liu formulation and shifting the reference plane to the inner surface of the shell. To resolve this issue a study was conducted to compare the performance of different types of thin and thick shell element formulations.

Results from the Belytschko/Tsay/Lin shell formulation were compared to results from the same model using the Hughes/Liu shell formulation. As stated earlier, the Belytschko/Lin/Tsay shell has the advantages of increased computational efficiency and a high degree of stability with large deformations at the expense of reduced accuracy at high

levels of plastic strain. The major difference between the two formulation stems from the fact that the element normal direction is updated periodically in the Hughes/Liu formulation. The Belytschko/Lin/Tsay formulation assumes negligible out of plane deformations, and therefore, does not update the shell normal. As a result, the inaccuracy of the Belytschko/Lin/Tsay formulation will increase as shell deformation becomes significant.

The models used to compare the two formulations were identical in all aspects with the exception of the shell formulation. The center line plane was used for the reference on both models. The results confirmed that the strain levels encountered in this underwater explosion test were small enough to support use of the Belytschko/Lin/Tsay formulation. However, it was apparent that differences did occur for positions with significant plastic strain in the axial direction (Positions A1, A2, B3, C1, and C2). Although the differences in these cases were not significant enough to require use of the Hughes/Liu formulation, it is also noted that higher strain may result in larger differences. Therefore the Belytschko/Lin/Tsay formulation should not be used in cases where significant denting occurs unless stability problems occur while using the Hughes/Liu formulation.

As stated earlier, the presence of high strain gradients near the end plates causes small changes in end condition or distance to be significant. When it became apparent that end effects would be important in the results an investigation was performed to determine if an eight node brick shell formulation would provide more accurate results near the end of the cylinder. The thin shell formulation results as well as the experimental results were compared to results from a model computed using eight node brick shell elements. All three formulations are compared to experimental results in Figures IV.28 through IV.38. The following information can be gleaned from the plotted results. First, it is apparent that the greatest differences occur near the positions with the highest strains. At the same time, it can be noted that there is virtually no difference at the locations with no permanent strain. Second, as shown in Figures IV.28, IV.29, IV.35, IV.36 and IV.38, it is clear that there is a significant difference between the eight node brick shell results and the Belytschko/Lin/Tsay results at the locations with high levels of permanent plastic strain. However, contrary to the expected results, the eight node brick shell results move further from the expected values than the other formulations. It is also noted that the Hughes/Liu formulation lies between the eight node brick shell and the

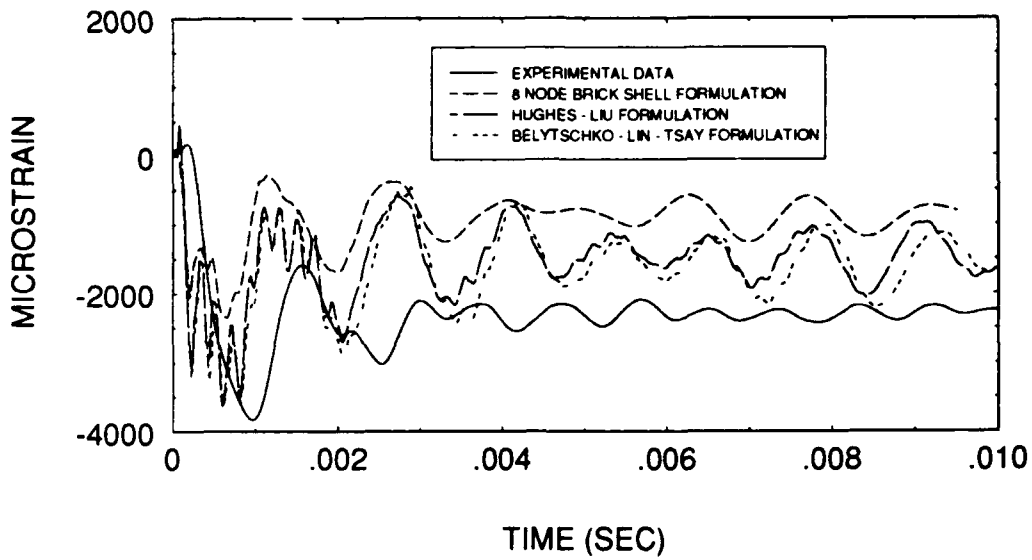


Figure IV.28. Shell formulation sensitivity results. (A1 Axial)

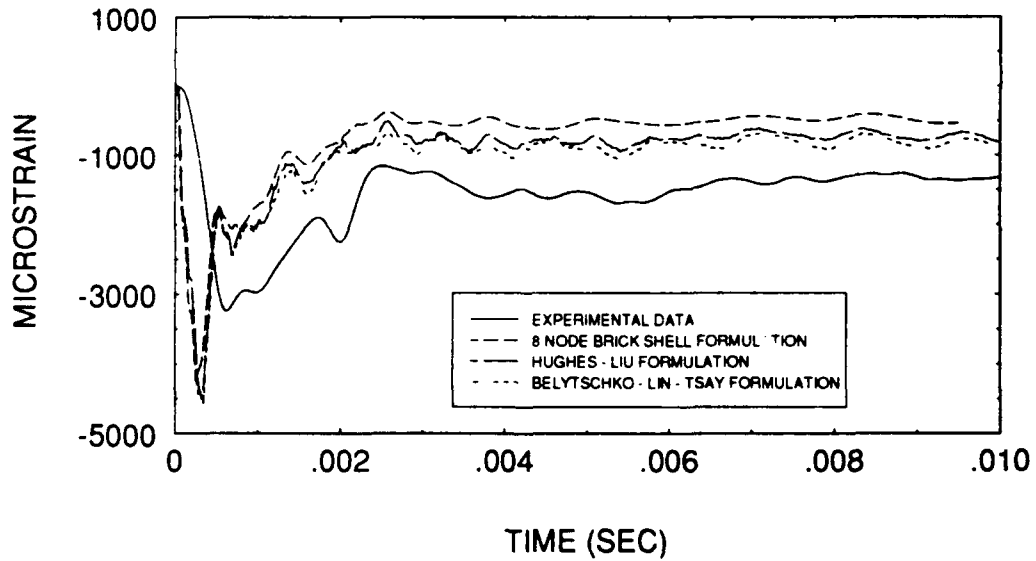


Figure IV.29. Shell formulation sensitivity results. (A2 Hoop)

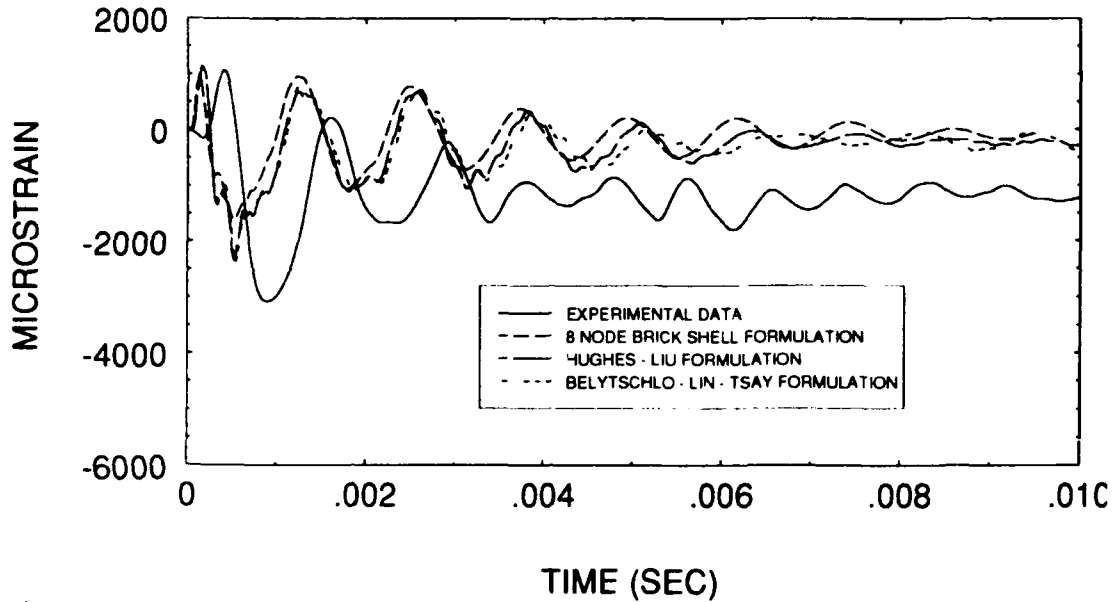


Figure IV.30. Shell formulation sensitivity results (A2 Axial)

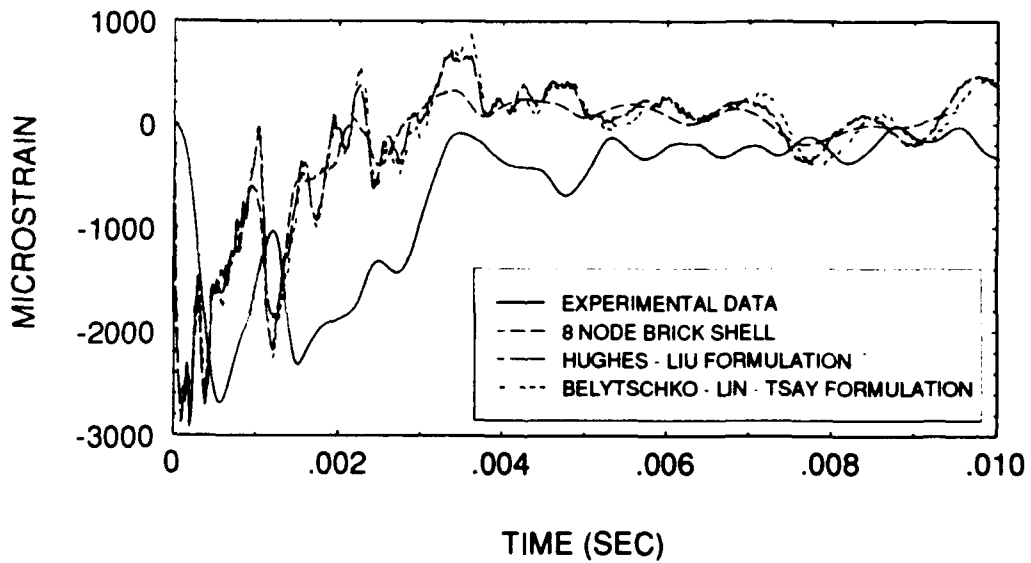


Figure IV.31. Shell formulation sensitivity results. (B1 Hoop)

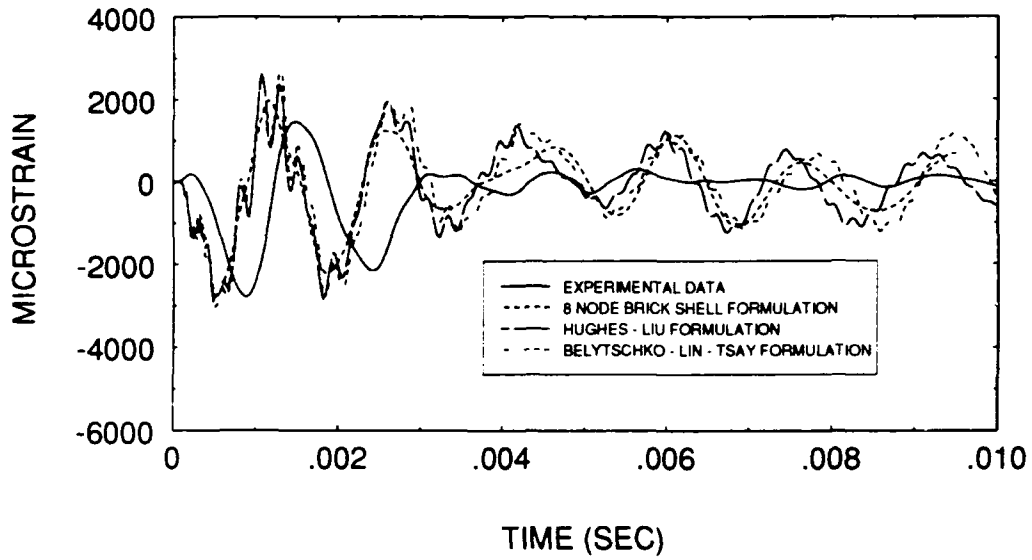


Figure IV.32. Shell formulation sensitivity results.
(B1 Axial)

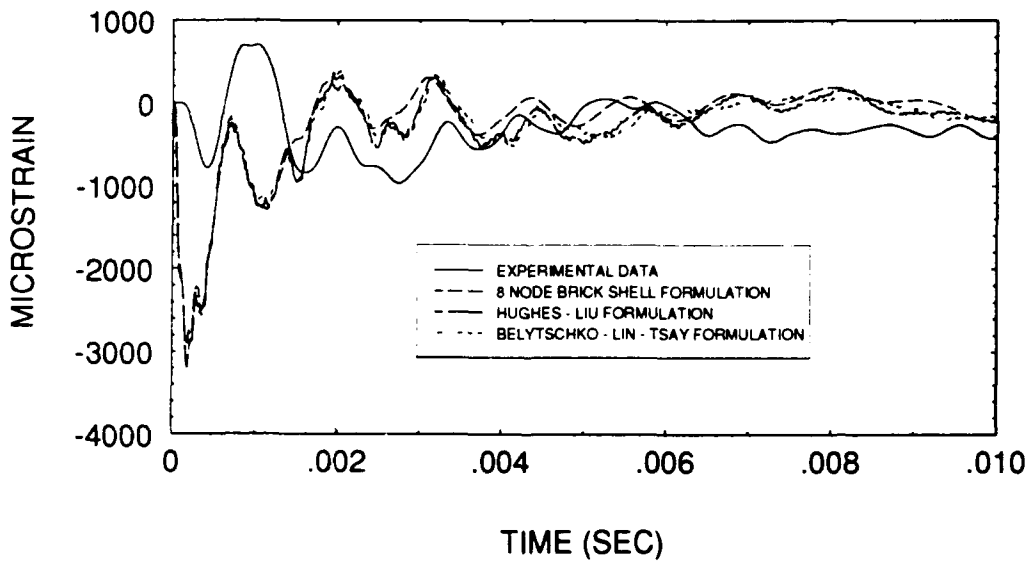
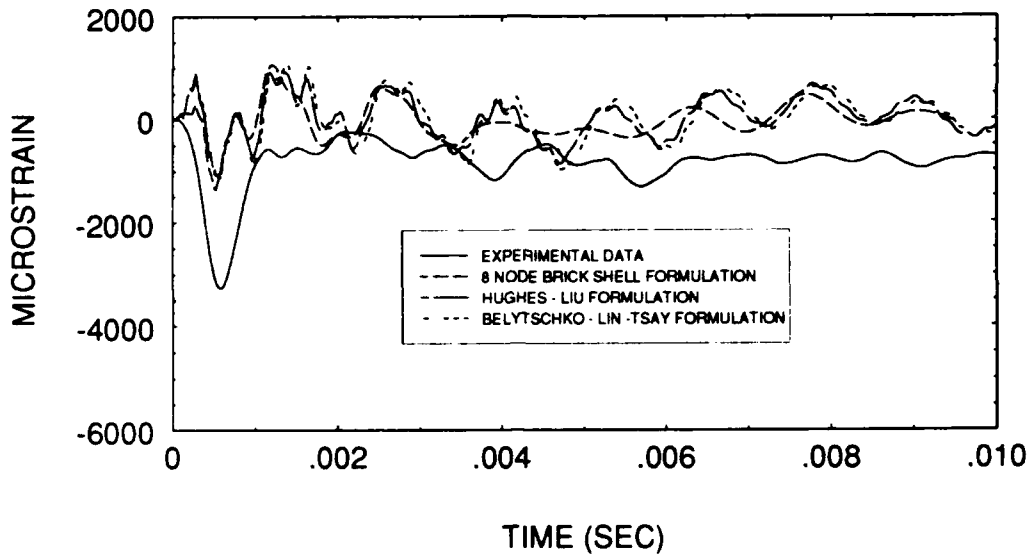
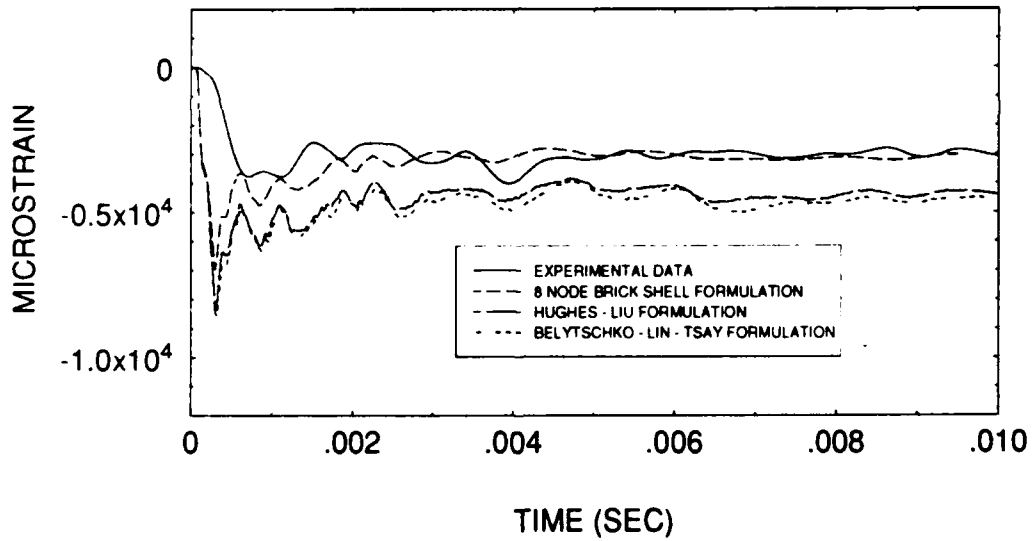


Figure IV.33. Shell formulation sensitivity results.
(B2 Hoop)



**Figure IV.34. Shell formulation sensitivity results.
(B2 Axial)**



**Figure IV.35. Shell formulation sensitivity results.
(B3 Hoop)**

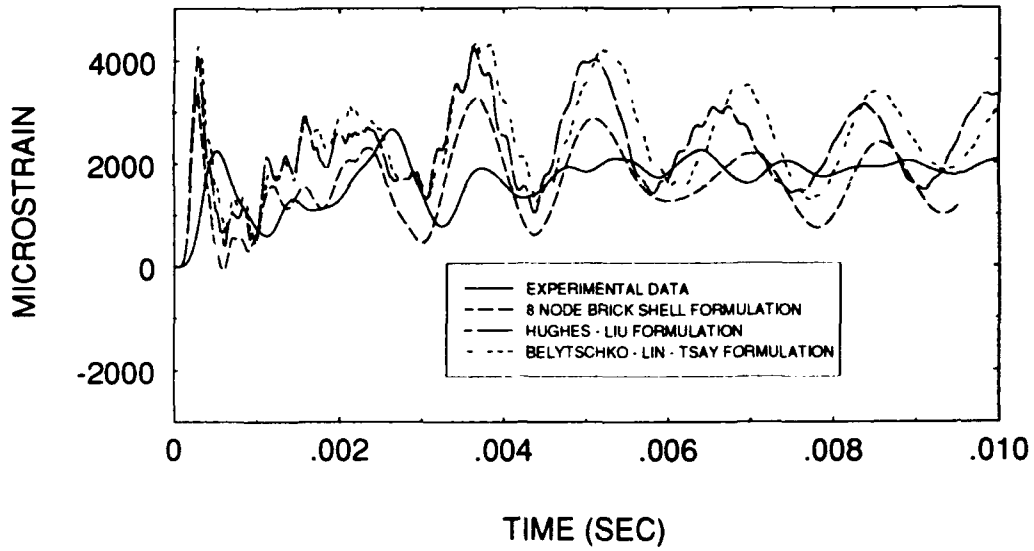


Figure IV.36. Shell formulation sensitivity results.
(B3 Axial)

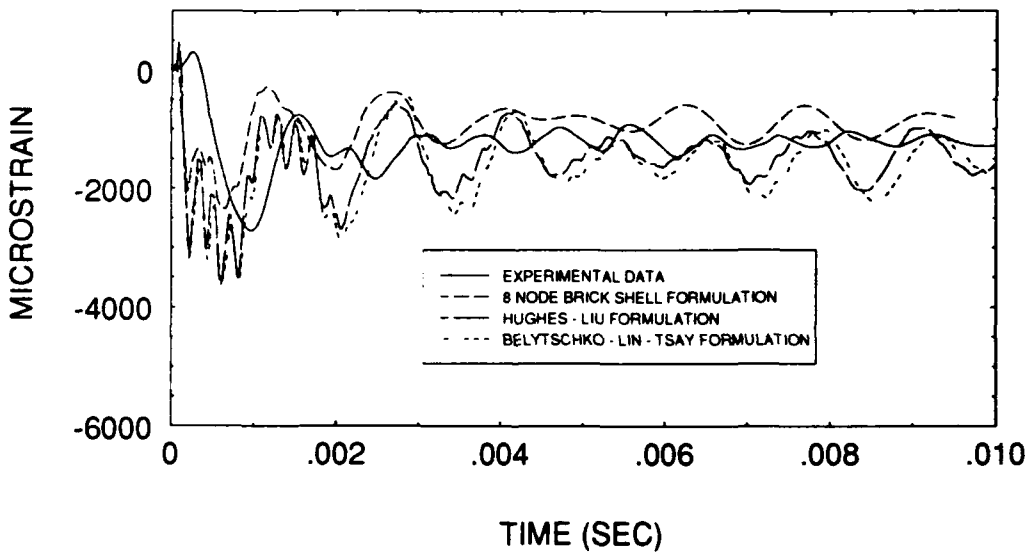
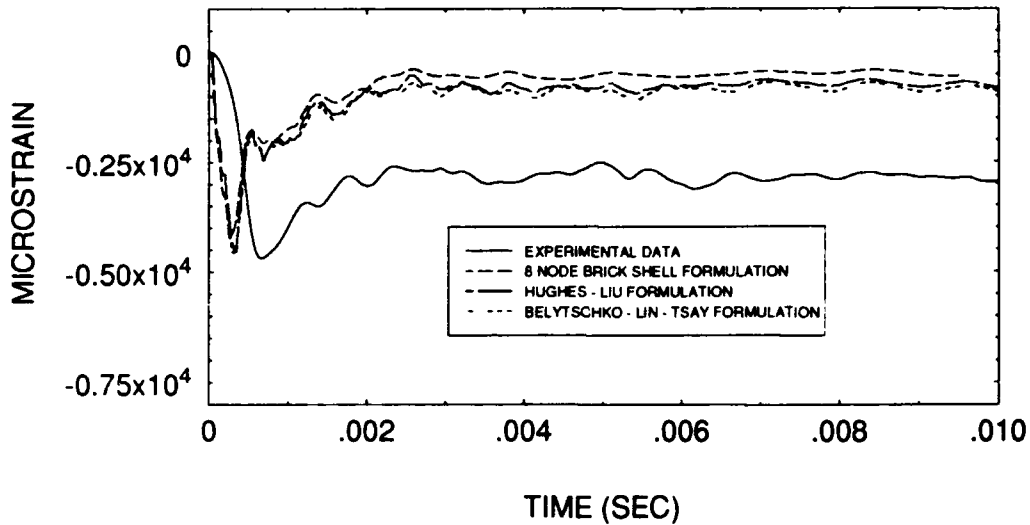


Figure IV.37. Shell formulation sensitivity results.
(C1 Axial)



**Figure IV.38. Shell formulation sensitivity results.
(C2 Hoop)**

Belytschko/Lin/Tsay formulation.

Additional research was performed to determine the cause of the disparities. The study revealed that the eight node brick shell is sensitive to integration time increment and will move marginally closer to the thin shell results if time integration is cut in half. However, the overall shift is only about 10 percent of the total difference. Quadrature rule (number of points used in the Gauss quadrature numerical integration scheme) proved to be a more significant effect. Use of five point quadrature moved the three results closer together while having the most profound effect on the Belytschko/Lin/Tsay formulation. Again, the affect of

quadrature rule affected the thick shell results only marginally. Figure IV.39 shows the combined results for the location with greatest plastic deformation.

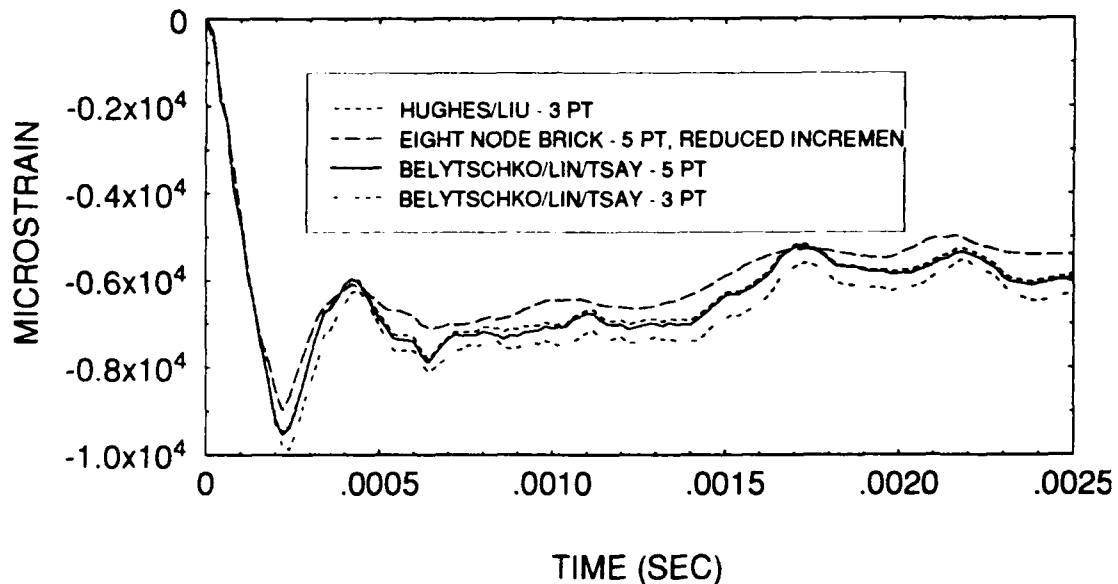


Figure IV.39. Effect of changing quadrature rule and time integration increment at location of highest strain (A1 and C1 hoop).

In summary, all three formulations appear to be satisfactory as long as care is used in designing the mesh and selecting the integration time and quadrature integration rule parameters. Specifically, when using Belytschko/Lin/Tsay formulations in areas with relatively high strain, the number

of quadrature points should be increased until stable results are achieved. When using eight node brick shell elements, integration time increment must be selected with care but number of quadrature points seems to be less critical. The Hughes/Liu formulation appeared to be relatively insensitive to both quadrature rule and integration time increment.

Reference 16 provides some useful thumbrules for selection of time increments. The following criteria are recommended.

$$\Delta t \approx 0.9 \frac{V}{(A_b c)} \text{ for brick shells}$$

$$\Delta t \approx 0.9 \frac{A_s}{Dc} \text{ for thin shells}$$

V - element volume

Δt - time increment

A_s - maximum surface area

D - maximum diagonal

c - speed of sound in the material

A_b - maximum area of any surface

The above criteria were found to be adequate except for the highest strain areas where the thick shell element rule did not provide stable solutions. In areas such as A1 and C1, a

value of the integration time increment half of the above recommendation proved to be satisfactory for the eight node brick shell.

C. ROTATION SENSITIVITY ANALYSIS

A sensitivity analysis was performed to determine the effect of an in plane rotation away from the expected symmetric orientation in an effort to explain the cause of the asymmetric results of the underwater explosion test. It was hypothesized that an unplanned rotation greater than ten degrees would have been detected by the personnel performing the test. Four different models were run within this range representing rotations of 0.0, 2.5, 5.0 and 10.0 degrees. The results are shown along with experimental results where available in Figures IV.40 through IV.53. The following observations are made concerning the results. First, the most dramatic affects are on the reverse side of the cylinder at position B3 (Figures IV.48 and IV.49). The results show that the differential between the numerical and experimental results at position B3 can be explained by a six to eight degree rotation from the symmetric configuration. Rotational effects at locations B1 and B2 on the centerline (Figures IV.44 through IV.47) are insignificant. Hoop strain at position C2 (Figure IV.52) is approximately 60 percent

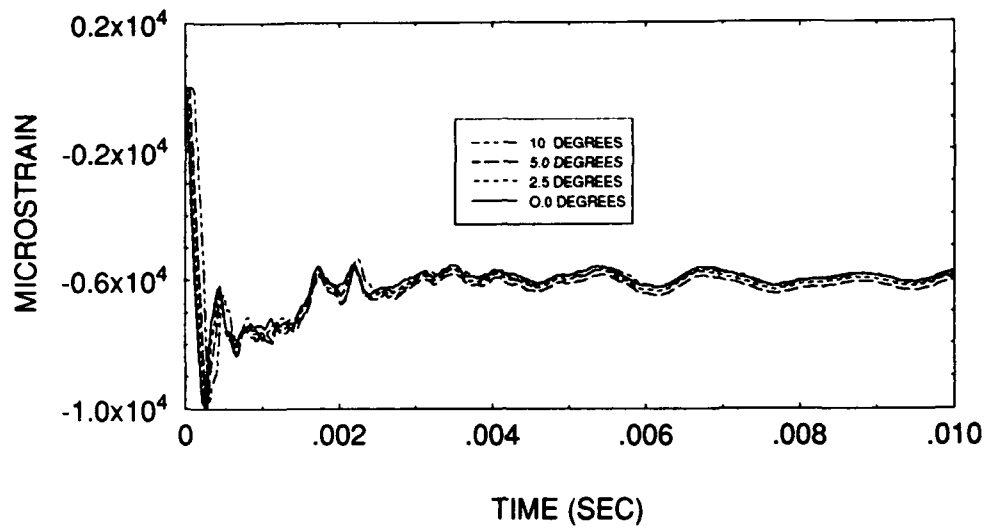


Figure IV.40. Rotation sensitivity results.
(A1 Hoop)

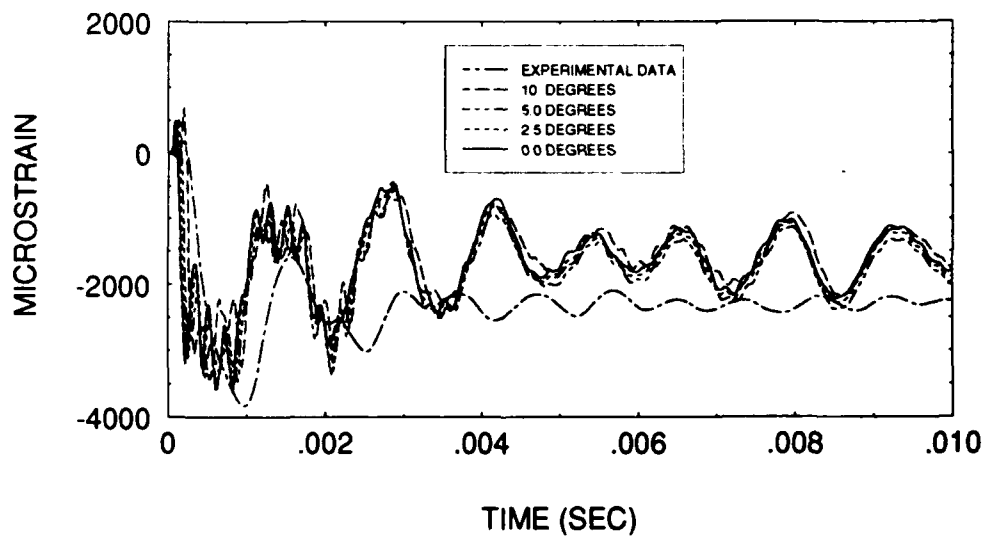


Figure IV.41. Rotation sensitivity results.
(A1 Axial)

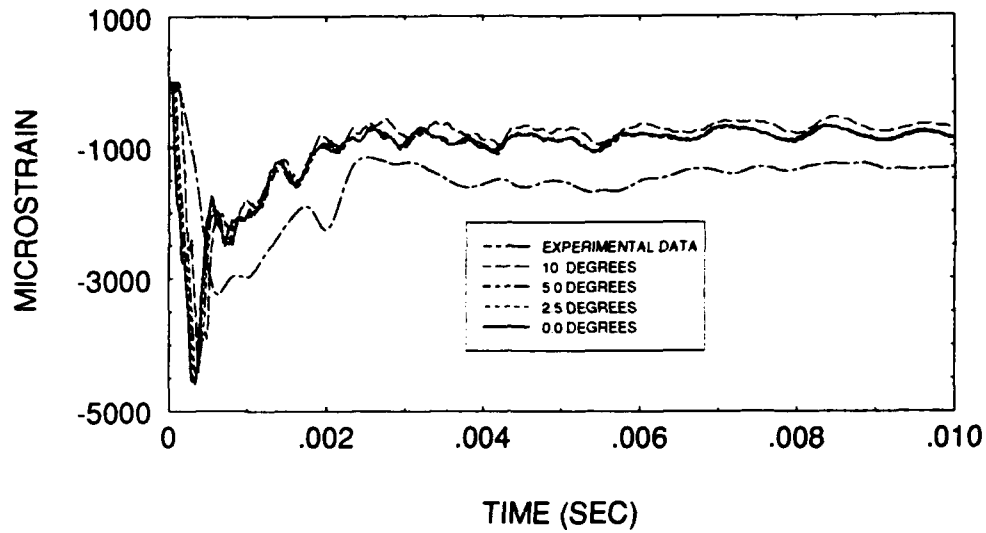


Figure IV.42. Rotation sensitivity results.
(A2 Hoop)

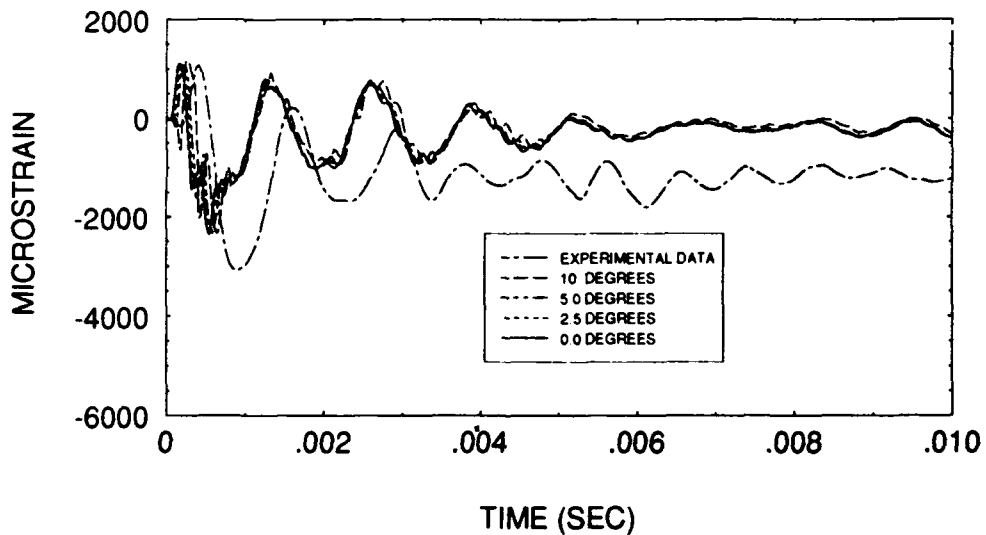


Figure IV.43. Rotation sensitivity results.
(A2 Axial)

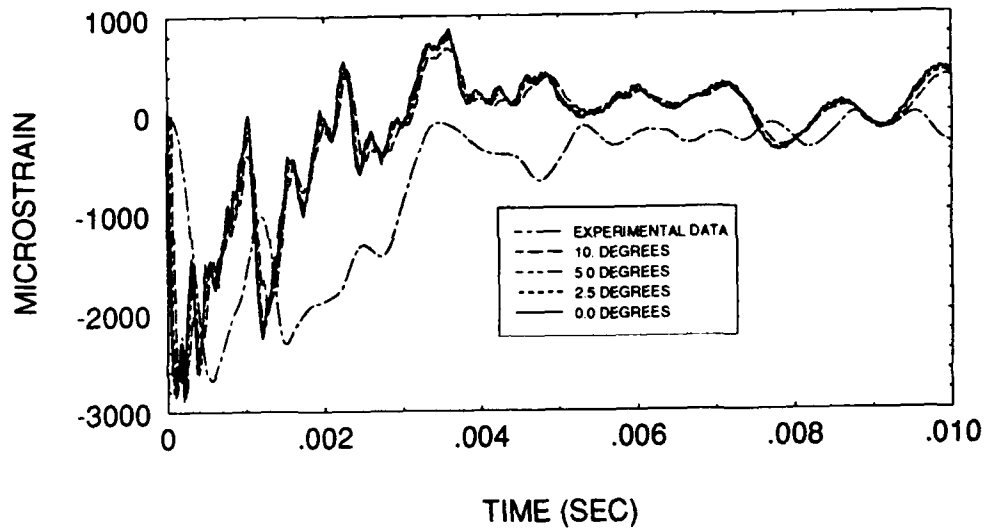


Figure IV.44. Rotation sensitivity results.
(B1 Hoop)

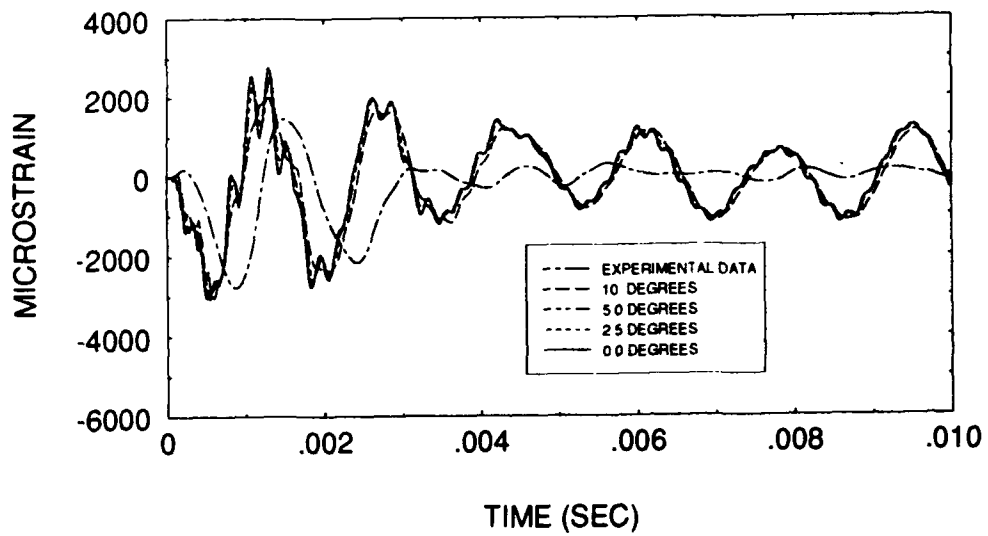
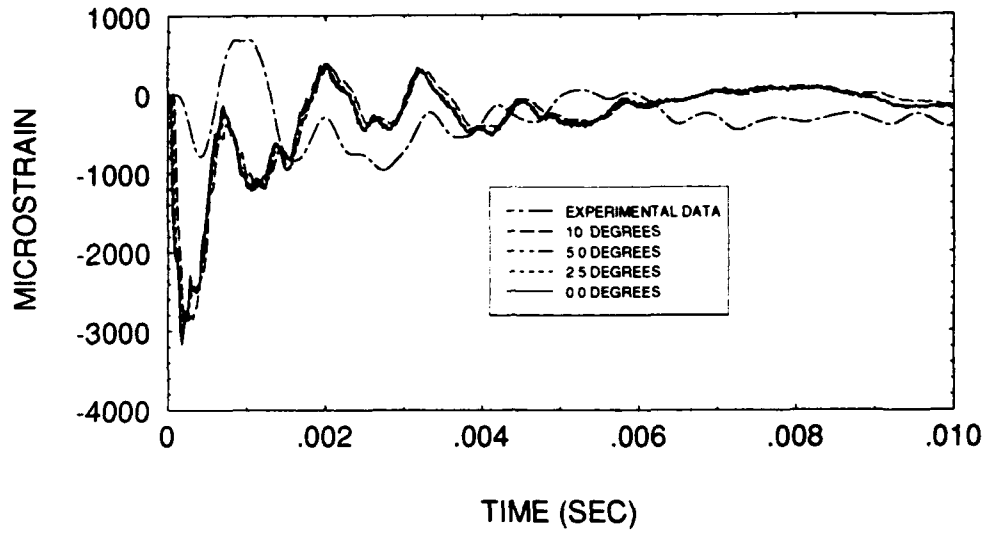
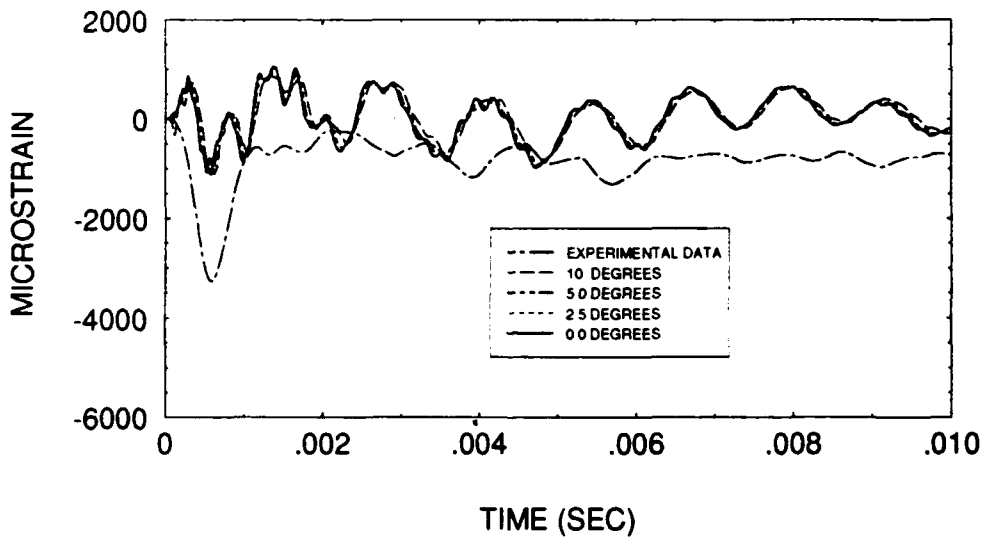


Figure IV.45. Rotation sensitivity results.
(B1 Axial)



**Figure IV.46. Rotation sensitivity results.
(B2 Hoop)**



**Figure IV.47. Rotation sensitivity results.
(B2 Axial)**

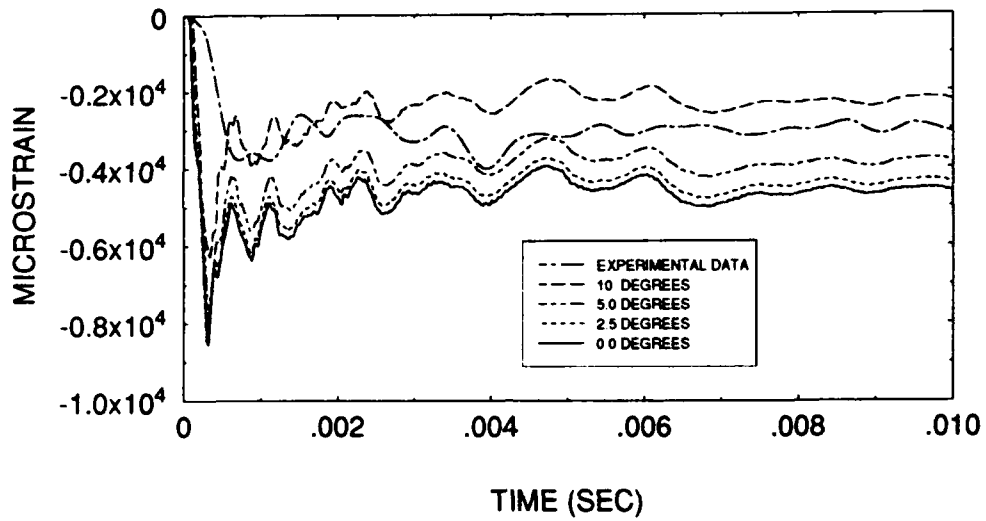


Figure IV.48. Rotation sensitivity results.
(B3 Hoop)

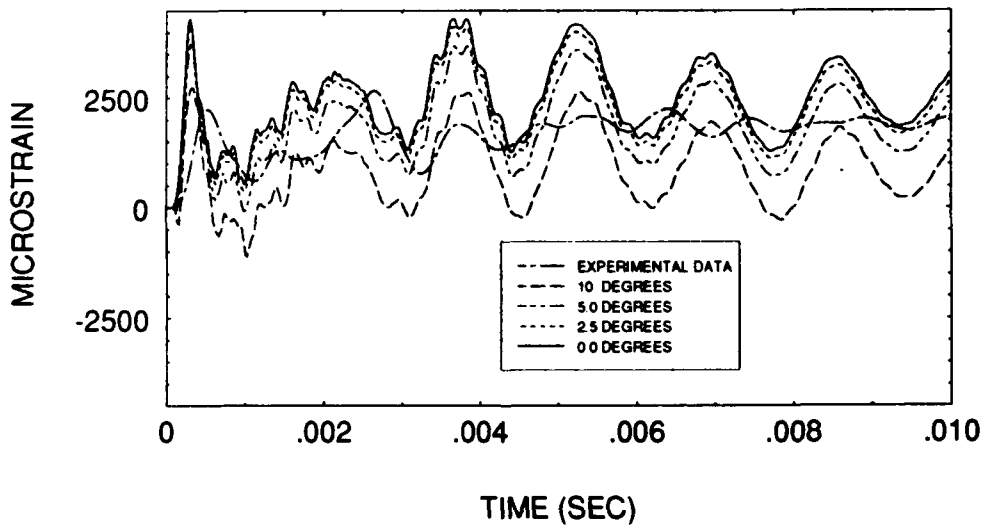


Figure IV.49. Rotation sensitivity results.
(B3 Axial)

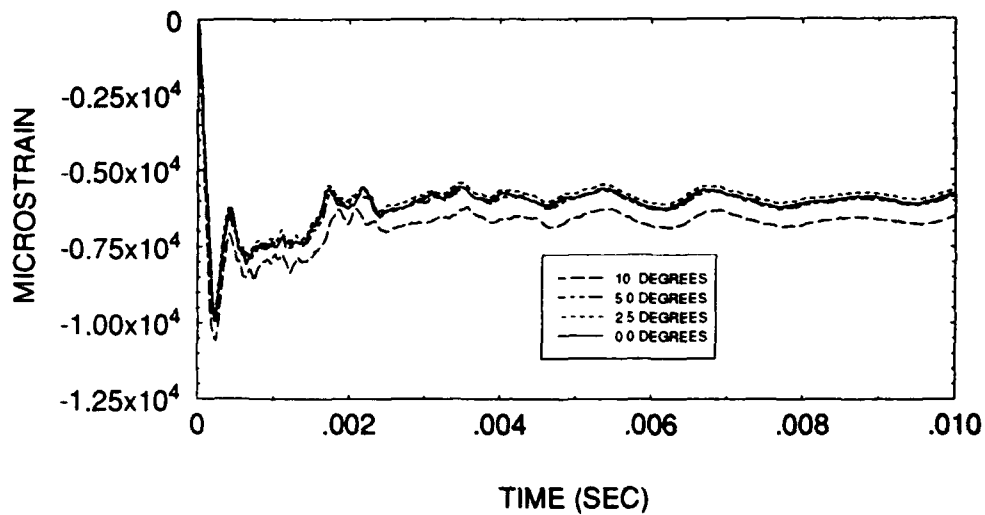


Figure IV.50. Rotation sensitivity results.
(C1 Hoop)

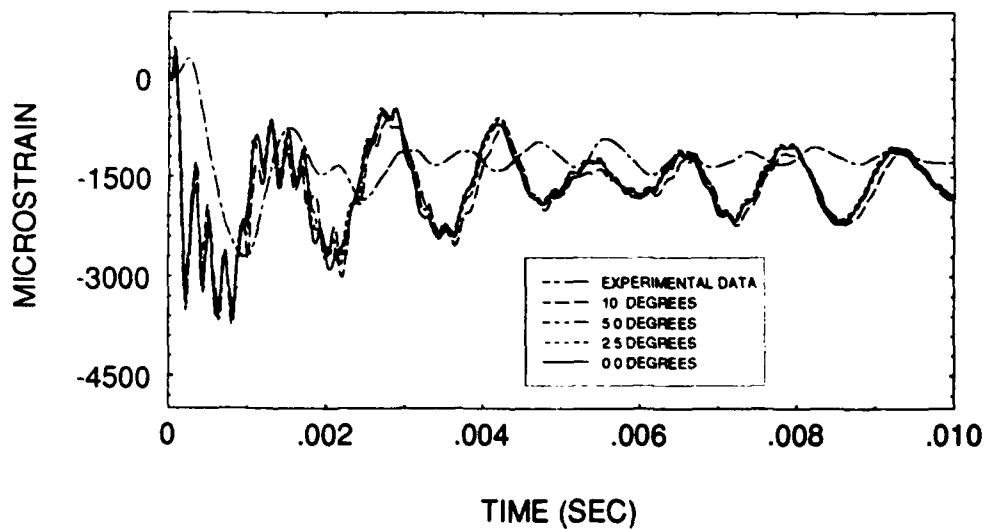


Figure IV.51. Rotation sensitivity results.
(C1 Axial)

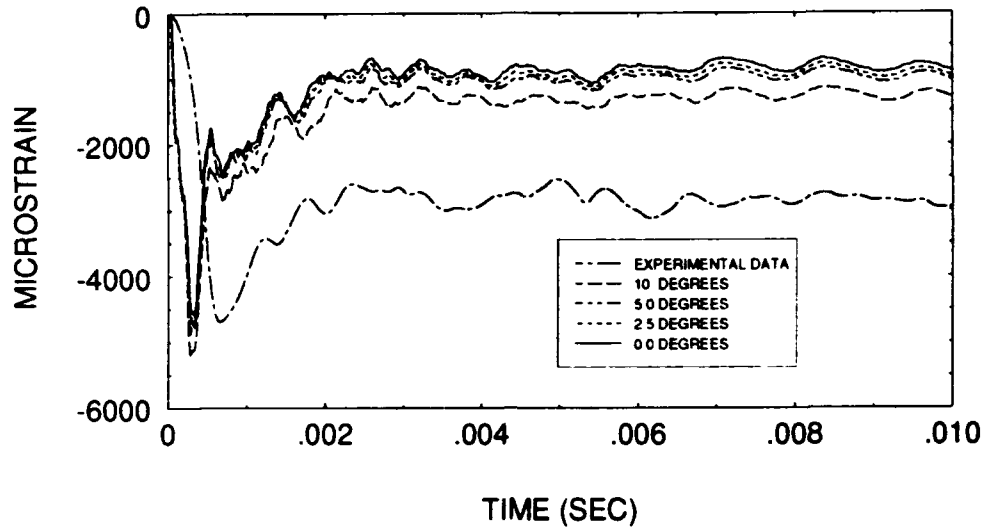


Figure IV.52. Rotation sensitivity results.
(C2 Hoop)

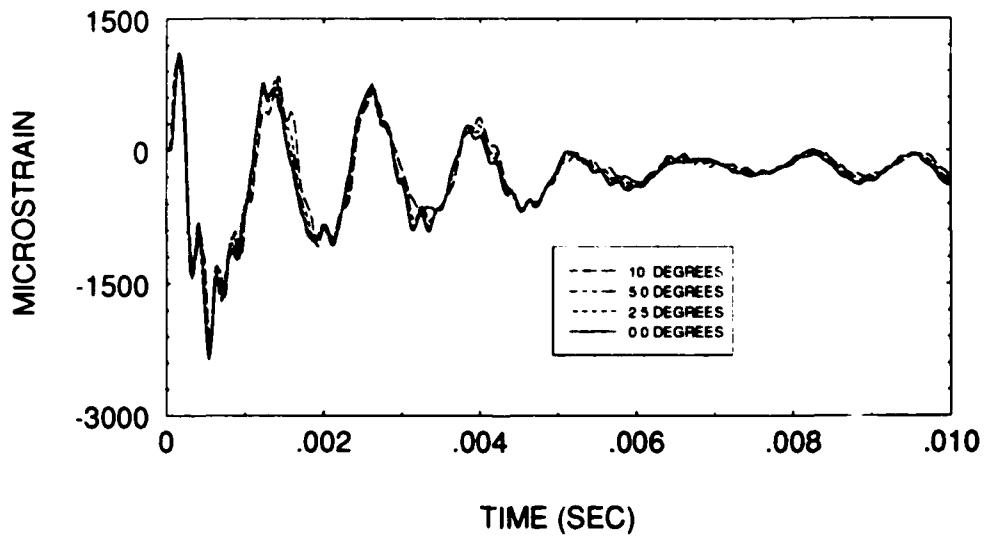


Figure IV.53. Rotation sensitivity results.
(C2 Axial)

higher than the hoop strain at position A2 (Figure IV.43) with a rotation of ten degrees. This is also consistent with the experimental data. Similar positive results were obtained for positions A1 and C1 axial strains. It was further discovered that rotating the cylinder about its axis could further improve the results. However, even though these rotations did improve the results, significant differences still exist between the experimental and numerical strains at the ends of the cylinders. Although it is clear that the model can account for rotational effects, it is also clear that other factors are causing the large differences. Once again, welding affects are suspected to be the probable cause.

The important point to note out of these results is that even small rotations from expected orientation can result in significant errors on in expected results. Therefore extreme care must be taken to ensure that instrumentation cable tension and other unanticipated factors do not cause undetected rotations.

3. PHYSICAL FINDINGS

a. RESPONSE MODES

It was determined that a cylinder subject to a side on explosion will have three primary response modes. The first mode is an accordion motion. The accordion motion

results from the compression and subsequent release of the cylinder in the axial direction. Figure IV.54 shows a plot of points located at the center of each end plate. It is clear

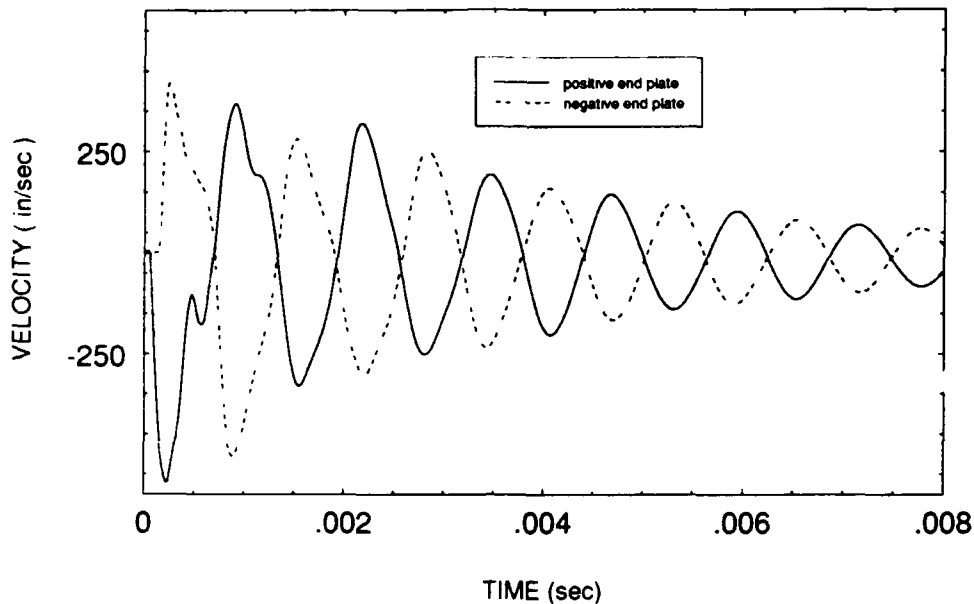


Figure IV.54. Cylinder accordion motion.

that the two end plates are travelling in opposite directions at the same time generating the accordion motion.

The cylinder is also subject to a whipping mode parallel to the direction of shock wave travel. The whipping mode is the most significant motion experienced by the cylinder and is caused as a result of the curvature of the shock wave. In the symmetric situation, the shock wave will come in contact with the center of the cylinder first. This will cause the center to move first, followed by the ends. The cylinder will then move in an oscillatory motion that is

a function of the stiffness and mass distribution of the cylinder and the water surrounding the cylinder. Figure IV.55

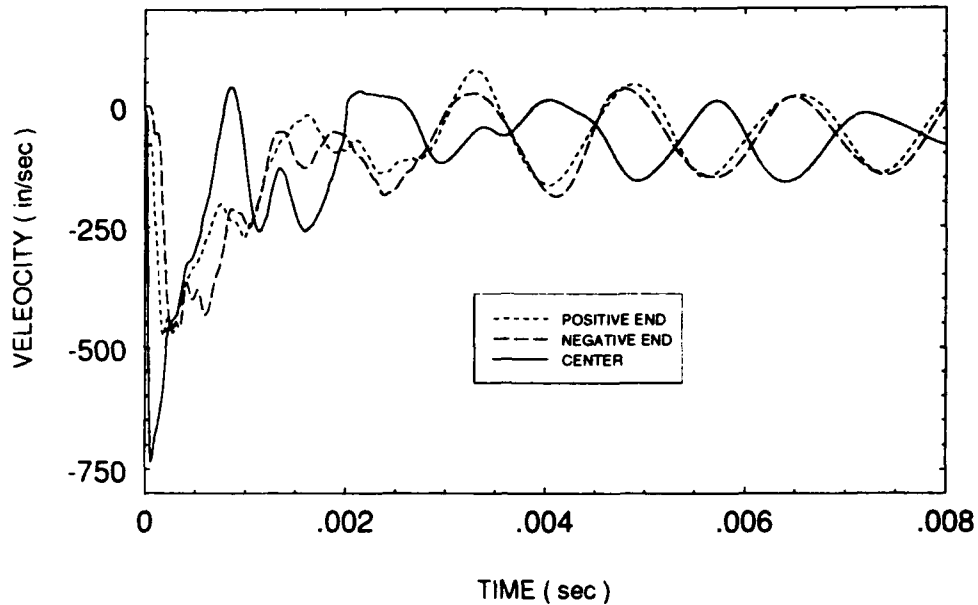


Figure IV.55. Cylinder whipping motion in plane parallel to shock wave direction.

shows a plot of a points located at the center and ends of a line located parallel to the axis on the near side of the cylinder. The plot shows that the end plates are moving in the opposite direction of the cylinder throughout the transient response of the cylinder. Figure IV.56 shows a scale factor 20 drawing of the cylinder at two different times. The cylinder's opposite direction of curvature at the two different times is a result of the whipping motion.

The final response mode noted was a breathing motion in the plane perpendicular to the shock wave direction

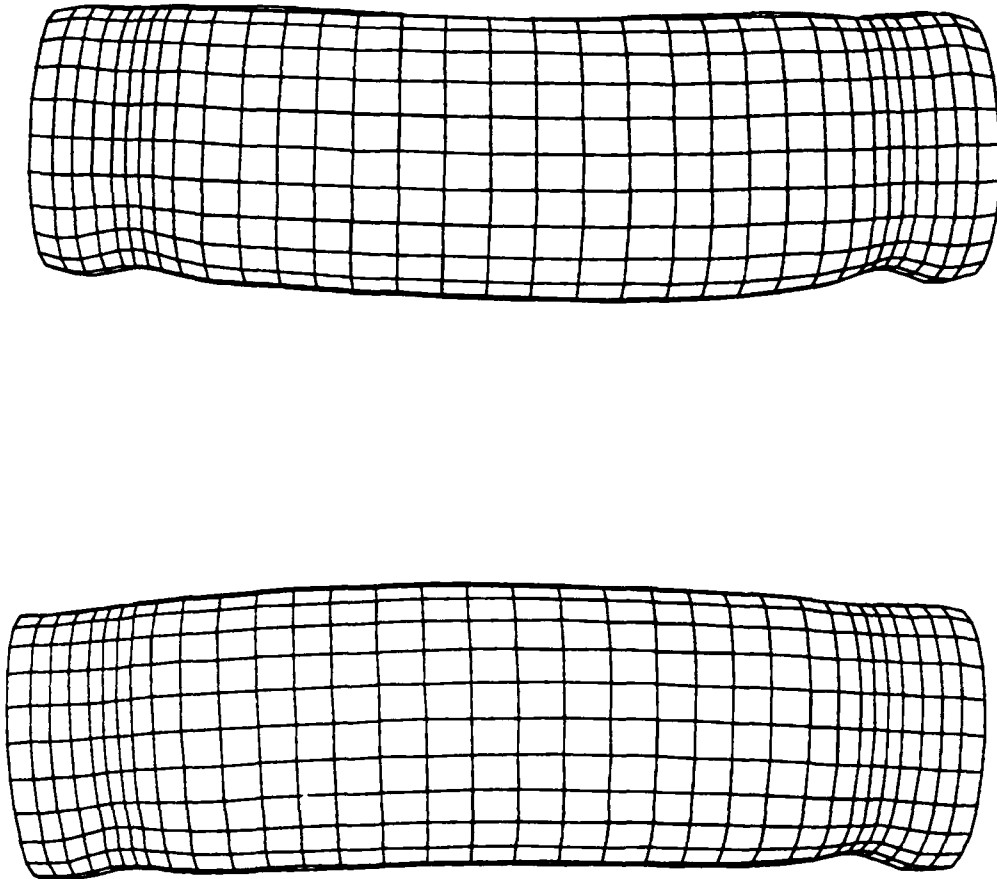


Figure IV.56. Cylinder curvature as a result of whipping motion (scale factor 20).

of travel. Although breathing motion also occurred in the direction parallel to the shock wave travel, it was not as obvious since the much larger whipping motion turned out to be

the predominant mode in that direction. Figure IV.57 shows a plot of two points located at the top and bottom of the

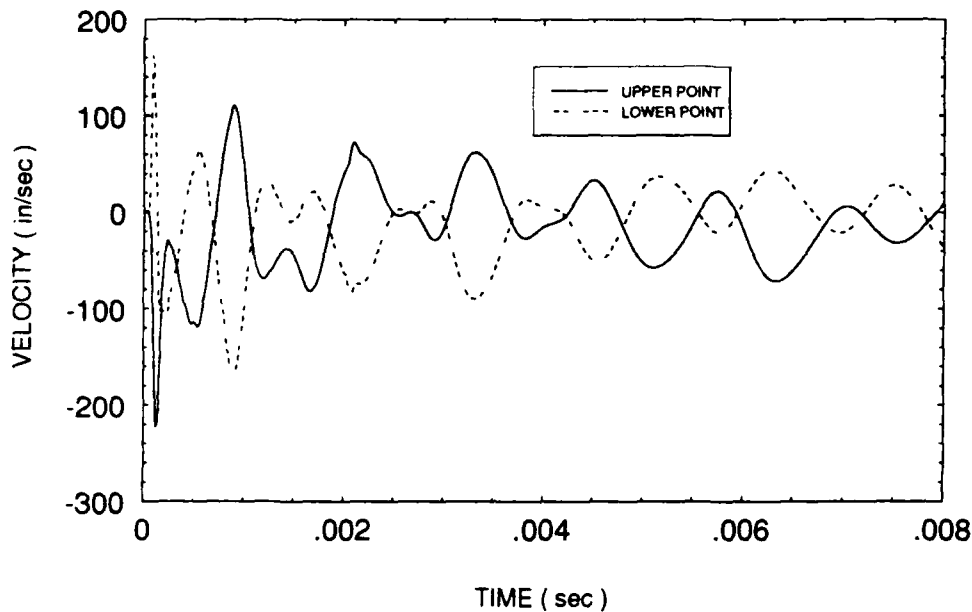


Figure IV.57. Cylinder breathing motion perpendicular to the shock wave direction of travel.

cylinder in a plane perpendicular to the axis at the axial mid point of the cylinder. It can be observed that the upper point is moving in a direction opposite to the lower point throughout the transient response of the cylinder. The breathing motion is also caused by the compression and subsequent release of the cylinder. Figure IV.58 provides an illustration of the breathing motion. The two scale factor 40 drawings are for two separate times and show the shell first bowed inward toward the axis and then outward away from the axis.

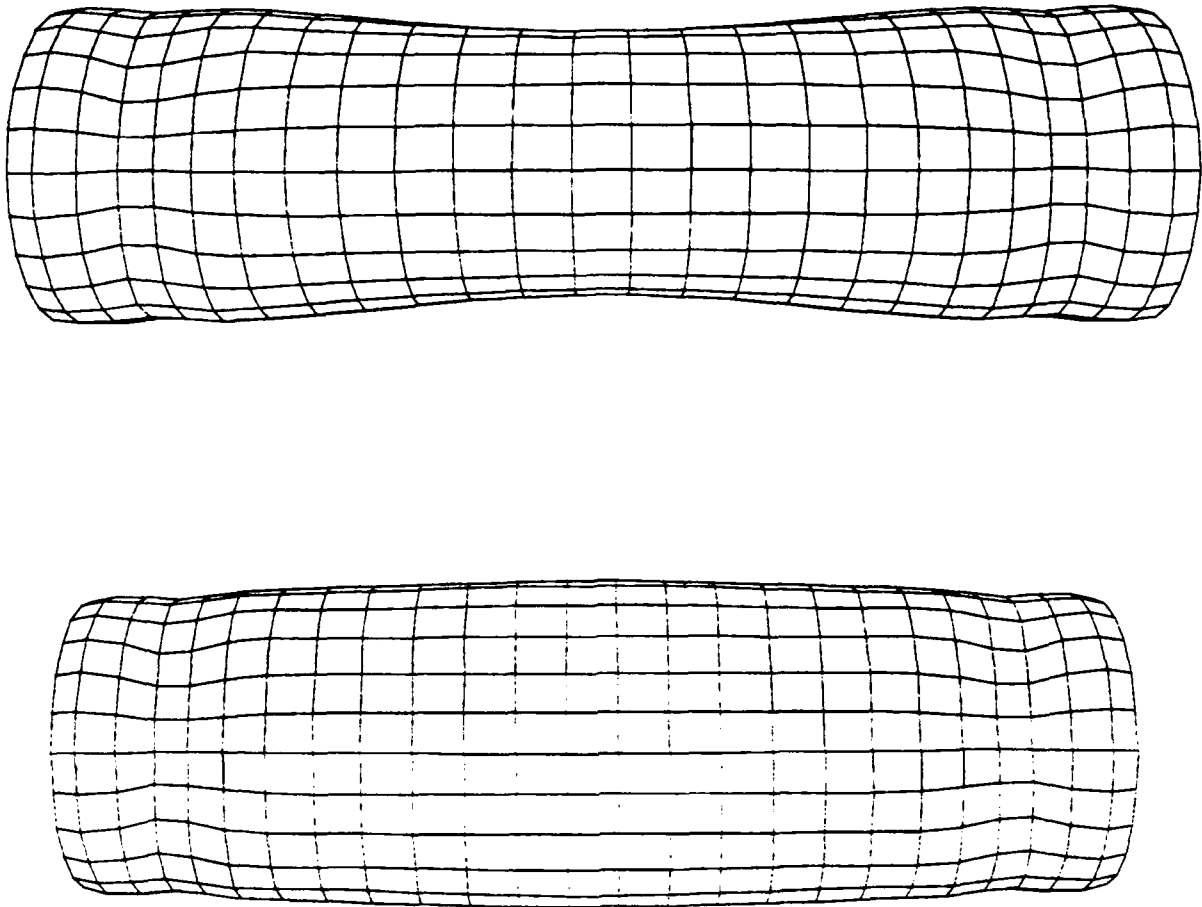


Figure IV.58. Illustration of cylinder breathing mode at two different times (scale factor 40).

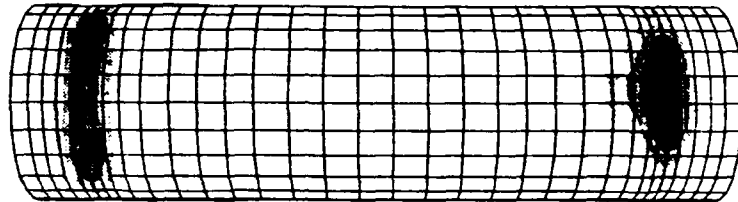
b. ROTATIONAL EFFECTS

Plastic strain fringe plots generated as a result of the rotation sensitivity analysis revealed some interesting information on the causes of the strain distribution

experienced by the cylinder. The experimental results included a reduction in the strain at the rear of the cylinder at position B3, a decrease at A2 relative to C2 and an increase at A1 relative to C1. The fringe plots show why this strain distribution occurs. Figure IV.59 shows the effective plastic strain distribution for a 7.5 degree rotation. The left side of the cylinder is nearest the charge. The results show that the rotation tends to diffuse the strain around the cylinder on the near end while concentrating it at the far end. This causes the distribution noted for positions A1, C1, A2 and C2. At the same time, the high stress region on the reverse side of the cylinder tends to move away from the charge. This placed location B3 in a lower strain region which led to the experimental and numerical results noted at position B3.

THICK SHELL MODEL
time = .59798E-02
fringes of eff. plastic strain
min= 0.000E+00 in element 960
max= 7.104E-03 in element 433

fringe levels
1.089E-03
2.321E-03
3.552E-03
4.783E-03
6.015E-03



THICK SHELL MODEL
time = .59798E-02
fringes of eff. plastic strain
min= 0.000E+00 in element 960
max= 7.104E-03 in element 433

fringe levels
1.089E-03
2.321E-03
3.552E-03
4.783E-03
6.015E-03

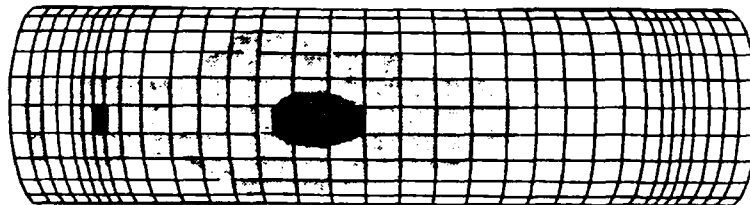


Figure IV.59. Effective plastic strain distribution for near and remote side of cylinder with 7.5 degrees of rotation.

V. CONCLUSIONS AND RECOMMENDATIONS

A. CONCLUSIONS.

1. NUMERICAL MODELLING

Two general conclusions can be reached from the material contained in this report. First, the USA/DYNA3d connection is successful and can replicate the response of simple analytical models.

Second, numerical modeling can predict the response of a simple cylinder to an underwater explosion. Near field numerical predictions matched expected results. However, to fully confirm this, experimental data must be obtained for comparison to the numerical results.

Far field numerical predictions generally match experimental results if rotation and end effects resulting from fabrication caused material property changes are correctly modelled. It was found that results in high strain areas are extremely sensitive to shell formulation, mesh design, quadrature rule and integration time increment. The best results were achieved with brick shell elements. However, the eight node brick shell required substantially longer computation times to achieve the desired results because of the need to reduce the integration time increment. In

addition, it was found that thin shell formulations can also provide correct results. However, results for the Belytschko/Lin/Tsay formulation appear to be very sensitive to the number of quadrature points used for the numerical integration scheme in high strain areas.

2. PHYSICAL ASPECTS

a. NEAR FIELD PHYSICAL RESULTS

The propagation of the pressure wave through the water near the shell was studied. The numerical model correctly predicted pressure response at the shell water interface. In addition, cavitation was predicted next to the shell.

Damage to the shell was primarily local in nature with severe buckling occurring at the point nearest the charge. In addition, stiffeners in stiffened models failed by local buckling (tripping). Further the remote side of the shell experience significant plastic strain as a result of the bending effect caused by the shock wave striking the axial mid plane of the cylinder.

b. FAR FIELD PHYSICAL RESULTS

Primary damage areas are near the ends of the cylinder on the side nearest the charge where the stiff, heavy, flat end plates caused a concentration of the effective plastic strain. Damage also occurred on the reverse side as

a result of a bending effect similar to that described in the near field results. The cylinder experienced breathing, whipping and accordion response modes.

In addition, it was discovered that rotation tends to diffuse strain on the end nearest the charge while concentrating the strain at the far end on the side nearest the charge. The high strain area located at the center of the cylinder on the reverse side tends to migrate toward the end most remote from the charge.

B. RECOMMENDATIONS.

1. TOPICS FOR ADDITIONAL STUDY.

a. WELDING FABRICATION EFFECTS.

An analysis should be performed to quantify the relative effect that the change in material properties generated by the welding fabrication process has on the numerical results. This analysis could include the measurement of material properties near a weldment. These properties could then be added as a separate material in the numerical model.

b. EIGHT NODE BRICK SHELL SENSITIVITY ANALYSES.

Although it was fairly clear that the eight node brick shell formulation comes closest to predicting the overall response of the shell, it was also noted that the formulation is very sensitive to integration time increment in

areas with high strain. Commonly used thumbrules did not appear to be adequate in this case. In addition, additional analyses need to be performed to determine the mesh sensitivity of the eight node brick shell in this model.

c. FAILURE CRITERIA.

This study was performed on a model with relatively low total plastic strain (less than one percent). In order to deal with larger strains, a failure model must be introduced into the material modelling of the cylinder. The model should include structural instability as well as material rupture criteria.

d. NEAR FIELD EXPERIMENTATION

Although the numerical predictions appear to be physically correct, the physical results obtained using them cannot be assumed completely correct until they are confirmed with experimental results. A study should be conducted to compare near field experimental results with numerical predictions.

2. RECOMMENDATIONS TO IMPROVE TEST CONTROL.

Several factors made the comparison of the numerical to experimental results difficult. If properly controlled, the analysis process could be simplified. First, rotation of the cylinder must be carefully controlled. Second, unless specifically required, high strain gradient areas should be

avoided. Placement of the strain gages becomes critical in these locations as does mesh design and integration time increment. If these areas cannot be avoided, additional sensitivity analyses may be required to determine the adequacy of the mesh and integration time increment. Finally, analysis near welded seams should be avoided unless the effects can be quantified. If near weld analysis cannot be avoided, consideration should be given to restoring the heat treatment after the weld process.

LIST OF REFERENCES

1. Boticario, L. A., *Dynamic Response of Cylindrical Shells to Underwater End-On Explosion*, Master's Thesis, Naval Postgraduate School, Monterey, California, 1991.
2. Livermore Software Technology Corporation Report 1018, *VEC/DYNA3D User's Manual (Nonlinear Dynamic Analysis of Structures in Three Dimensions)*, by D. W. Stillman and J. O. Hallquist, June 1990.
3. Livermore Software Technology Corporation Report 1019, *LS-INGRID: A Pre-processor and Three-Dimensional Mesh Generator for the Programs LS-DYNA3D, LS-NIKE3D and TOPAZ-3D, version 3.0*, by D. W. Stillman and J. O. Hallquist, June 1991.
4. Livermore Software Technology Corporation Report 1009, *LS-TAURUS, An Interactive Post-Processor for the Programs LS-DYNA3D, LS-NIKE3D and TOPAZ-3D*, by J. O. Hallquist, April 1990.
5. Deruntz, J. A. Jr. and Rankin, C. C., "Applications of the USA-Stags Codes to Underwater Shock Problems, Palo Alto, California, 1990.
6. Geers, T. L., "Residual Potential and Approximate Methods for Three Dimensional Fluid-Structure Interaction Problem," *Journal of the Acoustic Society of America*, v. 49, pp 1505-1510, 1971.
7. Huang, H., Everstine, C. C. and Wang, Y. F., "Retarded Potential for Analysis of Submerged Structures Impinged by Weak Shock Waves," *Computational Methods for Fluid-Structure Interaction Problems*, AMD-Vol 26, American Society of Mechanical Engineers, December 1977.
8. Geers, T. L., "Computational Methods for Transient Analysis," *Boundary-Element Methods for Transient Response*, Elsevier Science Publishing Co., Inc., New York, New York, p. 231, 1983.
9. Ugural, A. C. and Fenster, S. K., *Advanced Strength and Applied Elasticity, Second S. I. Edition*, Elsevier Science Publishing Co. Inc., New York, New York, p 398, 1987.
10. Huang, H., "Transient Interaction of Plane Waves With a Spherical Elastic Shell," *Journal of the Acoustic Society of America*, v. 45, pp 661-670, 1969.

11. Kwon, Y. W., Fox, P. K. and Shin, Y. S., "Response of a Cylindrical Shell Subject to a Near Field Side-On Explosion," *Proceedings of the 62nd Shock and Vibration Symposium, Volume II*, pp 163 - 178, Pasadena, California, October 1990.
12. Belytschko, T. and Tsay, C. S., "Explicit Algorithms for Non-Linear Dynamics of Shells," AMD-Vol 48, American Society of Mechanical Engineers, pp 209-231, 1981.
13. Dobratz, B. M., *LLNL Explosive Handbook*, Lawrence Livermore Laboratory, University of California, pp 8-21, 1981.
14. Dynamic Testing, Inc. Letter DTI91-183 to United States Naval Postgraduate School, Subj: Cylinder Testing Results; DTI Job No. 131, 4 September 1991.
15. Hughes, T. J. R., *The Finite Element Method. Linear Static and Dynamic Finite Element Analysis*, Prentice Hall, Englewood Cliffs, New Jersey, 1987.
16. Livermore Software Technology Corporation Report 1009, *LS-DYNA3D Course Notes*, by Hallquist, J. O. and Stillman, D. W., October 1990.

INITIAL DISTRIBUTION LIST

	No. of Copies
1. Defense Technical Information Center Cameron Station Alexandria, Virginia 22304-6145	2
2. Library, Code 52 Naval Postgraduate School Monterey, California 93943-5002	2
3. Professor Y. W. Kwon, Code ME/Kw Department of Mechanical Engineering Naval Postgraduate School Monterey, California 93940	1
4. Professor Y. S. Shin, Code ME/Sg Department of Mechanical Engineering Naval Postgraduate School Monterey, California 93940	1
5. Department Chairman, Code ME Department of Mechanical Engineering Naval Postgraduate School Monterey, California 93940	1
6. Dr. Thomas T. Tsai Defense Nuclear Agency 6801 Telegraph Road Alexandria, Virginia 22310	1
7. Dr. Kent Goering Defense Nuclear Agency 6801 Telegraph Road Alexandria, Virginia 22310	1
8. Mr. Douglas Bruder Defense Nuclear Agency 6801 Telegraph Road Alexandria, Virginia 22310	1
9. Dr. Phillip B. Abraham Office of Naval Research Mechanics Division, Code 1132 800 North Quincy Street Arlington, Virginia 22217-5000	1

- | | | |
|-----|--|---|
| 10. | Mr. Gene Remmers, ONT-23
Director, Office of Naval Technology
800 N. Quincy Street
Arlington, Virginia 22217-5000 | 1 |
| 11. | Professor Thomas L. Geers
Department of Mechanical Engineering
Campus Box 427
University of Colorado
Boulder, Colorado 80309 | 1 |
| 12. | Dr. John A. Deruntz Jr.
Computational Mechanics Section
Lockheed Palo Alto Research Laboratories
3251 Hanover Street
Organization 93-30
Palo Alto, California 94304 | 1 |
| 13. | LCDR Padraic K. Fox
RR 3, Box 181
Watertown, South Dakota 57201 | 1 |